JOURNAL OF

Journal of Petrology, 2016, Vol. 0, No. 0, 1–44 doi: 10.1093/petrology/egw050 Original Article



# Petrochronological Constraints on the Origin of the Mountain Pass Ultrapotassic and Carbonatite Intrusive Suite, California

Jacob E. Poletti<sup>1</sup>\*, John M. Cottle<sup>1</sup>, Graham A. Hagen-Peter<sup>1</sup> and Jade Star Lackey<sup>2</sup>

<sup>1</sup>Department of Earth Science, University of California, Santa Barbara, CA 93106-9630, USA and <sup>2</sup>Geology Department, Pomona College, Claremont, CA 91711, USA

\*Corresponding author. Telephone: 805-748-2549. Department telephone: 805-893-4688. Department fax: 805-893-2314. E-mail: jakepoletti@gmail.com

Received October 21, 2015; Accepted August 3, 2016

### **ABSTRACT**

Rare earth element (REE) ore-bearing carbonatite dikes and a stock at Mountain Pass, California, are spatially associated with a suite of ultrapotassic plutonic rocks, and it has been proposed that the two are genetically related. This hypothesis is problematic, given that existing geochronological constraints indicate that the carbonatite is  $\sim$ 15–25 Myr younger than the ultrapotassic rocks, requiring alternative models for the formation of the REE ore-bearing carbonatite during a separate event and/or via a different mechanism. New laser ablation split-stream inductively coupled plasma mass spectrometry (LASS-ICP-MS) petrochronological data from ultrapotassic intrusive rocks from Mountain Pass yield titanite and zircon U-Pb dates from 1429 ± 10 to 1385 ± 18 Ma, expanding the age range of the ultrapotassic rocks in the complex by  $\sim\!\!20$  Myr. The ages of the youngest ultrapotassic rocks overlap monazite Th-Pb ages from a carbonatite dike and the main carbonatite ore body (1396  $\pm$  16 and 1371  $\pm$  10 Ma, respectively). The Hf isotope compositions of zircon in the ultrapotassic rocks are uniform, both within and between samples, with a weighted mean  $\varepsilon Hf_i$  of  $1.9 \pm 0.2$  (MSWD = 0.9), indicating derivation from a common, isotopically homogeneous source. In contrast, in situ Nd isotopic data for titanite in the ultrapotassic rocks are variable  $(\varepsilon Nd_i = -3.5 \text{ to } -12)$ , suggesting variable contamination by an isotopically enriched source. The most primitive  $\varepsilon Nd_i$  isotopic signatures, however, do overlap  $\varepsilon Nd_i$  from monazite ( $\varepsilon Nd_i = -2.8 \pm 0.2$ ) and bastnäsite ( $\epsilon Nd_i = -3.2 \pm 0.3$ ) in the ore-bearing carbonatite, suggesting derivation from a common source. The data presented here indicate that ultrapotassic magmatism occurred in up to three phases at Mountain Pass (~1425, ~1405, and ~1380 Ma). The latter two stages were coeval with carbonatite magmatism, revealing previously unrecognized synchronicity in ultrapotassic and carbonatite magmatism at Mountain Pass. Despite this temporal overlap, major and trace element geochemical data are inconsistent with derivation of the carbonatite and ultrapotassic rocks by liquid immiscibility or fractional crystallization from common parental magma. Instead, we propose that the carbonatite was generated as a primary melt from the same source as the ultrapotassic rocks, and that although it is unique, the Mountain Pass ultrapotassic and carbonatite suite is broadly similar to other alkaline silicate-carbonatite occurrences in which the two rock types were generated as separate mantle melts.

Key words: carbonatite; geochronology; mineralization; rare earth elements; titanite

### INTRODUCTION

The Sulphide Queen rare earth element (REE) mine at Mountain Pass, California is the richest known source of REE ore in the USA (Long *et al.*, 2010). Since its discovery in 1949 until the late 1980s Mountain Pass was the world's foremost producer of REE commodities (Verplanck & Van Gosen, 2011). However, despite its status as an archetype for carbonatite-hosted REE deposits, the petrogenesis of the REE-bearing Mountain Pass carbonatite remains debated.

Carbonatite bodies at Mountain Pass, along with ultrapotassic, mafic to felsic, plutonic silicate rocks (shonkinite, syenite, and granite), make up the Mesoproterozoic Mountain Pass Intrusive Suite (MPIS, Fig. 1). Based on field relationships and the similar enrichment of these rocks in incompatible elements such as Sr, Ba, and light REE (LREE), previous workers have inferred that the Sulphide Queen carbonatite magma was derived from the same source as the ultrapotassic rocks and that the intrusive assemblage may represent a single suite of variably evolved alkaline igneous rocks (Woyski, 1980; Castor, 2008). This is broadly compatible with studies from a variety of locations worldwide suggesting that carbonatite and alkali-rich silicate melts can differentiate from the same parental magma, potentially by liquid immiscibility (e.g. Lee & Wyllie, 1998; Woolley, 2003; Panina & Motorina, 2008), extreme fractional crystallization of a CO<sub>2</sub>-rich silicate melt (e.g. Bell et al., 1999), or a combination of these processes (e.g. Beccaluva et al., 1992).

In contrast, existing geochronological data from the MPIS suggest that the carbonatite is  $\sim$ 15–25 Myr younger than the ultrapotassic rocks at Mountain Pass, which yielded ages of ~1375 Ma and ~1400 Ma, respectively (DeWitt et al., 1987, 2000; Premo et al., 2013). Interpretation of existing data is complicated by the fact that the ages are derived from different minerals and isotopic systems in each rock type (i.e. zircon and apatite U-Pb, monazite U-Th/ Pb, amphibole and biotite Ar-Ar) and are exclusively reported in conference abstracts (DeWitt et al., 1987, 2000; Premo et al., 2013). Thus, these ages lack the information necessary to directly compare the dates, such as which decay constants and monitor standards were used, and what sources of uncertainty are included in the quoted data. Furthermore, DeWitt et al. (1987) noted U-Pb discordance and 'anomalously young' dates in some samples, suggesting that age interpretation may be complicated for some rock types at Mountain Pass.

Field relationships generally indicate that carbonatite is the youngest rock type in the MPIS in terms of crosscutting relationships, but at least one study noted that a centimeter-scale vein of shonkinite appears to cut carbonatite in at least one location (Olson & Pray, 1954), inconsistent with the geochronological data. Given that fractional crystallization and liquid immiscibility processes are commonly thought to operate over timescales  $\ll 10$  Myr (e.g. Williams  $et\ al.$ , 1986; Schmitt  $et\ al.$ , 2010), the proposed 15–25 Myr age gap is irreconcilable with the hypothesis that the carbonatite and the

ultrapotassic rocks are derived from the same parental magma or were generated during the same melting event. Thus, it has been asserted that, although these rocks are geochemically similar, the MPIS is not a simple cogenetic magma series (e.g. Haxel, 2005), and models testing the common parental magma hypothesis have not been presented.

This study utilizes titanite, zircon, and monazite U-Th/Pb geochronology, accessory-phase and whole-rock geochemistry, Nd and Hf isotope geochemistry and petrography within the context of field data to decisively resolve the temporal and petrogenetic relationships between carbonatite and ultrapotassic igneous rocks in the MPIS. A quantitative model is developed to test whether the ultrapotassic rocks and carbonatites at Mountain Pass are related by fractional crystallization or liquid immiscibility. In aggregate, these data place new constraints on existing ore genesis models for the Sulphide Queen carbonatite REE deposit, and indicate that the MPIS is the result of long-lived carbonatitealkaline silicate magmatism in which multiple melting events of the same source produced separate carbonatite and ultrapotassic melts.

#### **GEOLOGICAL CONTEXT**

The Mountain Pass district is located in the central Mojave Desert of California, about 75 km SSW of Las Vegas, Nevada (Fig. 1). The district encompasses a topographic low between the Clark Mountain Range to the north and the Mescal Range to the south, and is primarily underlain by autochthonous, Proterozoic crystalline basement rocks that lie in the footwall of the westdipping Keystone Thrust of the Sevier Orogen (Burchfiel & Davis, 1971; Fig. 1b). Neoproterozoic to lower Paleozoic limestone, quartzite, and shale, and Mesozoic siliciclastic and felsic volcanic rocks lie above the thrust in the Mountain Pass area (Evans, 1974). In the east, the  $\sim$ 7 km wide structural block of Proterozoic crystalline rocks is bound by the inferred normal-sense Ivanpah fault (Olson et al., 1954). The structural block that exposes MPIS rocks is also cut by several transverse faults, none of which place the Proterozoic rocks against units of significantly different age or lithology (Olson et al., 1954; Fig. 1b). Despite local faulting, decimeter- to meter-scale dike emplacement in the Cenozoic, and minor, localized hydrothermal alteration and localized deposition of Th along faults (Shawe, 1952), the Proterozoic rocks in the district are relatively well preserved and were less affected by Cenozoic extension and deformation compared with neighboring areas in the Mojave Desert (Haxel, 2005).

#### **GEOLOGICAL UNITS AT MOUNTAIN PASS**

#### Paleoproterozoic host rocks

The Proterozoic crystalline basement rocks that underlie most of the Mountain Pass area are part of the Mojave

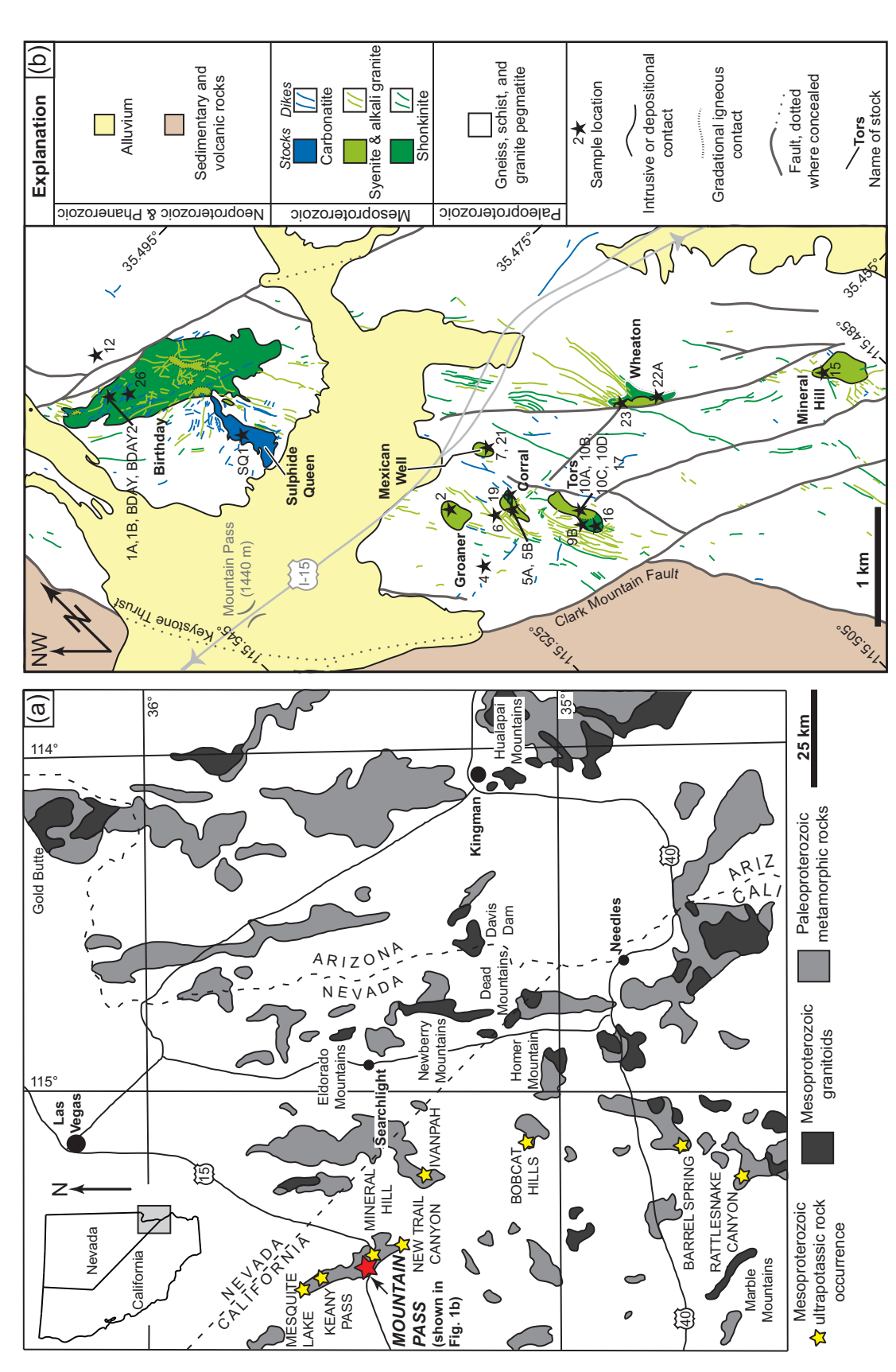


Fig. 1. (a) Map showing locations of Paleoproterozoic metamorphic rocks and Mesoproterozoic intrusive rocks in the southwestern USA. Modified from Castor (2008). (b) Generalized geological map of the Mountain Pass area. Alluvium contacts/exposures have been simplified for clarity. It should be noted that dike thickness is not to scale, and that north is not up. Modified from Haxel (2005), after Olson & Pray (1954), Olson et al. (1954), Burchfiel & Davis (1971) and Evans (1971).

Crustal Province (Wooden & Miller, 1990) and are primarily Paleoproterozoic gneiss and schist. The Paleoproterozoic rocks of the Mojave Crustal Province record a complex history of plutonism, metamorphism, and sedimentation associated with multiple orogenic events. U-Pb zircon ages from the province reported in several studies have been interpreted to indicate several discrete episodes of widespread pluton emplacement between ~1.79 and 1.64 Ga (Wooden & Miller, 1990; Barth et al., 2000, 2009; Strickland et al., 2013; McKinney et al., 2015). Zircon and monazite U-Pb ages indicate that metamorphism also took place in several discrete episodes, occurring locally between ~1.79 and 1-65 Ga (Wooden & Miller, 1990; Barth et al., 2000, 2009; Strickland et al., 2013; McKinney et al., 2015). The Paleoproterozoic rocks of the Mojave Crustal Province were widely intruded by 1.45-1.40 Ga granitoids throughout the southwestern USA (e.g. Anderson & Bender, 1989; McKinney et al., 2015), including the Mountain Pass Intrusive Suite. The origin of the 1.45-1.4 Ga granitoids and the tectonic environment in which they were emplaced remains debated, with some workers inferring an anorogenic setting (e.g. Anderson & Bender, 1989; Hoffman, 1989), whereas others have concluded that they were emplaced during an orogenic event at  $\sim 1.49-1.35$  Ga (Picuris orogeny of Daniel et al., 2013; and see also Nyman et al., 1994; Daniel & Pyle, 2006; Whitmeyer & Karlstrom, 2007).

In the Mountain Pass area, the Paleoproterozoic rocks are quartzofeldspathic gneiss and schist, coarsegrained to pegmatitic alkali granite dikes, and minor mafic to ultramafic rocks (this work; Olson et al., 1954; Haxel, 2005; Castor, 2008; Fig. 1). K-feldspar augen gneiss and migmatitic K-feldspar + plagioclase + quartz + biotite ± garnet ± sillimanite gneiss are most common. Foliation in the gneiss and schist generally strikes north to NW and dips 45-85° to the west (this work; Olson & Pray, 1954; Olson et al., 1954). Mineral ages from Paleoproterozoic rocks in the Mountain Pass area have not been reported, but are generally assumed to be similar to the rest of the Mojave Crustal Province based on their similar field relationships, lithology and close proximity to well-studied occurrences (e.g. Ivanpah Mountains, Strickland et al., 2013; Fig. 1a).

#### **Mountain Pass Intrusive Suite**

Paleoproterozoic rocks in the Mountain Pass area are intruded by hundreds of sub-meter- to meter-scale dikes and eight map-scale stocks that compose the Mountain Pass Intrusive Suite (Fig. 1b). Six of the stocks consist of shonkinite and/or syenite, one contains significant granite in addition to syenite (Mineral Hill), and the Sulphide Queen stock is carbonatite (Fig. 1b). Geochemical, mineralogical, and textural gradations between shonkinite-syenite and syenite-granite are common in single bodies. The stocks form ovoid to roughly tabular, sill-like bodies tens to hundreds of meters wide and hundreds of meters long, and occur

within a  $\sim$ 7 km  $\times$  2 km zone in the host gneiss. Most dikes and stocks in the MPIS are oriented roughly parallel to the regional foliation of the basement rocks (roughly north to NW), but some dikes also strike roughly NE. Dikes and stocks of both orientations crosscut foliation on an outcrop scale and are undeformed; there does not appear to be an obvious structural reason for the two different trends. In general, crosscutting relationships indicate that the sequence of intrusion in the MPIS was (1) shonkinite and melanosyenite, (2) syenite, (3) quartz syenite, (4) granite, (5) shonkinite dikes, and (6) carbonatite (e.g. this work, Fig. 2a-d; Olson et al., 1954; Haxel, 2005; Castor, 2008). However, as stated above, a centimeter-scale shonkinite vein appears to cut carbonatite in at least one location (Olson & Pray, 1954; Haxel, 2007). Magma mingling and mixing textures are common in some areas (e.g. Tors stock, Figs 1b and 2e; Haxel, 2005), and some shonkinite dikes within syenite are discontinuous, deformed, and backintruded by fine-grained syenite (Fig. 2f), indicating that emplacement of some of the shonkinite and syenite was synchronous (this work; Haxel, 2005). The Sulphide Queen carbonatite stock, which is the principal ore body at Mountain Pass (Fig. 1b), contains blocks of gneiss, shonkinite, syenite, and older carbonatite, the last indicating that carbonatite was not emplaced during a single event (Olson et al., 1954).

The MPIS lies roughly at the northwesternmost end of a zone containing Mesoproterozoic alkaline granitoid plutons that vary in areal exposure from  $\sim$ 4 to 150 km<sup>2</sup>, extending from southeastern California into southern Nevada and western Arizona (Haxel, 2007; Castor, 2008; Fig. 1a; also see above). Ultrapotassic rocks are known only from the western edge of this zone and form an ~130 km belt from Rattlesnake Canyon in the south to Mesquite Lake in the north (Castor, 2008; Fig. 1a), indicating that their occurrence at Mountain Pass is potentially not unique (e.g. Gleason et al., 1994). However, the ultrapotassic rocks that compose the belt are not well studied outside the Mountain Pass area, with the exception of the Barrel Spring Pluton in the Piute Mountains (Gleason et al., 1994; Fig. 1a). Generally, neither the relationships among ultrapotassic rock occurrences in the region nor the broader connections to Mesoproterozoic alkaline magmatism in the southwestern USA are well studied (Haxel, 2007; Castor, 2008).

### Shonkinite

The most abundant intrusive rock in the study area is coarse-grained shonkinite—a distinctive, dark gray to greenish rock composed of microcline, clinopyroxene (diopside, augite, and/or aegirine–augite), and euhedral, Mg-rich biotite, with or without amphibole (riebeckite, arfvedsonite, and/or hornblende) and minor sodic plagioclase, perthite, and apatite (up to  $\sim$ 3%). Accessory phases include quartz, zircon, titanite, magnetite, pyrite, Fe-oxides, calcite, and fluorite. Some samples contain

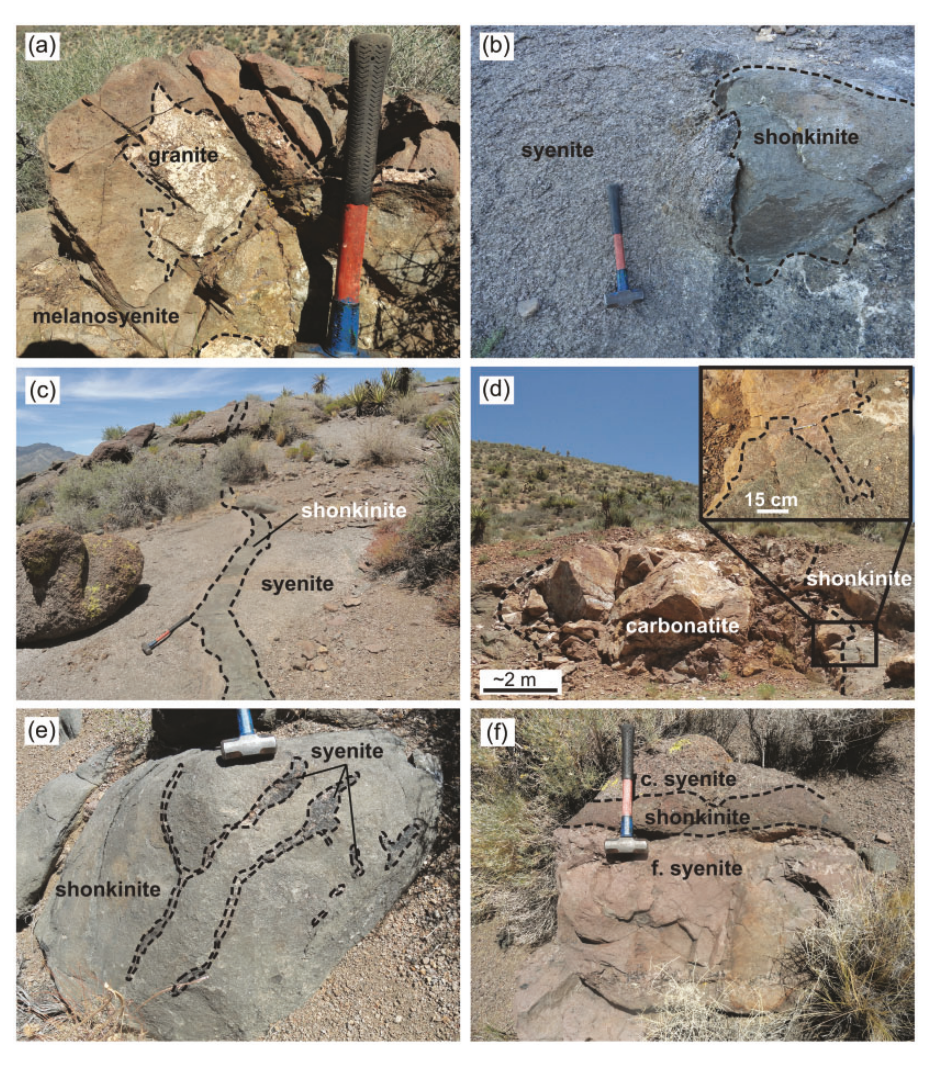


Fig. 2. Examples of cross-cutting relationships within the MPIS. Contacts are indicated by dashed lines for clarity. (a) Granite xeno-liths in melanosyenite dike (MP-P0913-6) just west of Corral stock. (b) Porphyritic shonkinite enclave (MP-P0914-10A) in coarse syenite (MP-P0913-10B) in Tors stock. (c) Porphyritic shonkinite dike (e.g. MP-P0913-10C) in coarse syenite (MP-P0913-10B) in Tors stock. (d) Bastnäsite-barite carbonatite dike (MP-L0613-BDAY2; Birthday Vein) that cuts coarse shonkinite (MP-L0613-BDAY, MP-P0913-1A) in Birthday stock. (e) Diffuse syenite inclusions in shonkinite at Tors stock. (f) Shonkinite dike that cuts coarse syenite and is back-intruded by fine-grained syenite (MP-P0714-17) in Tors stock (ex situ). c, coarse; f, fine.

micrometer-scale veins composed primarily of barite, quartz, and Fe-oxide with minor monazite. Based on mineralogy, the rock is a melanosyenite; however, the name shonkinite is used here to maintain continuity with previous work and to describe the most mafic rocks consisting of K-feldspar + biotite + clinopyroxene ± amphibole. Melanosyenite is used for rocks that are transitional from shonkinite-syenite and contain  $\sim$ 40–55% mafic minerals. The shonkinite has MgO > 3 wt %, K<sub>2</sub>O > 3 wt %, and  $K_2O/Na_2O > 2$ , and is therefore considered ultrapotassic based on the criteria of Foley et al. (1987). Some shonkinite is peralkaline [highest ( $K_2O + Na_2O$ )/ $Al_2O_3 \sim 1.1$ ], but most samples are metaluminous. Sample petrographic descriptions and photographs of representative hand samples are provided in Supplementary Data Electronic Appendices 1 and 2, respectively (supplementary data are available for downloading at http://www.petrology. oxfordjournals.org).

## Syenite, quartz syenite, and granite

Syenite is the second most common intrusive rock type at Mountain Pass, occurring as a pinkish to purple to brick-red rock that consists mostly of K-feldspar with variable amounts of biotite, sodic amphibole (riebeckite and/or arfvedsonite) and quartz, with minor sodic plagioclase, clinopyroxene, and Fe-oxides. Accessory minerals include apatite, zircon, titanite, pyrite, fluorite, calcite, thorite, and galena. Rutile, epidote, monazite, and trace barite are present in some samples, but textural relationships suggest that these phases are secondary. Monazite and barite primarily occur in veins, as fine, disseminated grains (this work; Stoeser, 2013), or as fine aggregates, and are most abundant in samples with pervasive rustcolored stains along grain boundaries and fractures (see Supplementary Data Electronic Appendix 1). Based on these textures, we consider samples with abundant veins and/or fine, disseminated monazite and barite

grains to be altered (see also Stoeser, 2013). Leucosyenite, quartz syenite, and granite occur as dikes and pods in shonkinite or syenite, although the Mineral Hill stock (Fig. 1b) contains significant granite. The mineralogy of these rock types differs from that of syenite only in the relative proportions of K-feldspar and quartz. Some syenite and all leucosyenite at Mountain Pass is potassic rather than ultrapotassic (see criteria above); however, we use the term ultrapotassic here to refer to all K-rich igneous rocks for brevity.

#### Carbonatite

Carbonatite at Mountain Pass varies in appearance, but is generally porphyritic with centimeter-size barite phenocrysts in a matrix of calcite, dolomite, quartz, Feoxide, and bastnäsite ([LREE]CO<sub>3</sub>F). Synchysite (Ca[LREE](CO<sub>3</sub>)<sub>2</sub>F), parisite (Ca[LREE]<sub>2</sub>(CO<sub>3</sub>)<sub>3</sub>F<sub>2</sub>), ankerite, siderite, monazite, thorite, zircon, strontianite, celestite, apatite, an unidentified Th-carbonate, and at least two unidentified REE-bearing phases are common as minor, accessory, or trace phases. The most abundant types of carbonatite are bastnäsite–barite beforsite (dolomite-dominated) and bastnäsite–barite dolomitic sövite (calcite-dominated with significant dolomite), but sövite (calcite-dominant) and silicio-carbonatite are also common (Castor, 2008).

# SUMMARY OF PREVIOUS GEOCHEMICAL, GEOCHRONOLOGICAL, AND ISOTOPIC WORK AT MOUNTAIN PASS

Previous workers generally agreed that the MPIS carbonatite and ultrapotassic rocks are genetically related based on field relationships and similar geochemical characteristics (e.g. Olson et al., 1954; Woyski, 1980; Haxel, 2005, 2007; Castor, 2008). Haxel (2005, 2007) proposed that a small degree ( $\sim 0.01-0.1\%$ ) of partial melting of highly enriched lithospheric mantle source produced the shonkinite magma. In this model, shonkinite is the parental magma that evolved to the more silicic rock types in the complex (syenite, quartz syenite, granite). Crow (1984) showed that the syenite could be produced by ~20% crystal fractionation of the shonkinite. The relatively high abundance of compatible elements (e.g. Cr, Ni) but distinctively lower contents of Al, Ca, and Na in the shonkinite in comparison with other primitive mafic rocks was interpreted to indicate derivation from harzburgitic peridotite that had previously been depleted in Al, Ca, and Na through extraction of basaltic magma (Haxel, 2007). These geochemical characteristics coupled with extreme enrichment in incompatible elements (i.e. K, Ba, LREE) in the MPIS rocks require that the depleted source was metasomatically re-enriched (Haxel, 2007). The model of Haxel (2005) did not consider derivation of the carbonatite from a shonkinite parental magma, partially owing to the implications of the geochronological data reported by DeWitt et al. (1987, 2000). Conversely, Castor (2008) viewed the

spatial association and similar geochemistry of the ultrapotassic rocks and carbonatites as evidence for a common parental magma.

Available geochronological data do not support the notion that the ultrapotassic rocks and carbonatites may have differentiated from a common parental magma. Early attempts to determine ages of the MPIS yielded data that were too imprecise to critically evaluate the absolute timing of the various intrusive phases (i.e. Jaffe, 1955; Lanphere, 1964). More recent studies by DeWitt et al. (1987, 2000) reported  $^{40}$ Ar/ $^{39}$ Ar dates of 1400  $\pm$  8 Ma and 1403 ± 7 Ma from phlogopite in shonkinite and arfvedsonite in syenite, respectively; apatite from shonkinite yielded a U-Pb date of 1410 ± 2 Ma; monazite from carbonatite yielded a Th-Pb date of 1375 ± 7 Ma. Zircons from the syenite were reportedly highly discordant with respect to U-Pb. Bastnäsite and parisite from carbonatite contained abundant common Pb-both vielding dates of ~1330 Ma and younger, which DeWitt et al. considered 'anomalously young' based on the monazite Th-Pb date of  $1375 \pm 7$  Ma for the same rock type. DeWitt et al. (1987, 2000) interpreted these dates as indicating emplacement of carbonatite ~25 Myr after crystallization of the ultrapotassic intrusive rocks.

Premo *et al.* (2013) reported zircon U–Pb secondary ionization mass spectrometry dates from shonkinite, syenite, and granite that overlap within uncertainty between 1410 and 1422 Ma, supporting the interpretations of DeWitt *et al.* (1987, 2000), but did not specify whether there was a statistically distinguishable age difference between rock types.

DeWitt et al. (1987, 2000) and Premo et al. (2013) also reported Pb, Sr, and Nd isotopic data for the MPIS. Common Pb isotopic ratios from galena in carbonatite and K-feldspar in the ultrapotassic rocks are as follows:  $^{204}$ Pb: $^{206}$ Pb = 1:16·08,  $^{204}$ Pb: $^{207}$ Pb = 1:15·32,  $^{204}$ Pb: $^{208}$ Pb = 1:35-61 (DeWitt et al., 1987). 87Sr/86Sr ratios vary from 0.7046 to 0.7072 (DeWitt et al., 2000). Premo et al. (2013) reported a slightly smaller range of whole-rock 87Sr/86Sr (0.7045-0.7068) and whole-rock εNd; values ranging from -1.5 to -6 for the ultrapotassic rocks and carbonatite. DeWitt et al. (2000) interpreted their Pb, Sr, and Nd isotope data to indicate derivation of the carbonatite magma from a hybrid source, produced by mixing of 1.4 Ga mantle and 1.75 Ga mantle or enriched lower crust. DeWitt et al. (2000) also noted that only the youngest shonkinite dikes at Mountain Pass have the same Nd isotopic signature as the carbonatite.

Based on their U–Th/Pb data, DeWitt *et al.* (1987, 2000) and Premo *et al.* (2013) concluded that, although the various intrusive phases in the MPIS appear to be closely related based on petrological and geochemical evidence, the different rock types of the MPIS were not contemporaneous.

#### **ANALYTICAL METHODS**

Here, we report new U-Th/Pb, trace element, isotopic, and/or textural data for a suite of U- and/or Th-bearing

accessory minerals from 22 Mountain Pass shonkinite, syenite, and carbonatite samples and three host-rock samples. Additionally, whole-rock geochemical data are reported for 14 ultrapotassic rock samples and one carbonatite sample. Three to four kilograms of each sample was collected from suitable outcrops (e.g. Fig. 2), and representative samples were selected for mineral analysis based on cross-cutting relationships, lithology, and spatial context (see Table 1 for summary of samples and sample locations). Zircon, titanite, monazite, apatite, bastnäsite and rutile were analyzed, but the measured concentrations of U in the last three minerals were too low to provide reliable U-Pb dates; therefore only zircon, titanite, and monazite data are utilized for geochronology in this study. Bastnäsite and apatite are employed only for Nd isotopic data and trace element data, respectively. Accessory mineral U-Th/Pb isotopes and trace elements were measured by laser ablation split-stream inductively coupled plasma mass spectrometry (LASS-ICP-MS), accessory mineral Nd and Hf isotopes were measured by laser ablation multicollector (LA-MC)-ICP-MS, and whole-rock geochemistry was measured by X-ray fluorescence spectrometry (XRF) and laser ablation quadrupole (LA-Q)-ICP-MS. Detailed analytical methods are presented in the Appendix, and representative SEM images of sample grains with labeled spot analyses are provided in Supplementary Data Electronic Appendix 3 (supplemen tary data are available for downloading at http://www. petrology.oxfordjournals.org).

### **RESULTS**

## Whole-rock geochemistry

Geochemical data for ultrapotassic rock samples are shown on variation diagrams in Fig. 3, and presented in full in Table 2. TiO<sub>2</sub>, Fe<sub>2</sub>O<sub>3</sub>, MnO, MgO, CaO, and P<sub>2</sub>O<sub>5</sub>, compatible trace elements (e.g. Cr, V), and incompatible trace elements (e.g. Sr, Ba, LREE) decrease in abundance with increasing silica content; Al<sub>2</sub>O<sub>3</sub> and Na<sub>2</sub>O contents increase with increasing silica content; K2O, high-fieldstrength elements (HFSE; e.g. Zr, Nb, and Ta), heavy rare earth elements (HREE), and actinides (Th, U) do not show demonstrable trends. The ultrapotassic rocks are enriched in LREE by ~500-1000 times chondritic values, and in HREE by  $\sim$ 10–50 times chondritic values (Fig. 4). They display chondrite-normalized REE patterns with steep negative slopes (La/Yb ranging from 18 to 174), and without a significant Eu anomaly. Carbonatite from the MPIS is highly enriched in LREE, containing ~500 000  $\times$  chondritic values, with a La/Yb ratio of  $\sim$ 15 000 (Fig. 4). MPIS carbonatite whole-rock data are provided in Supplementary Data Electronic Appendix 4.

# Titanite textures, U-Pb, trace elements, and Nd isotopes

Titanite is present in most fresh ultrapotassic rock samples collected at Mountain Pass as translucent, euhedral

to subhedral, dark brown to golden crystals up to ~2 mm (Fig. 5a and b). Interstitial grains are common in coarse-grained samples, and euhedral matrix grains are typical in fine-grained samples (Fig. 5a and b). Titanite is absent in most samples that contain significant monazite and rutile (e.g. MP-P0913-2), with one exception (MP-P0913-10B). Titanite grains in some samples contain inclusions of clinopyroxene or apatite (Fig. 5a and b) and small (<2 µm) inclusions of monazite (Fig. 5c): monazite inclusions are most common in samples that appear to have undergone alteration (see above description of alteration textures in syenite). Grains with small monazite inclusions were typically avoided for analysis. Titanite in most samples appears unzoned in BSE images, but some grains appear to be weakly zoned (Fig. 5d). Where identified, specific zones were targeted for U-Pb, trace element and Nd isotopic analysis, but no consistent age, trace element, or isotopic pattern with respect to zonation was observed. Similarly, core and rim regions of grains are indistinguishable in terms of their age, trace element, and Nd isotopic composition.

Representative titanite geochronology data are presented in Table 3, and complete titanite LASS-ICP-MS data (including trace element data) are reported in Supplementary Data Electronic Appendix 5. LASS-ICP-MS U-Pb data from 10 titanite samples yielded singlepopulation [i.e. mean square weighted deviation (MSWD)  $\sim$  1] isochrons ranging from 1429  $\pm$  10 to  $1385 \pm 18 \,\mathrm{Ma}$  (Fig. 6). MP-P0714-17 has relatively little spread in U/Pb and <sup>207</sup>Pb/<sup>206</sup>Pb ratios, leading to a relatively imprecise isochron age of  $1358 \pm 71 \, \text{Ma}$ . Two samples have MSWD = 1.7, larger than expected for a single age population, and yield apparent 'errorchrons' of 1410  $\pm$  17 and 1367  $\pm$  9 Ma (MP-P0714-16 and MP-P0714-26). Subdividing the analyses into two single populations based on their relative 207Pb-corrected <sup>206</sup>Pb/<sup>238</sup>U date yields dates that broadly overlap within uncertainty for MP-P0714-16, and yields dates of 1410  $\pm$  17 (n = 8, MSWD = 0.3) and 1363  $\pm$  7 Ma (n = 27, MSWD = 1.0) for MP-P0714-26 (Fig. 6). In general, the position of each analysis in Tera-Wasserburg space correlates with U content (Fig. 6), suggesting that the degree of discordance in single analyses is due to the radiogenic Pb/common Pb ratio, as opposed to inheritance.

Chondrite-normalized REE profiles for titanite are characterized by LREE enrichment, with a negative LREE to HREE slope and no notable Eu anomaly (Fig. 7a). Zr-in-titanite apparent temperatures form single populations in only three samples (MP-P0913-10C weighted mean =  $859 \pm 9^{\circ}$ C; MP-P0714-17 weighted mean =  $875 \pm 8^{\circ}$ C; MP-P0714-23 weighted mean =  $806 \pm 16^{\circ}$ C) (Ti and Si activities assumed to be 0-8 and unity, respectively; see the Appendix for analytical details). Apparent temperatures in other samples range from  $\sim 950-850$  to  $700-650^{\circ}$ C (Fig. 7b). There is no consistent correlation observed between apparent Zr-intitanite temperature and either the trace element

(continued)

Downloaded from http://petrology.oxfordjournals.org/ by guest on September 23, 2016

_
ξŝ
e data
ЭС
ᅙ
SO
Ξ
Ξ
2
a
ž
a,
/ data,
ronology
픙
ŭ
Ξ
엉
geoc
5
ō
ati
8
∹
g
믕
Ž
=
풉
Ε
Sa
y of
>
na
ī
Sur
رن
<b>P</b>
š
Ta

date : Callinal y	or regulation of the control of the	table is called in the state of	, ממנמ, ועם מוום ווו וכ	מנסלס ממנמ					
Sample	Rock type	Location	Coordinates	Field context	Titanite	Zircon	Monazite	Accessory	Zircon
					age (ivia)	age (ivia)	(Ma)	εNd <sub>i</sub> (mean)	(mean)
MP-L0613-BDAY	biotite	Birthday mine	35.48916 N,	massive	I	$1425\pm5^*$	1	1	$1.6\pm0.5$
MP-L0613-BDAY2	snonkinite bastnäsite–	Birthday mine	35.48916 N,	body dike in	1	1	1396 ± 161	I	I
	barite	•	115 53627 W	shonkinite					
MP-P0913-SQ1	carbonatite bastnäsite-	Sulphide Queen	35.46971 N,	massive	I	I	1371 ± 10	$-2.9 \pm 0.13$	I
	barite	(parking lot near	115·52961 W	body (?)				(monazite &	
MP-P0913-1A	biotite	Birthday mine	35.48911 N,	massive body	1	1	1		I
GL 01000 GM	shonkinite	00:00	115-53628 W	<u>:</u> :		7			
	barite		115-53627 W	shonkinite		discoldant			l
	carbonatite								
MP-P0913-2	amphibole svenite	Groaner stock	35.46479 N, 115.52261 W	massive body	I	discordant	$1376 \pm 361$	1	I
MP-P0913-4	garnet-biotite- sillimanite	$\sim$ 170 m SW of Groaner stock	35.46244 N, 115.52376 W	host rock	ı	~1800–1660	1693 ± 8 (mean <sup>207</sup> Pb/	I	1
	gneiss						<sup>206</sup> Pb age)		
MP-P0913-5A	leucosyenite	Corral stock	35.46213 N, 115.52045 W	massive body	$1406 \pm 24$	1416 ± 9*	1	-9·6 ± 1† (titanite)	$1.9 \pm 0.7$
MP-P0913-5B	granite	Corral stock	35.46213 N,	m-scale host	I	$\sim \! 1820 \!\!-\!\! 1640$	I		I
MP-P0913-6	biotite	dike ∼50 m W	35.46218 N,	dike in host	$1429 \pm 10$	1423 ± 7#	I	$-5.8 \pm 0.91$	$2 \pm 0.5$
	melanosyenite	of Corral stock	115·52153 W	rock				(titanite)	
MP-P0913-7	syenite	Mexican Well	35·46608 N, 115·51612 W	massive body	I	discordant	$1401 \pm 321$	1	I
MP-P0913-9B	leucosyenite	dike at W edge	35-45592 N,	dike in host	I	discordant	1	1	1
MP-P0913-10A	biotite	Tors stock	35.45634 N,	enclave in	$1402\pm13$	discordant	1	1	I
	shonkinite		115.51416 W	syenite					(
MP-P0913-10B	biotite– amphibole	l ors stock	35·45634 N, 115·51416 W	massive body	1398 ± 14	1411 ± 8‡	I	$-4.7 \pm 0.4$ (titanite)	1.2 ± 2.3†
200000000	syenite	, o o o o o	DE AEGOG NI	() () () () () () () () () () () () () (	1001	1450 + 7+			- -
JUI10913-100	shonkinite	I OFS SLUCK	35:45656 N, 115:51418 W	dike iii syeniite	0	+7 ← 1430	I	-4 ± 0:4 (titanite)	n - - -
MP-P0913-10D	biotite– amphibole	Tors stock	35·45636 N, 115·51418 W	enclave in shonkinite dike	1401 ± 12	I	I	$-4.1\pm0.5$ (titanite)	I
	syenite								

Downloaded from http://petrology.oxfordjournals.org/ by guest on September 23, 2016

Table 1: Continued									
Sample	Rock type	Location	Coordinates	Field context	Titanite age (Ma)	Zircon age (Ma)	Monazite Th-Pb age (Ma)	Accessory mineral «Nd; (mean)	Zircon ɛHf <sub>i</sub> (mean)
MP-P0913-12	feldspar augen gneiss	host rock ~360 m NNW of Birthday mine	35·49240 N, 115·53518 W	hostrock	I	~1820–1765	I	I	1
MP-P0714-15	quartz syenite	Mineral Hill stock	35·45159 N, 115·48979 W	massive body	l	discordant	I	I	I
MP-P0714-16	biotite shonkinite	Tors stock	35-45551 N, 115-51433 W	massive body	$1413 \pm 16$	I	I	$-7.3 \pm 1.31$ (titanite)	ı
MP-P0714-17	leucosyenite	Tors stock	35·45664 N, 115·51430 W	dike intruding shonkinite dike in svenite	1358 ± 71	I	I	$-5.5\pm0.61$ (titanite)	I
MP-P0714-19	biotite shonkinite	Corral stock	35-46223 N, 115-51896 W	massive body	$1414 \pm 19$	discordant	I	$-4.2 \pm 0.51$ (titanite)	
MP-P0714-21	biotite– amphibole melanosvenite	Mexican Well stock	35.46631 N, 115.51594 W	enclave in syenite	I	1407 ± 11*	I		0.8 + 0.9
MP-P0714-22A	biotite– amphibole shonkinite	Wheaton stock	35·46063 N, 115·50265 W	massive body	$1404\pm12$	I	I	$-4.6\pm0.71$ (titanite)	1
MP-P0714-23	leucosyenite	Wheaton stock	35·46153 N, 115·50457 W	massive body	$1406\pm26$	discordant	I	I	ı
MP-P0714-26	biotite shonkinite	Birthday stock	35.48844 N, 115.53650 W	massive body	1410 ± 17	1434 ± 10‡	I	$-5.6 \pm 1.71$ (titanite)	$2.2 \pm 1$

\*U-Pb concordia age.

†MSWD≫1. ‡Mean <sup>207</sup>Pb/<sup>206</sup>Pb age. Stock names in the 'location' column are shown in Fig. 1b. Mean εNd<sub>i</sub> and εHf<sub>i</sub> values are weighted means of all analyses in a sample. Titanite ages are U–Pb isochron lower-intercept dates.

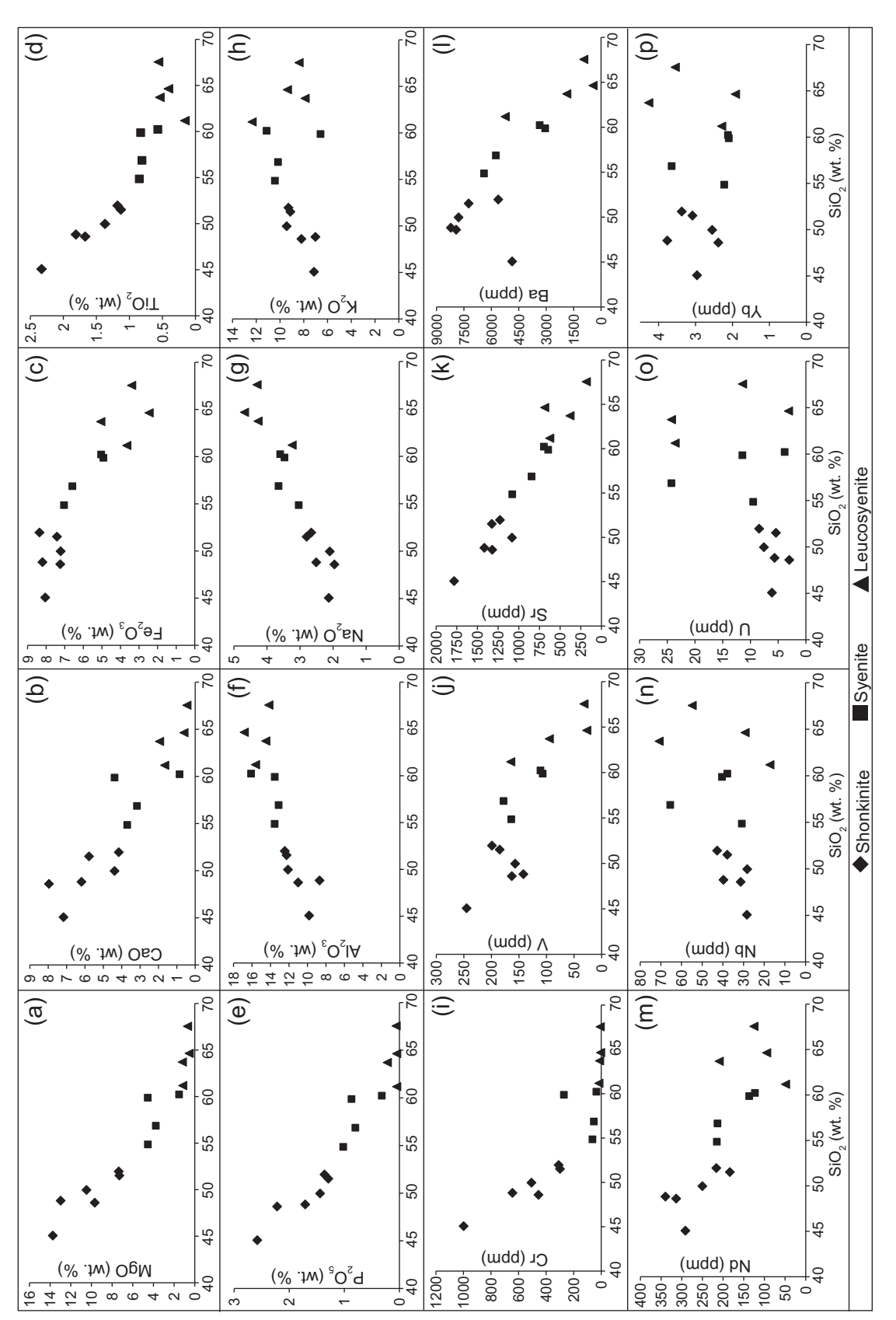


Fig. 3. Whole-rock major and trace element variations versus silica for MPIS ultrapotassic rocks. (a–h) Major elements; (i–p) trace elements.

Table 2: Whole-rock geochemical data

Sample:	MP- PO913-2	MP- PO913-5A	MP- PO913-6	MP- PO913-9B	MP- PO913-10A	MP- PO913-10B
wt%						
SiO <sub>2</sub>	60-01	63-69	59.99	64.54	51.87	56.76
TiO <sub>2</sub>	0.57	0.54	0.83	0.41	1.18	0.81
	16.04	14·50	13.56	16.81		13·10
Al <sub>2</sub> O <sub>3</sub>					12.43	
Fe <sub>2</sub> O <sub>3</sub>	5.02	5.06	4.93	2.46	8.35	6.58
MnO	0.07	0.02	0.07	0.01	0.11	0.06
MgO	1.51	1.20	4.56	0.54	7.35	3.76
CaO	0.85	1.94	4.40	0.61	4.15	3.16
Na <sub>2</sub> O	3.59	4.27	3.48	4.67	2.66	3.64
K <sub>2</sub> O	11.09	7.89	6.60	9.37	9.27	10.15
$P_2O_5$	0.32	0.22	0⋅87	0.05	1⋅36	0.80
Total	99.07	99.32	99.29	99.47	98.73	98.83
ppm						
Rb	444	347	228	446	658	568
Sc	3	4	12	0	22	13
V	111	95	107	27	199	178
Ni	10	4	72	0	106	64
Ga	17	22	17	19	17	17
Cu	53	38	64	38	75	100
Zn	119	78	111	45	183	106
Cr	35.2	11.9	271.0	4.7	309.0	53.4
Sr	697	381	645	687	1228	846
Y	32.5	67.7	34.0	25.9	57.2	56.8
Zr	508	1176	496	530	845	946
Nb	37.9	70.9	40.4	29.3	42.8	65.5
Cs	3.2	2.7	3.0	2.4	15.8	7.0
Ba	3356	1874	3054	437	5622	5753
La	148.5	259.6	160.4	88.8	224.6	190.3
Ce	289.4	492.3	307.5	195.2	481.5	430.9
Pr	32.6	56.8	36.0	24.7	55.4	52.4
Nd	123.0	209.4	136.8	94.6	216.4	213.6
Sm	21.2	36.2	22.9	15·3	39.0	41.3
Eu	4·79	8.28	5·15	3.84	8.99	9.34
Gd	14·8	26.8	16·2	11.5	27.9	29.6
Tb	1.59	3·11	1.64	1.31	27.9	3.07
					2.62 12.52	3.07 13.72
Dy	7.30	14.73	7.35	5.92		
Ho	1.146	2.359	1.194	0.942	2.021	2.125
Er -	2.82	5.65	2.82	2.38	4.59	4.95
Tm	0.341	0.707	0.338	0.301	0.541	0.589
Yb	2.12	4.27	2.10	1.92	3.37	3.65
Lu	0.279	0.569	0.296	0.226	0.464	0.514
Hf _	11.2	26.5	12.8	11.9	19.8	24.2
Та	27.6	22.3	22.9	11.3	12⋅5	16.1
Pb	154.0	60⋅8	87⋅1	36.1	91.1	57⋅0
Th	45.8	301.9	100.6	42.8	120-2	184.3
U	3.8	24.3	11.5	3⋅1	8.4	24.3

(continued)

composition or the <sup>207</sup>Pb-corrected <sup>206</sup>Pb/<sup>238</sup>U date of single LASS-ICP-MS spots. However, the two youngest samples in terms of cross-cutting relationships and titanite U–Pb dates (MP-P0913-10C and MP-P0714-17) have some of the highest (>800°C) and the most consistent apparent Zr-in-titanite temperatures.

In situ Nd isotopic measurements on titanite from three ultrapotassic samples from the Tors stock give single population weighted means of  $\varepsilon$ Nd<sub>i</sub>: MP-P0913-10B= $-4\cdot7\pm0.4$  (MSWD= $1\cdot3$ , n=20); MP-P0913-10C= $-4\pm0.4$  (MSWD=0.5, n=20); MP-P0913-10D= $-4\cdot1\pm0.5$  (MSWD= $1\cdot5$ , n=20), (Fig. 8). These three samples also yield the youngest U–Pb isochron dates in the MPIS, and contain some of the largest titanite crystals of the studied samples. In contrast, the other seven samples yield dispersed  $\varepsilon$ Nd<sub>i</sub> values from approximately -2 to -13, with a range of up to  $\sim$ 9 epsilon units

within a single sample (-2 to -11 in MP-P0714-26; Fig. 8). For four of the seven samples, the majority of analyses (66 of 71 spots) fall between -3.5 and -7. The remaining three samples yield the most scattered, and negative, εNd<sub>i</sub> values (as low as -13); one of these samples (MP-P0913-5A) also contains abundant xenoliths of host granite and gneiss as well as abundant inherited (~1700-1640 Ma) zircons. The other two samples (MP-P0714-16 and MP-P0714-26) also do not yield single-population U-Pb isochrons, indicating a possible relationship between the disturbance of the U-Pb and Nd isotopic systems. In general, more primitive and more consistent  $\epsilon Nd_i$  is associated with larger crystals; however, there is no apparent relationship between εNd<sub>i</sub> and position in crystals or location of samples in the field area. In the oldest (~1430-1420 Ma) and youngest (1380-1370 Ma) rocks, εNdi is typically lower with

Table 2: Continued

Table 2: Co	ontinued							
Sample:	MP- PO913-10C	MP- PO913-10D	MP- P0714-16	MP- P0714-17	MP- P0714-19	MP- PO913-22A	MP- PO714-23	MP- P0714-26
wt%								
SiO <sub>2</sub>	51.44	54.66	49.90	60.96	48.56	48.92	67.47	45.30
TiO <sub>2</sub>	1.13	0.85	1.37	0.16	1.67	1.81	0.56	2.34
$Al_2O_3$	12.24	13.50	12.09	15.56	11.00	8.71	14.16	9.87
Fe <sub>2</sub> O <sub>3</sub>	7.41	7.01	7.21	3.65	7.23	8.22	3.40	8.09
MnO	0.10	0.07	0.07	0.04	0.07	0.17	0.00	0.06
MgO	7.29	4.52	10.47	1.17	9.67	13.01	0.70	13.81
CaO	5.77	3.69	4.38	1.65	7·95	6.20	0.45	7.21
Na <sub>2</sub> O	2.80	3.03	2.10	3.23	1.96	2.51	4.29	2.14
K <sub>2</sub> O	9.12	10.39	9.43	12·31	8.19	7.03	8.39	7.18
$P_2O_5$	1.29	1.02	1.44	0.05	2.22	1.71	0.06	2.59
		98·74		98·78	98·52	98·29		98.60
Total	98.57	98.74	98.46	90.70	96.52	98.29	99.48	98.00
ppm	CO 4	CEO	CEO	670	077	204	220	405
Rb	604	652	652	679	277	364	329	435
Sc	20	15	16	5	22	20	0	21
V	185	164	157	165	163	142	32	245
Ni	99	105	478	0	207	396	0	475
Ga	16	20	17	20	16	16	22	17
Cu	161	147	95	47	136	30	29	77
Zn	141	132	133	46	130	194	37	112
Cr	299.3	63⋅8	506⋅4	16⋅8	455∙4	644-4	7.3	998.7
Sr	1326	1079	1082	626	1322	1417	183	1783
Υ	50.9	44.4	50⋅7	22.8	47.7	63⋅1	39⋅1	58.4
Zr	644	420	516	1235	420	423	1124	492
Nb	37.9	30⋅8	28.2	17⋅3	31.4	39.7	54.9	28.4
Cs	13⋅6	10∙7	11.9	6.0	7.6	6.9	2.6	7.8
Ba	7241	6402	7793	5243	7926	8214	943	4863
La	191.2	217.2	248.5	42.8	354.8	655.3	197.1	307.0
Ce	407.4	464-1	555.5	90.9	722.4	1056.5	356.0	661.4
Pr	46.8	54.4	63.4	11.9	82.6	100.0	37⋅2	74.5
Nd	183.6	215.1	250.1	48.9	313⋅5	339.5	125-4	291.2
Sm	32.7	38⋅5	42.6	10.0	47.9	49.3	19.4	48.3
Eu	7.67	8.32	9.56	2.87	11.43	10.10	4.17	10.89
Gd	23.6	26.2	30.4	8.1	31.1	33.6	13.4	33.9
Tb	2.42	2.49	2.90	0.92	2.80	3.14	1.54	3.05
Dy	11.12	10.58	11.81	4.36	11.47	13.51	7.48	13.27
Ho	1.754	1.560	1.727	0.756	1.720	2.048	1.296	1.963
Er	4.14	3.40	3.85	1.96	3.75	4.95	3.56	4.38
Tm	0.488	0.384	0.435	0.322	0.408	0.600	0.553	0.529
Yb	3.08	2.22	2.55	2.29	2.38	3.77	3.55	2.96
Lu	0.417	0.310	0·328	0.384	0·295	0.521	0·519	0.380
Hf	15.6	11.9	13.4	43.1	10.0	10.9	26.2	11.7
Та	13.8	13.3	10·1	43·1 14·9	12·6	14.5	26·2 15·4	11.7
Pb	255.7	83·4	45.6	687·0	75·8	23·4	28·3	45.5
Th					75·8 39·6	23·4 81·3		
	74.0	64·3	100·3	407·6			104·9	58.8
U	5.4	9.5	7.6	23.6	3.0	5.7	11.4	6⋅1

Reported values for major element oxides and Rb to Zn were measured by XRF; reported values for Cr to U were measured by LA-Q-ICP-MS.

increasing whole-rock silica content (Fig. 8). In general, samples with older dates have lower  $\epsilon Nd_i$  values (Fig. 8). Representative examples of titanite Nd isotopic data are shown in Table 4, and the complete set of titanite Nd isotopic data is presented in Supplementary Data Electronic Appendix 6.

# Zircon textures, U-Pb, trace elements, and Hf isotopes

Zircon in Mountain Pass rocks is diverse in morphology. Metamict, pseudo-octahedral, opaque grains are abundant in most samples, and do not luminesce in CL, but some grains show irregular, blotchy CL-bright domains (Fig. 9a and b). Translucent, pink to reddish-brown,

rounded or anhedral to euhedral grains that range from  $30\,\mu m$  to  $3\,mm$  in size are also present (Fig. 9c), but are less common. Some show typical oscillatory or sector zoning in CL (e.g. Fig. 9d), and others show irregular zoning (e.g. Fig. 9e). Zoning patterns do not appear to correlate with either whole-rock composition or age.

Representative zircon geochronology data are presented in Table 5, and the complete set of zircon LASS-ICP-MS data (including trace element data) is given in Supplementary Data Electronic Appendix 7. Zircon from 14 samples of Mountain Pass shonkinite and syenite are characterized by moderate to high U ( $\sim$ 300–10000 ppm), radiogenic Pb loss, high common Pb content, high or variable LREE, highly variable Ti contents ( $\sim$ 10–450 ppm), and correspondingly variable apparent

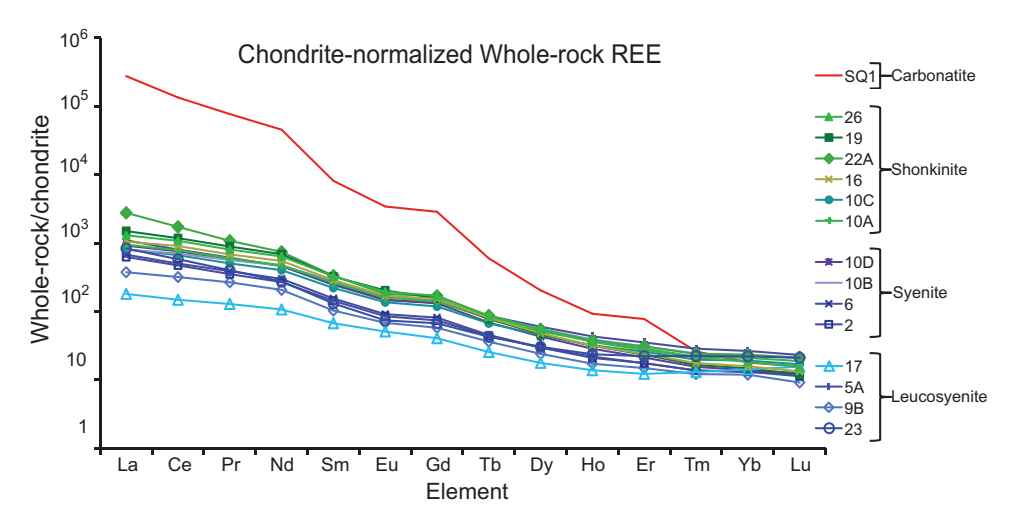


Fig. 4. Chondrite-normalized REE patterns for all whole-rock samples analyzed in this study.

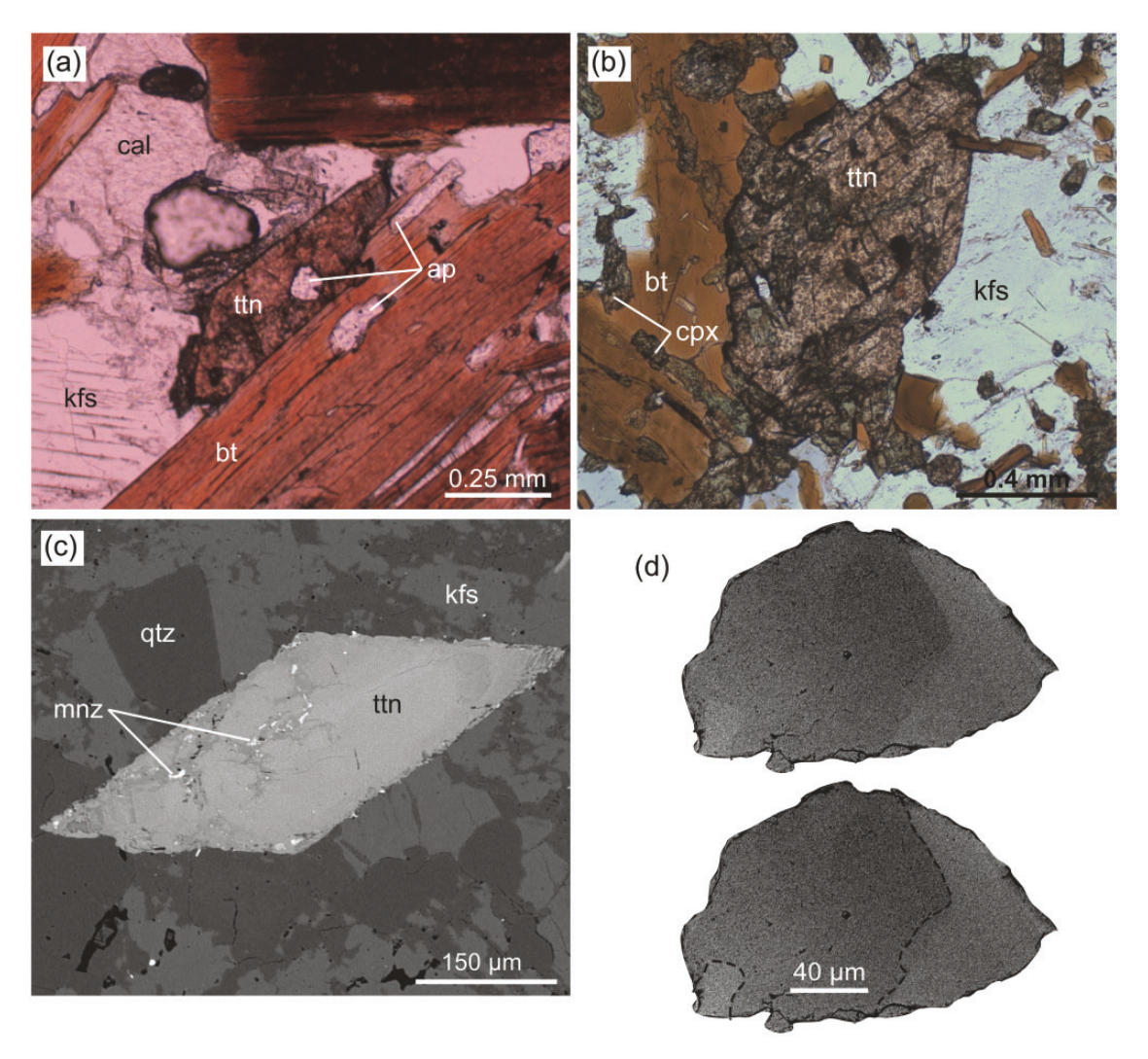


Fig. 5. Examples of typical titanite from MPIS ultrapotassic rocks. (a) Plane-polarized light (PPL) photomicrograph of euhedral titanite in shonkinite thin section (MP-P0714-19). (b) PPL photomicrograph of subhedral titanite in shonkinite thin section (MP-P0913-10C). (c) Back-scattered electron (BSE) image of titanite grain in leucosyenite thin section with veins containing monazite (MP-P0913-9B). (d) BSE image of zoned titanite in grain mount (MP-P0714-19). Zones are outlined by dashed lines in the lower image. ap, apatite; bt, biotite; cal, calcite; cpx, clinopyroxene; kfs, K-feldspar; mnz, monazite; qtz, quartz; ttn, titanite.

Downloaded from http://petrology.oxfordjournals.org/ by guest on September 23, 2016

 Table 3: Representative titanite LASS-ICP-IMS geochronology data

9	nepiden	וומוואם וו	ומווונם רא	101-00	hepieselitative titaliite EASS-IOF-IVIS geociii oliology da	2 6 6 6 6	5										
Spot	Pb	드	⊃	Th/U			Measured isotopic ratios	isotopic	ratios					Apparent isotopic ages (Ma)	otopic age	s (Ma)	
	(mdd)	(mdd)	(mdd)		<sup>207</sup> Pb/ <sup>206</sup> Pb	2σ%	<sup>207</sup> Pb/ <sup>235</sup> U	2σ %	<sup>206</sup> Pb/ <sup>238</sup> U	2σ %	Rho	<sup>207</sup> Pb/ <sup>206</sup> Pb age	2σ abs	<sup>206</sup> Pb/ <sup>238</sup> U age	2σ abs	<sup>207</sup> Pb-corrected <sup>206</sup> Pb/ <sup>238</sup> U age	2σ abs
MP-P09	13-6 titan	ite (spot	size= 40	um, shot	MP-P0913-6 titanite (spot size = 40 $\mu$ m, shot frequency=	= 4 Hz, sh	hot count=		100, laser energy=	3 mJ	at 100%)						
_	40.3	175	49.5	3.55	0.5027			2.66	0.4586	2.16	0.812	4249	62.9	2435	52.6	1390	39.4
2	45.3	247	59.2	4.16	0.45142	1.52	26.18	2.51	0.4207	2.00	0.797	4090	62.0	2265	45.3	1417	34.7
က	53.0	291	71.3	4.08	0.44319	1.51	25.39	2.53	0.415	2.03	0.803	4063	61.2	2240	45.5	1420	34.7
4	68.3	419	99.2	4.21	0.40812	1.51	22.02	2.53	0.3912	2.03	0.803	3939	59.3	2130	43.2	1429	33.2
2	43.4	211	53.5	3.93	0.4717	1.53	29.08	2.57	0.4491	2.07	0.804	4155	63.5	2393	49.6	1451	37.7
9	110.3	1219	177.0	06.9	0.17531	1.51	6.639	2.53	0.2748	2.02	0.801	2609	39.5	1566	31.7	1428	28.3
7	43.6	211	54.1	3.91	0.47983	1.51	30.03	2.54	0.454	2.04	0.804	4180	63.0	2415	49.3	1443	37.6
00	85.9	949	142.9	99.9	0.15106	1.51	5.609	2.55	0.2692	2.05	0.805	2358	35.7	1538	31.6	1441	28.8
6	83.9	947	160·8	5.90	0.15221	1.51	5.458	2.55	0.2607	2.05	0.804	2371	35.9	1495	30.6	1395	27.8
10	48.9	290	69.5	4.20	0.41797	1.51	22.98	2.56	0.3974	5.06	0.807	3975	0.09	2159	44.5	1426	33.9
1	59.4	492	44.2	11.20	0.45881	1.51	27.27	2.55	0.4312	2.05	0.804	4114	62.3	2313	47.4	1431	36.1
12	69.3	365	89.2	4.12	0.4522	1.57	27.09	2.76	0.4353	2.27	0.822	4092	64.3	2331	52.9	1462	39.3
13	94.1	1003	147.7	6.78	0.1904	1.61	7.459	5.66	0.2837	2.13	0.798	2746	44.1	1611	34.2	1445	30.2
14	87.5	686	146.0	6.77	0.153	1.51	5.624	2.53	0.2651	2.03	0.802	2380	36.0	1517	30.8	1417	28.0
15	34.3	94	26.7	3.53	0.6325	1.51	56.99	2.59	0.6534	2.10	0.811	4584	69.3	3244	0.89	1417	55.6
16	28.4	73	26.4	2.77	0.5954	1.51	49.12	2.57	0.5978	2.08	0.810	4497	67.9	3023	63.0	1442	50.1
17	37.7	159	45.9	3.47	0.4979	1.51	32.39	2.57	0.4724	2.08	0.809	4235	64.1	2496	51.9	1445	39.4
18	2.09	989	117.1	5.87	0.13786	1.52	4.967	2.55	0.2614	2.05	0.803	2201	33.5	1498	30.7	1423	28.3
19	63.7	721	123.2	5.88	0.13648	1.51	4.927	2.56	0.2632	5.06	908.0	2183	33.1	1507	31.1	1435	28.7
20	72.8	333	149.7	2.22	0.38206	1.51	19.54	2.55	0.3718	2.05	908.0	3840	6.73	2040	41.9	1423	32.3
21	66.1	392	72.2	5.49	0.48209	1.51	29.61	2.63	0.4443	2.15	0.818	4187	63.4	2372	51.1	1406	38.0
22	31.6	123	36.7	3.38	0.5182	1.51	34.98	2.65	0.4901	2.18	0.821	4294	65.0	2573	2e·0	1433	41.8
23	41.6	188	53.4	3.54	0.48186	1.51	29.85	2.56	0.4509	5.06	908.0	4187	63.4	2401	49.5	1427	37.6
24	46.6	293	6.96	3.02	0.3327	1.54	15.78	5.66	0.3464	2.17	0.816	3630	22·8	1919	41.6	1438	32.7
25	52.8	281	61.5	4.58	0.47583	1.51	29.16	2.56	0.4451	5.06	0.808	4168	62.8	2375	49.1	1427	37.1
56	39.3	149	43.0	3.47	0.5386	1.53	37.61	2.61	0.5052	2.12	0.810	4350	99	2638	22·8	1410	42.5
27	103·1	1131	174.9	6.47	0.15656	1.57	5.778	2.60	0.2693	2.07	0.796	2419	38.0	1538	31.8	1432	28.9
28	86.3	922	99.4	9.31	0.21349	1.52	8.527	2.54	0.2897	2.03	0.802	2932	44.5	1641	33.4	1432	28.8
29	52.9	296	72.0	4.11	0.43585	1.51	24.85	2.54	0.4128	2.04	0.803	4038	61.1	2230	45.5	1432	34.8
30	52.6	257	2.79	3.80	0.47042	1.51	28.81	2.56	0.4427	2.07	0.807	4151	62.7	2365	48.9	1435	37.0
31	83.8	909	79.0	7.63	0.4611	1.56	27:39	2.66	0.4317	2.16	0.810	4121	64.4	2315	49.9	1426	37.5
																00)	(continued)

Downloaded from http://petrology.oxfordjournals.org/ by guest on September 23, 2016

	0	פַע
	2	=
	100	5
	١	ز
	Ċ	י נו
	200	2
I	ŕ	U

apie	lable 3: confinited	nar															
Spot	Pb	Th	⊃	Th/U			Measured isotopic ratios	l isotopic	ratios					Apparent isotopic ages (Ma)	otopic ages	(Ma)	
	(mdd)	(mdd)	(mdd)		<sup>207</sup> Pb/ <sup>206</sup> Pb	2σ%	<sup>207</sup> Pb/ <sup>235</sup> U	2σ %	<sup>206</sup> Pb/ <sup>238</sup> U	2σ %	Rho	<sup>207</sup> Pb/ <sup>206</sup> Pb age	2σ abs	<sup>206</sup> Pb/ <sup>238</sup> U age	2σ abs	<sup>207</sup> Pb-corrected <sup>206</sup> Pb/ <sup>238</sup> U age	2σ abs
MP-PC	1913-10C t	itanite (sp	oot size= 4	10 µm, sh	MP-P0913-10C titanite (spot size $=$ 40 $\mu m$ , shot frequency $=$ 4 H	y = 4  Hz,	. shot count	= 100,	laser energy = $3  \text{mJ}$	y = 3 m	l at 75%)						
_	30.1	166	61.9	2.64	0.4358	1.52	23.19		0.3824	2.04	0.802	4037	61.4	2089	42.7	1383	33.9
2	32.5	197	66.2	2.92	0.3964	1.53	19.81	2.56	0.3587	2.06	0.804	3895	59.4	1978	40.8	1385	32.3
က	23.7	104	39.0	2.65	0.5671	1.51	38.66	2.67	0.493	2.20	0.823	4426	67.0	2586	9.99	1380	45.5
4	25.5	110	41.7	2.61	0.5623	1.55	39.06	2.76	0.4994	2.28	0.827	4413	68.4	2613	9.69	1412	47.1
വ	28.1	153	55.1	2.75	0.4463	1.52	24.02	2.64	0.3876	2.16	0.817	4073	61.9	2113	45.6	1376	35.5
9	38.6	231	74.6	3.07	0.4073	1.52	20.74	2.61	0.3671	2.12	0.812	3936	0.09	2017	42.7	1392	33.6
7	35.7	178	65.3	2.72	0.5012	1.52	30.08	2.59	0.4329	2.10	0.811	4245	64.3	2321	48.8	1389	38.8
∞	51.0	279	102·1	2.73	0.44484	1.51	23.86	2.59	0.387	2.10	0.811	4068	61.6	2111	44.4	1378	34.8
െ	24.7	114	40.3	2.83	0.5528	1.54	36.21	2.61	0.4745	2.11	0.807	4389	2.79	2505	52.8	1371	43.2
10	23.6	107	39.6	2.68	0.5527	1.52	36.81	5.66	0.4825	2.19	0.821	4388	8.99	2540	929	1393	44.4
1	58.2	348	182.8	1.90	0.3231	1.51	14.26	2.54	0.3191	2.05	0.804	3585	54.2	1787	36.5	1378	29.6
12	41.2	161	97.0	2.81	0.6325	1.52	50.83	2.53	0.5815	2.03	0.801	4584	69.5	2957	59.9	1391	53.8
13	25.3	123	47.5	2.61	0.4999	1.55	29.41	2.62	0.428	2.11	908.0	4241	9.59	2299	48.5	1377	38.6
14	26.2	134	43.6	3.09	0.5112	1.53	30.71	2.63	0.4353	2.14	0.813	4274	65.3	2331	49.8	1370	39.2
15	25.7	110	42.4	2.62	0.5547	1.52	37.16	2.60	0.485	2.12	0.813	4394	2.99	2551	54.0	1394	44.0
16	47.0	269	122.2	2.23	0.3881	1.52	19.07	2.49	0.3554	1.98	0.792	3864	58.8	1962	38.8	1390	31.2
17	28.1	126	20·8	2.51	0.5325	1.52	33.94	2.62	0.4603	2.14	0.815	4334	62.9	2443	52.2	1387	41.8
18	33.3	196	61.9	3.21	0.41205	1.52	21.28	2.67	0.3742	2.19	0.823	3954	0.09	2051	45.0	1407	35.0
19	39.0	252	76.9	3.31	0.3611	1.53	17.29	2.57	0.346	5.06	0.803	3754	57.5	1917	39.6	1411	31.7
20	52.8	285	107.7	2.67	0.4378	1.53	23.56	2.43	0.3882	1.89	0.777	4044	61.8	2116	39.9	1398	32.8
21	62.1	312	124.5	2.56	0.4809	1.52	27.5	2.41	0.4134	1.88	0.778	4184	63.5	2232	41.9	1379	34.9
22	66.2	343	129.9	2.67	0.46914	1.51	26.55	2.41	0.4083	1.87	0.778	4147	62.7	2209	41.4	1391	34.3
23	37.7	189	66.3	2.88	0.5079	1.53	31.39	2.44	0.4455	1.91	0.780	4264	65.2	2377	45.3	1410	38.2
24	27.4	134	43.0	3.16	0.5392	1.52	34.73	2.44	0.4665	1.90	0.782	4352	66.1	2470	47.0	1387	40.4
22	41.1	176	182.1	0.98	0.35225	1.51	16.345	2.42	0.3355	1.90	0.783	3717	56.1	1866	35.4	1387	28.9
56	24.5	115	41.4	2.80	0.5378	1.52	34.88	2.47	0.4703	1.95	0.788	4348	66.1	2487	48.4	1401	41.0
27	32.7	155	58.6	5.66	0.5212	1.52	32.69	2.44	0.4541	1.91	0.783	4302	65.3	2415	46.1	1400	39.0
28	53.5	267	80.4	3.36	0.54294	1.51	35.2	2.46	0.4694	1.94	0.789	4362	62.9	2483	48.2	1384	40.9
59	40.6	156	52.8	2.98	0.6534	1.53	55.24	2.47	0.613	1.94	0.787	4631	9.07	3084	0.09	1387	57.1

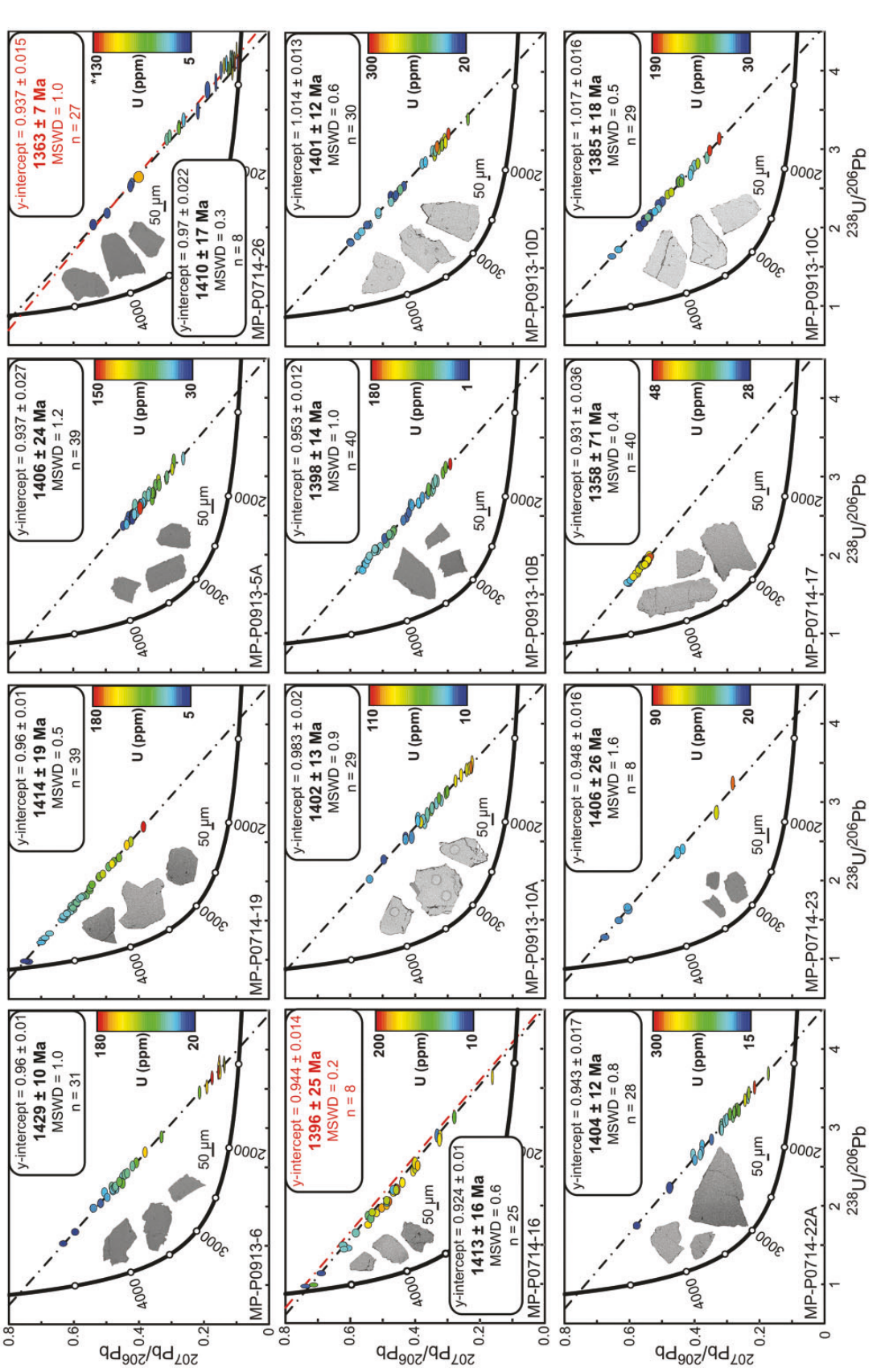
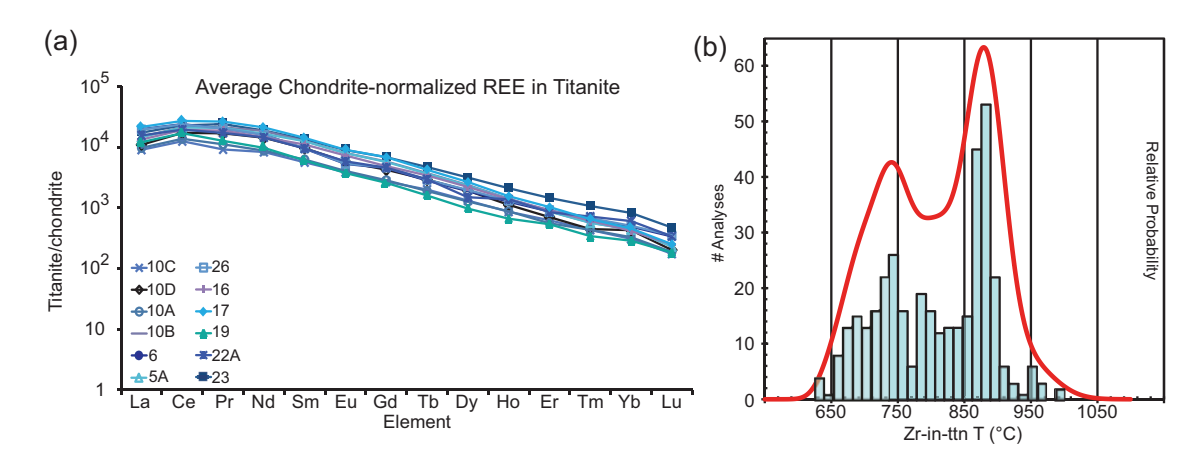


Fig. 6. Titanite U-Pb concordia plots for MPIS ultrapotassic rocks. Analyses are colored by U content; warmer colors represent higher concentrations. It should be noted that there are two age populations shown for MP-P0714-26 (top right corner) and MP-P0714-16 (left of middle row); the younger age populations are shown by red isochrons; also that for MP-P0714-26 the U-content scale does not include one analysis that has much higher U content (450 ppm vs <130 ppm). BSE images of representative grains are shown in each plot; it should be noted that scale is different for each plot.



**Fig. 7.** Titanite trace element plots. (a) Average chondrite-normalized REE patterns for titanite from all analyzed samples. (b) Probability distribution plot of Zr-in-titanite temperatures for all titanite samples calculated using the calibration of Hayden *et al.* (2008) with adjustment of activities for Si and Ti according to the Appendix.

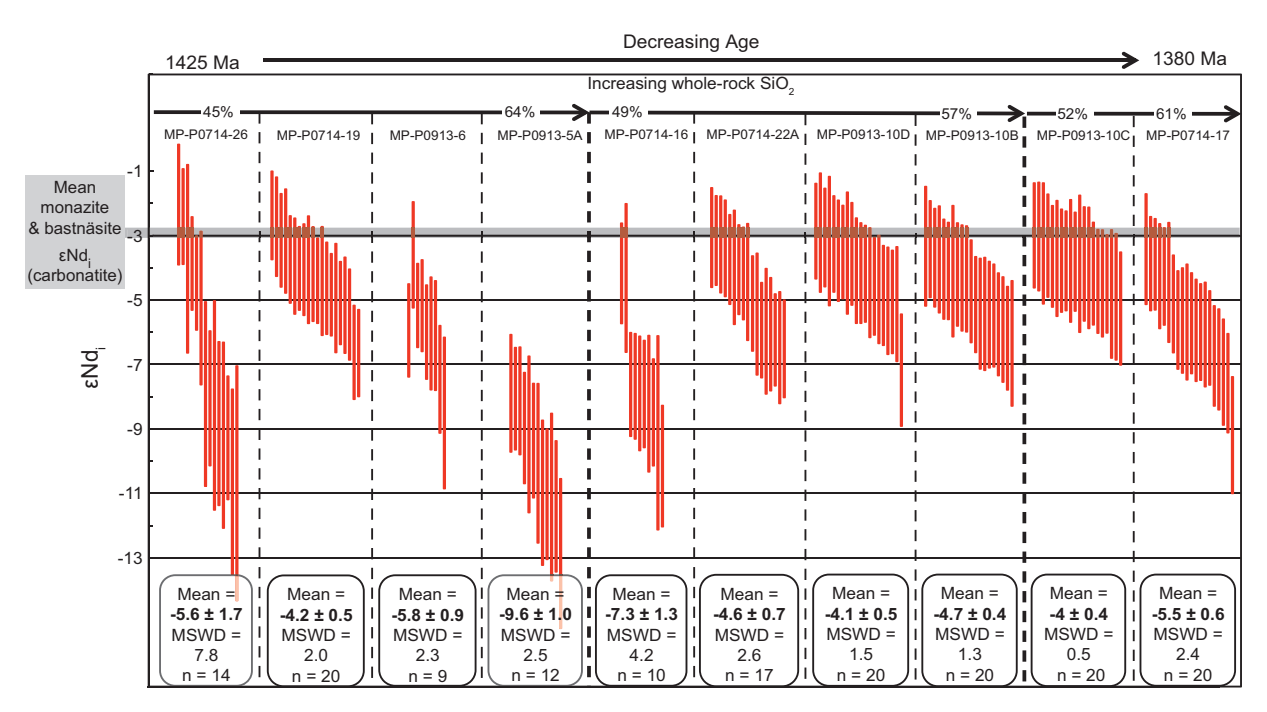


Fig. 8. Titanite Nd isotopic data for MPIS ultrapotassic rocks. Each set of analyses is from a single sample; weighted means are shown in boxes below each set of analyses. Samples are arranged by age, with age decreasing from left to right. Within each age group, samples increase in whole-rock silica content from left to right. Mean εNd<sub>i</sub> of monazite and bastnäsite from MPIS carbonatite is shown by the gray bar.

Ti-in-zircon temperatures (800–1500°C, Ti and Si activities assumed to be 0.8 and unity, respectively; see the Appendix for analytical details). Most of the U–Pb data are highly discordant on Tera–Wasserburg concordia diagrams, defining broad arrays that appear to be the result of a mixture of radiogenic Pb loss and high or variable common Pb content (Fig. 10a–f). In general, per cent discordance correlates positively with U content, LREE content, and mass-204 signal intensity (a proxy for common Pb content) (e.g. Fig. 10c and d). Zircon is present in only one carbonatite sample (MP-P0913-1B), and all crystals examined are metamict and do not yield meaningful U–Pb data. Of 15 samples, eight yielded

only discordant zircon U-Pb data (e.g. MP-P0913-10A, Fig. 10c and d).

A minority of zircons (134 of 436 analyses) from seven out of 15 MPIS rocks yielded small populations of concordant or near-concordant U–Pb dates, primarily from low- to moderate-U grains (~80–500 ppm). The dates primarily form two clusters; one at ~1460–1400 Ma, and another at 1800–1640 Ma (Fig. 10a and b), although one sample additionally yielded sparse analyses from 1600 to 1430 Ma (Fig. 10b). Elongate or rounded, colorless to brown zircons from two samples that contain gneissic or granitic xenoliths (MP-P0913-5A and MP-P0913-6; e.g. Fig. 2a) yield dates >1460 Ma and

(continued)

Downloaded from http://petrology.oxfordjournals.org/ by guest on September 23, 2016

Spot	146Nd (V)	Total Nd	144Sm	<sup>143</sup> Nd/ <sup>144</sup> Nd	2SE	<sup>143</sup> Nd/ <sup>144</sup> Nd std corr'd	2SE	145Nd/ 144Nd	2SE	147Sm/ 144Nd	2SE	<sup>147</sup> Sm/ <sup>144</sup> Nd std corr'd	2SE	2SE propagated	β (Sm)	β (Nd)	Age (Ma)	$^{\rm s}$ Nd $^{\rm s}$	2SE
MP-P	MP-P0913-SQ1 monazite	1 mona	zite																
_	1.537	6.59	1.0129	0.511105	37	0.511168	37	0.348420	20	0.049067	9/	0.047754	9/	2389	-1.406	-1.629	1380	-2.34	0.8
2	1.533	6.57	1.0132	0.511069	33	0.511132	33	0.348405	24	0.049064	99	0.047751	99	2388	4.1-	-1.6267	1380	-3.05	0.8
က	1.507	6.46	1.0042	0.511036	43	0.511099	43	0.348385	56	0.048656	9	0.047354	9	2369	-1.405	-1.6213	1380	-3.62	6.0
4	1.518	6.51	1.0042	0.511080	56	0.511143	26	0.348412	22	0.048656	92	0.047354	92	2370	-1.406	-1.6256	1380	-2.76	0.7
2	1.508	6.46	0.9964	0.511080	36	0.511143	36	0.348404	21	0.048255	63	0.046964	63	2349	-1.405	-1.6223	1380	-2.69	0.8
9	1.531	99.9	1.0049	0.511077	33	0.511140	33	0.348394	21	0.048680	140	0.047377	140	2373	-1.407	-1.6223	1380	-2.83	6.0
7	1.504	6.45	0.9962	0.511057	33	0.511120	33	0.348414	19	0.048250	140	0.046959	140	2352	-1.392	-1.6193	1380	-3.14	0.8
œ	1.532	6.57	1.0073	0.511096	33	0.511159	33	0.348388	24	0.048826	80	0.047519	80	2377	-1.411	-1.6188	1380	-2.48	6.0
6	1.524	6.53	1.0016	0.511060	32	0.511123	35	0.348414	22	0.048531	90	0.047232	8	2363	-1.405	-1.6183	1380	-3.13	0.8
10	1.511	6.47	0.9999	0.511065	51	0.511128	21	0.348402	24	0.048441	86	0.047145	86	2359	-1.405	-1.6192	1380	-3.02	<del>[</del>
11	1.519	6.51	1.0189	0.511080	38	0.511143	38	0.348403	24	0.049362	92	0.048041	92	2404	-1.404	-1.617	1380	-2.88	6.0
12	1.506	6.46	1.0177	0.511084	4	0.511147	40	0.348408	17	0.049300	130	0.047981	130	2403	-1.401	-1.6166	1380	-2.8	6.0
13	1.521	6.52	1.0212	0.511068	32	0.511131	32	0.348397	20	0.049450	140	0.048127	140	2410	-1.383	-1.615	1380	-3.13	0.8
14	1.513	6.49	1.0086	0.511081	53	0.511144	59	0.348409	22	0.048878	86	0.047570	86	2381	-1.412	-1.6182	1380	-2.78	0.7
15	1.54	6.61	1.0247	0.511092	44	0.511155	44	0.348423	28	0.049666	74	0.048337	74	2418	-1.409	-1.6171	1380	-2.7	_
16	1.527	6.54	0.9839	0.511098	38	0.511161	38	0.348420	23	0.047649	94	0.046374	94	2321	-1.404	-1.6262	1380	-2.24	6.0
17	1.428	6.12	9.60	0.511036	34	0.511099	34	0.348418	25	0.047320	120	0.046054	120	2306	-1.419	-1.6271	1380	-3.39	0.8
18	1.497	6.41	0.9804	0.511075	42	0.511138	45	0.348406	23	0.047500	110	0.046229	110	2314	-1.419	-1.6264	1380	-2.66	6.0
19	1.495	6.4	0.9917	0.511083	37	0.511146	37	0.348391	22	0.048072	75	0.046786	75	2340	-1.417	-1.6257	1380	-2.6	φ Θ
20	1.499	6.42	0.9792	0.51106	33	0.511123	33	0.348398	18	0.047434	62	0.046165	62	2309	-1.416	-1.6214	1380	-2.94	0.8
21	1.456	6.24	0.9718	0.511076	38	0.511139	38	0.348413	25	0.047080	140	0.045820	140	2295	-1.397	-1.6217	1380	-2.57	φ Θ
22	1.452	6.22	0.9718	0.511048	38	0.511111	88	0.348411	56	0.047080	130	0.045820	130	2295	-1.403	-1.6178	1380	-3.12	0.8
23	1.454	6.23	0.9749	0.511061	36	0.511124	36	0.348396	22	0.047230	110	0.045966	110	2301	-1.408	-1.6169	1380	-2.89	0.8
24	1.452	6.22	0.9759	0.511070	41	0.511133	41	0.348393	21	0.047257	66	0.045992	66	2302	-1.412	-1.6154	1380	-2.72	6.0
22	1.416	90.9	0.9632	0.511045	37	0.511108	37	0.348409	21	0.046700	120	0.045450	120	2276	-1.43	-1.6136	1380	-3.11	0.8
56	1.552	6.65	0.9778	0.511050	37	0.511113	37	0.348404	25	0.047386	70	0.046118	70	2307	-1.403	-1.6144	1380	-3.13	φ Θ
27	1.575	6.75	0.9838	0.511091	46	0.511154	46	0.348395	30	0.047708	74	0.046431	74	2323	-1.431	-1.616	1380	-2.38	_
28	1.543	6.61	0.9874	0.511063	38	0.511126	38	0.348405	9	0.047850	150	0.046570	150	2333	-1.406	-1.6135	1380	-2.96	6.0
59	1.568	6.72	0.9818	0.511121	38	0.511184	38	0.348410	21	0.047570	100	0.046297	100	2317	-1.406	-1.6169	1380	-1.77	φ Θ
30	1.617	6.93	0.9843	0.511089	32	0.511152	32	0.348402	18	0.047696	71	0.046420	71	2322	-1.386	-1.6146	1380	-2.42	0.8

Downloaded from http://petrology.oxfordjournals.org/ by guest on September 23, 2016

Table 4	Fable 4: Continued	panu																	
Spot	146Nd (V)	Total Nd	% 144Sm	143Nd/ 144Nd	2SE	<sup>143</sup> Nd/ <sup>144</sup> Nd std corr'd	2SE	<sup>145</sup> Nd/ <sup>144</sup> Nd	2SE	147Sm/ 144Nd	2SE	<sup>147</sup> Sm/ <sup>144</sup> Nd std corr'd	2SE	2SE propagated	β (Sm)	β (Nd)	Age (Ma)	εNd <sub>i</sub>	2SE
MP-PO	MP-P0913-6 titanite	tanite																	
_	1.047	4.62	2.464	0.511538	47	0.511583	47	0.348410	24	0.119500	1500	0.116473	1500	6014	-1.492	-1.6725	1420	9–	1.4
2	1.77	7.94	3.327	0.511842	33	0.511887	39	0.348401	23	0.161300	1700	0.157214	1700	8042	-1.4758	-1.6716	1420	-7.49	1.7
က	1.616	7.22	3.096	0.511809	52	0.511854	52	0.348409	23	0.150090	960	0.146288	096	7377	-1.4865	-1.6711	1420	-6.14	1.7
4	1.648	7.42	3.534	0.512005	33	0.512050	39	0.348415	22	0.171200	1800	0.166864	1800	8535	-1.4219	-1.6309	1420	90.9-	1.7
2	1.572	7.05	3.326	0.512038	33	0.512083	33	0.348395	22	0.161180	890	0.157097	830	7905	-1.4239	-1.6243	1420	-3.63	1.6
9	1.127	4.99	2.643	0.511612	44	0.511657	44	0.348418	23	0.127900	1400	0.124660	1400	6388	-1.486	-1.6651	1420	-6.05	1.5
7	1.189	5.26	2.634	0.511652	41	0.511697	41	0.348411	22	0.127700	1300	0.124465	1300	6358	-1.454	-1.6497	1420	-5.23	1.4
∞	1.483	6.57	2.722	0.511691	56	0.511736	56	0.348404	9	0.131940	930	0.128598	930	6497	-1.48	-1.6668	1420	-5.22	<del>ن</del>
6	2.137	89.6	3.83	0.512011	84	0.512056	84	0.348398	39	0.185660	830	0.180957	830	9806	-1.455	-1.6428	1420	-8.52	2.3
MP-PO	913-100	P-P0913-10C titanite	<b>.</b>																
_	0.428	1.905	2.892	0.511893	29	0.511938	29	0.348429	38	0.140110	540	0.136561	540	6849	-1.399	-1.618	1380	-3.03	1.7
2	0.438	1.952	2.923	0.511815	79	0.511860	79	0.348375	38	0.141600	1100	0.138013	1100	8869	-1.409	-1.6166	1380	-4.81	7
ო	0.617	2.757	3.126	0.511919	21	0.511964	51	0.348428	31	0.151470	620	0.147633	620	7408	-1.423	-1.6263	1380	-4.49	1.7
4	0.576	2.572	3.0983	0.511967	47	0.512012	47	0.34839	32	0.150120	320	0.146318	320	7323	-1.408	-1.6237	1380	-3.31	1.6
2	0.787	3.5	2.9464	0.511867	72	0.511912	72	0.348437	32	0.142790	360	0.139173	360	8969	-1.425	-1.6246	1380	4-	9:
9	0.63	2.79	3.025	0.511913	44	0.511958	44	0.348415	33	0.146740	730	0.143023	730	7188	-1.423	-1.617	1380	-3.79	15
	0.383	1.704	2.875	0.511852	67	0.511897	29	0.348415	33	0.139400	100	0.135869	100	2989	-1.403	-1.6064	1380	-3.71	<del>,</del>
	0.567	2.522	2.8853	0.511859	21	0.511904	21	0.348391	24	0.139820	160	0.136279	160	6816	-1.394	-1.6003	1380	-3.65	1.6
6	0.555	2.473	2.947	0.511858	20	0.511903	20	0.348411	33	0.142800	1000	0.139183	1000	7031	-1.418	-1.6206	1380	-4.18	1.6
10	0.527	2.344	2.87	0.511813	23	0.511858	53	0.348425	33	0.139100	1200	0.135577	1200	6884	-1.42	-1.616	1380	-4.42	1.6
	0.377	1.681	2.933	0.511816	77	0.511861	77	0.348381	32	0.142200	1100	0.138598	1100	7017	-1.412	-1.601	1380	-4.9	2
12	0.418	1.853	2.751	0.511795	26	0.511840	26	0.348418	43	0.133350	170	0.129972	170	6501	-1.405	-1.5859	1380	-3.78	1.6
	0.398	1.77	2.859	0.511836	83	0.511881	68	0.348389	46	0.138550	860	0.135041	860	6807	-1.386	-1.5959	1380	-3.88	2.1
	0.483	2.151	2.978	0.511891	44	0.511936	44	0.348475	56	0.144400	1000	0.140742	1000	7108	-1.418	-1.591	1380	-3.81	15
15	0.833	3.71	2.941	0.511839	44	0.511884	44	0.348418	22	0.142500	1100	0.138891	1100	7031	-1.402	-1.6065	1380	-4.5	15
16	0.659	2.948	3.153	0.511891	24	0.511936	54	0.348418	22	0.152800	2400	0.148930	2400	7824	-1.406	-1.6136	1380	-5.26	1.7
17	0.462	2.056	2.8478	0.511876	26	0.511921	26	0.348384	32	0.137980	340	0.134485	340	6733	-1.393	-1.5868	1380	-2.99	1.6
18	0.475	2.116	2.919	0.511894	72	0.511939	72	0.348402	59	0.141460	740	0.137877	740	6933	-1.388	-1.5926	1380	-3.24	1.9
19	0.408	1.821	2.852	0.511833	99	0.511878	99	0.348419	33	0.138240	720	0.134739	720	6775	-1.392	-1.5869	1380	-3.88	<del>,</del>
20	0.367	1.63	2.7958	0.511813	9/	0.511858	9/	0.348382	44	0.135430	150	0.132000	150	6602	-1.371	-1.5746	1380	-3.79	<del>ن</del>

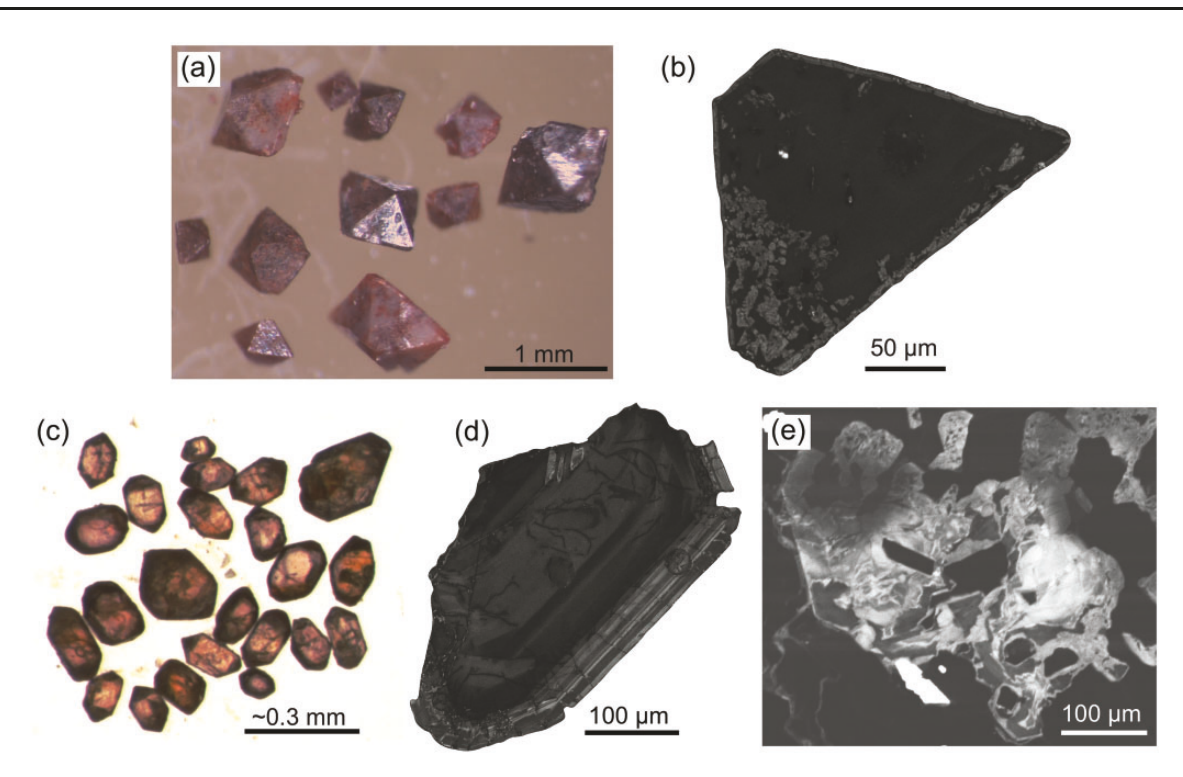


Fig. 9. Examples of typical zircon from MPIS ultrapotassic rocks. (a) Pseudo-octahedral, metamict zircons separated from shonkinite (MP-P0714-22A). (b) Cathodoluminescence (CL) image of metamict zircon grain (MP-P0714-17). (c) Euhedral, pink to reddishbrown zircons separated from melanosyenite (MP-P0913-6). (d) CL image of zircon in grain mount showing oscillatory zoning (MP-P0714-26). (e) CL image of anhedral zircon with irregular zoning pattern in shonkinite thin section (MP-P0913-10A).

have Th/U < 1; pink to reddish-brown, euhedral to anhedral zircon with low aspect ratios ( $\leq$ 2:1) yield dates < 1460 Ma and chiefly have Th/U > 1. Mean  $^{207}\text{Pb/}^{206}\text{Pb}$  and concordia dates < 1460 Ma range from 1458  $\pm$  7 to 1407  $\pm$  11 Ma (e.g. Fig. 10e and f; Supplementary Data Electronic Appendix 8). Only one sample gave > 10 concordant, Mesoproterozoic dates out of 30–40 analyses (MP-L0613-BDAY), yielding a concordia age of 1425  $\pm$  5 Ma (n=25; Supplementary Data Electronic Appendix 8). Where titanite and zircon occur in the same sample, concordant, Mesoproterozoic zircon dates overlap titanite dates within uncertainty in all cases except one (MP-P0913-10C). Multiple dates within single crystals are consistently similar.

Zircons that yield concordant and slightly discordant data have similar REE concentrations to typical igneous zircon from a variety of igneous rocks (e.g. Belousova *et al.*, 2002), and yield Ti-in-zircon apparent temperatures from ~600 to 850°C (Fig. 11a and b).

Zircons from three Mountain Pass host-rock samples are primarily colorless to brown and elongate or moderately rounded, and yielded zircon dates of  $\sim\!1820-1765\,\mathrm{Ma}$  (feldspar augen gneiss, sample MP-P0913-12),  $\sim\!1820-1640\,\mathrm{Ma}$  (coarse-grained alkali granite, sample MP-P0914-5B) and 1800–1660 Ma (garnet–biotite–sillimanite gneiss, sample MP-P0913-4) (Supplementary Data Electronic Appendix 8). U–Pb discordance is common in the host-rock zircons, and generally correlates positively with U content and mass-204 signal intensity, but  $\sim\!50-70\%$  of the zircon analyses are concordant.

Th/U is consistently < 1. Chondrite-normalized REE profiles are highly variable, and Ti-in-zircon apparent temperatures mostly range from 650 to 800°C (Supplementary Data Electronic Appendix 8).

The EHfi values from Mesoproterozoic zircons typically range from ~0.5 to 3. Five of seven samples analyzed yield single populations (MSWD  $\sim$  1; Fig. 12). Two samples with fewer analyses have higher MSWD owing to one or two outlying analyses (e.g. MP-P0913-10B, Fig. 12). Taken as a whole, data from all the samples give a weighted mean of  $1.9 \pm 0.2$  (MSWD=0.9; seven of 76 analyses rejected; Fig. 12). EHfi values > 3 occur only in one sample—a shonkinite dike (MP-P0913-10C) that cross-cuts syenite, which also yielded the oldest zircon age (1458  $\pm$  7 Ma; mean  $^{207}$ Pb/ $^{206}$ Pb age), the youngest titanite age (1385  $\pm$  18 Ma), and the most primitive  $\varepsilon Nd_i$ values (weighted mean =  $-4 \pm 0.4$ ). Despite the higher εHf<sub>i</sub> of this sample, excluding it does not affect the mean εHf<sub>i</sub> for all samples (weighted mean εHf<sub>i</sub> without MP-P0913-10C =  $1.72 \pm 0.24$ ). Representative examples of zircon Hf isotopic data are shown in Table 6, and the complete set of zircon Hf isotopic data is provided in Supplementary Data Electronic Appendix 9.

# Monazite textures, U-Th/Pb, trace elements, and Nd isotopes

Monazite in the ultrapotassic rocks primarily occurs in veins and as inclusions in other phases (e.g. titanite, Fig. 5c), and as fine, subhedral to anhedral grains in altered

Downloaded from http://petrology.oxfordjournals.org/ by guest on September 23, 2016

data d
onology
geochr
CP-MS
)-SS
٢
< 1
ntative zircon LA
Representative zircon L⊿
tepresentative zircon LA

Spot	Used in	Used in %	Pb	Th	n A	Th/U			Measured isotopic ratios	isotopic	ratios			App	arent isoto	Apparent isotopic ages (Ma)	a)
	age interp.?	discordance	(mdd)	(mdd)	(mdd)		<sup>207</sup> Pb/ <sup>206</sup> Pb	2σ %	<sup>207</sup> Pb/ <sup>235</sup> U	2σ%	<sup>206</sup> Pb/ <sup>238</sup> U	2σ%	Rho	<sup>207</sup> Pb/ <sup>206</sup> Pb age	2σ abs	<sup>206</sup> Pb/ <sup>238</sup> U age	2σ abs
MP-LO	MP-L0613-BDAY zircon (spot	on (spot size=20	) μm, shot	μm, shot frequency	= 4 Hz,	shot count	nt=80, laser	er energy	= 4 mJ	at 100%)							Î
<b>←</b> c	Yes	1.52	196	306	000	3.45	0.09	1.83	3.045	2.50	0.2457	1.65	0.683	1439	26.3	1417	23.4
7 6	0 Z	3.09 3.09	150	231	19.0	2.40 1.81	0.09248	9/-1	3.046	2.34	0.2463	1.43	0.675	1491 1453	79.7	1421	20.0
2 4	2 2	0.35	127	180	146	1.25	0.09003	79.	3.191	2.27	0.2536	1.39	0.659	1463	23.7 24.4	1458	20.3
ى -	202	0 00 0 00 0 00 0 00 0 00	135	199	132	1.52	0.0926	2.21	3.187	2.76	0.2492	1.60	0.601	1493	33.0	1436	23.0
9	Yes	0.02	144	221	125	1.78	0.08937	1.82	3.07	2.36	0.2474	1.45	0.639	1426	25.9	1426	20.6
7	No	16.46	223	307	171	1.81	0.1075	1.82	3.873	2.27	0.2577	1.30	0.601	1771	32.2	1479	19.2
00	No	1.18	119	185	125	1.48	0.09058	1.66	3.148	2.20	0.249	1.38	0.657	1452	24.1	1434	19.8
6	Yes	1.63	160	248	103	2.43	0.08965	1.75	3.069	2.34	0.244	1.49	0.664	1432	25·1	1409	21.0
10	Yes	2.22	133	202	92	2.14	0.09041	1.67	3.106	2.32	0.2454	1.55	0.694	1448	24.2	1416	22.0
7	No.	3.94	138	215	151	1.44	0.09142	1.76	3.155	2.37	0.2445	1.52	699.0	1469	25.8	1411	21.5
12	Yes	2.43	111	168	122	1.39	0.09094	1.74	3.157	2.32	0.2469	1.48	0.664	1459		1424	21.1
<u></u>	Yes	0.29	195	298	128	2.34	0.08943	1.63	3.106	2.16	0.2468	1:36	0.658	1427	23.3	1423	19:3
1. 4 i	Yes	0.83	102	15/	124	1.27	0.08957	1.67	3.083	2.11	0.245/	1.21	0.611	1430	23.9	1417	17.2
15	0 2	26.25	141	388	, x	2.16	0.1196		4.203	2.40	0.2516	1.46	0.636	1963	36.4	1448	21.2
9 1	0 N	14:91	123	183	182	9 ;	0.1015		3.493	2.45	0.2456		0.656	1665	30.8 80.8	141/	22.0
_ ;	Yes	1.55	103	163	1.16	1.41	0.09039	1.84	3.089	2.32	0.24/2		0.612	1448	26.6	1425	
<u></u>	Yes	2.13	/8/	777	<u></u> 5	75.	0.09027	4 0 4	3.000	2 5	0.2451	2,5	0.620	1445	23.6	14 14	<u> </u>
<u>n</u> e	ON X	4.57	707	<del>1</del> ე	12,	7.80	0.09265	90,	χ. – 4α α – 4α	2	0.24/4	77.	0.627	1494	24.0 20.00	1426	<u> </u>
707	Yes	Ο·/ ·	120	738	<del>4</del> ξ	40.	0.09017	100	3.007	2	0.2480	67.7	0.030	2443 0024	25.0	1432	<u>ö</u> ç
- 6	ze X	60 C	172	760	201	70.7	0.00093	 	7 60 6	47.0	0.2430	500	7000	041	0.4.0	0 1 1 1	3.5
23	\ \ \ \ \ \ \ \ \ \ \ \ \ \ \ \ \ \ \	7.07 0.68	132	200	00 98	9.38	0.09052	77.1	3.085	2.37	0.2447	1.44	0.649	1430	24.0 25.5	14.12	70.7
27	2 2	16.26	- 7 7 7 7 7 7	738	313	2, 2, 2, 2, 2, 2, 2, 2, 2, 2, 2, 2, 2, 2	0.1105	1.96	2000	3.12	0.2666	2.30	0.77	1821	2 2 2	15.5	36.4
25	Yes	0:01	9.5	141	119	1.19	0.0898	1.73	3.09	2.17	0.2491	1.23	0.602	1435	24.9	1435	17.7
26	Yes	0.93	383	269	279	2.05	0.09041	1.58	3.13	2.25	0.249	1.54	0.710	1448	22.9	1434	22.0
27	No	6.65	100	148	100	1.48	0.09361	1.78	3.198	2.49	0.2449	1.69	0.700	1514	27.0	1413	23.9
28	No	24.90	117	152	102	1.51	0.1199	1.90	4.251	2.65	0.2574	1.80	0.697	1968	37.4	1478	26.5
59	No	6.05	209	299	125	2.40	0.0955	1.96	3.364	2.57	0.2535	1.62	0.650	1552	30.4	1458	23.5
30	No.	6.72	117	169	186	0.91	0.09414	1.63	3.215	2.46	0.2466	1.78	0.747	1525	24.9	1422	25.4
31	No S	0.92	54	74	101	0.73	0.09095	1.76	3.159	2.55	0.2512	1.79	0.724	1459	25.7	1446	25.9
35	Yes	. T. C	154	278	72	χ. Ο Ο Γ	0.09067	9/.	3.094	2./3	0.2495	2.02	0.755	1453	26.1	143/	29.0
ک ک	No.	9.45 5.45	777	34 L	671	20.7	0.0973	46.	3.323	2.03	0.2434	7.07	0.728	198/	χΩ.α α α α α	143/	28.0
ง 4 ด	Yes	0.34	160	6/9 6/9	107	2.53	0.00930	0 7	3.030	7 - 7	0.2469	05.1	0.000	1459 CAAL	25.2	1434	9 G
2 0	\ \ \ \ \ \ \ \ \ \ \ \ \ \ \ \ \ \ \	0.50	100	110	- 6	5 5	0.090	1 , 4	0.00	5 6	2162.0		071.0	1442	20.0	1440	20.0
200	Yes	7:47	7/	0110	7,0	- 0 - 0	19060	4 / 1	3.040 0.00 0.00	0.0 20.0	0.2455	1 4.7	0.0	1452	20.0	1410	34.Z
s c	S2- X	00.0	111	9,70	167	9 6	08000	1 2 2	0000	2.20	10270		2000	25,7	7.60	147	20.0
9 6	S ON	00:-	- 1	225	101	9 6	0.00334	2 6	0.00	75.7	0.2403	5 5 7	10.0	1450	25.7	1424	300
33 40	2 2	26.33	165	146	786	0.52	0.1428	1.83	7.7.7	2.53	0.2455	2.25	0.787	2274	41.6	1675	37.6
4 4	\ \ \ \ \ \ \ \ \ \ \ \ \ \ \ \ \ \ \	1.83	318	486	244	9.0	0.09023	2.5	3.027	2.22	0.2458	1.48	0.697	1444	23.0	1418	21.0
42	S C	39.30	176	183	114	1.63	0.1668	1.66	6.118	2.33	0.2697	- t-	0.702	2538	42.2	1541	24.3
43	Yes	0.41	86	152	82	1.85	0.0899	1.87	3.033	3.01	0.2484	2.32	0.784	1437	26.8	1431	33.1
44	Yes	0.64	262	408	147	2.79	0.08925	1.68	2.999	2.80	0.2451	2.19	0.799	1423	23.9	1414	31.0
45	Yes	60.0	142	221	132	1.68	0.0893	1.65	3.014	2.33	0.2473	1.58	0.703	1424	23.5	1426	22.5
																))	(continued)
																3	IIIIII nen)

Downloaded from http://petrology.oxfordjournals.org/ by guest on September 23, 2016

7	5	
S. Continued	commune.	
3		

anies	lable 3. collillued																
Spot	Used in	%	Pb	Т	⊃	Th/U			Measured isotopic ratios	l isotopic	ratios			Appa	arent isoto	Apparent isotopic ages (Ma)	â
	age interp.?	discordance	(mdd)	(mdd)	(mdd)		<sup>207</sup> Pb/ <sup>206</sup> Pb	2σ %	<sup>207</sup> Pb/ <sup>235</sup> U	2σ%	<sup>206</sup> Pb/ <sup>238</sup> U	2σ%	Rho	<sup>207</sup> Pb/ <sup>206</sup> Pb age	2σ abs	<sup>206</sup> Pb/ <sup>238</sup> U age	2σ abs
MP-P0;	714-21 zircon (	MP-P0714-21 zircon (spot size= 25 $\mu$ m, shot frequency	n, shot fre	equency=	4 Hz, sh	ot count=	100, laser	energy=	5 mJ at	100%)							
_	No	70.36	970	4677	710	6.58		1.56	1.169	2.52	0.0812	1.98	0.785	1699	28.8	504	12.0
2	No	38.47	1001	2419	611	3.99	0.09951	1.80	2.3	6.26	0.168	5.99	0.958	1628	33.5	1002	61.5
က	No	14.14	1215	2094	464	4.22	0.09527	1.63	3.015	2.55	0.2286	1.97	0.770	1547	30.7	1328	31.5
4	No	12.88	1188	2002	461	4.28	0.09505	1.66	3.039	2.38	0.2316	1.70	0.716	1543	31.3	1344	29.0
വ	No	82.58	1434	9120	1121	8.14	0.13194	1.57	1.086	2.65	0.0594	2.14	908.0	2137	27.5	372	9.4
9	No	13.30	983	1578	328	4.78	0.09589	1.67	3.097	2.74	0.2331	2.17	0.793	1559	31.4	1352	34.4
7	No	75.21	1094	6160	804	7.69	0.10866	1.60	1.07	2.53	0.0712	1.96	0.773	1790	29.3	444	10.5
∞	No	12.21	1020	1648	341	4.82	0.09473	1.65	3.06	2.73	0.2325	2.18	0.798	1536	31.0	1349	34.4
<u></u>	No	37.99	1094	2363	589	3.99	0.10075	1.60	2.37	6.07	0.172	5.86	0.965	1651	29.8	1024	61.5
10	No	14.65	866	1623	392	4.11	80960.0	1.71	3.024	5.69	0.2297	2.08	0.772	1563	32.1	1334	32.9
1	No	13.40	950	1502	387	3.84	0.09604	1.72	3.095	2.50	0.2333	1.81	0.725	1562	32.3	1353	30.4
12	No	62.38	971	3923	669	5.56	0.10161	1.58	1.432	2.40	0.1021	1.81	0.752	1667	29.3	627	14.1
13	No	12.28	853	1388	412	3.35	0.09473	1.62	3.032	2.59	0.2323	2.02	0.780	1536	30.5	1348	32.6
14	Yes	2.80	225	351	123	2.87	0.09044	1.58	3.034	2.56	0.2439	2.01	0.786	1449	30.2	1408	33.9
15	No	77.36	811	4512	871	5.24	0.11252	1.62	1.043	2.96	0.0672	2.48	0.838	1854	29.3	420	11.8
16	Yes	2.67	146	227	101	2.23	0.09015	1.58	3.013	2.47	0.2431	1.90	0.769	1442	30.2	1404	32.6
17	No	19.44	1340	2440	466	5.21	0.09645	1.62	2.858	2.43	0.2166	1.80	0.743	1570	30.5	1265	28.3
9	No	10.72	1032	1649	329	4.60	0.09444	1.63	3.039	2.58	0.2359	1.99	0.773	1531	30.8	1366	32.7
19	Yes	2.58	110	176	79	2.26	0.08961	1.55	2.959	2.38	0.2412	1.80	0.757	1431	29.7	1394	31.2
20	No	35.89	1076	2499	655	3.89	0.09719	1.69	2.258	3.02	0.1705	2.50	0.829	1584	31.7	1016	28.8
21	No	4.06	463	746	204	3.67	0.09109	1.56	3.029	2.24	0.2429	1.60	0.716	1462	29.7	1403	29.2
22	No	7.44	1129	1942	389	5.04	0.09234	1.56	3.023	2.29	0.238	1.67	0.729	1488	29.7	1377	29.3
23	No	81.08	972	4955	1045	4.78	0.14287	1.65	1.343	3.05	690.0	2.56	0.841	2275	28.5	430	12.4
24	No	40.10	1060	3450	710	4.81	0.09458	1.54	1.98	6.75	0.153	6.57	0.974	1533	29.1	918	61.6
22	No	79.21	955	6305	1008	6.39	0.10259	1.59	0.788	3.20	0.0558	2.78	0.868	1685	29.4	320	10.8
56	No	70.20	1168	5561	799	7.11	0.11327	1.74	1.397	3.26	60.0	2.76	0.846	1866	31.4	226	17.0
27	No	17.43	1437	2753	572	4.93	0.09643	1.56	2.949	2.13	0.2225	1.44	0.677	1570	29.4	1296	25.4
28	No	13.00	1118	1830	466	4.01	0.09543	1.63	3.04	2.60	0.2325	2.02	0.777	1550	30.8	1349	32.6
59	No	15.87	827	1510	322	4.37	0.09549	1.67	2.98	4.69	0.2242	4.38	0.934	1551	31.4	1305	59.8
30	No	8:28	602	926	254	3.84	0.09294	1.62	3.02	2.47	0.2369	1.87	0.754	1500	30.8	1372	31.4
31	No	30.38	933	2053	547	3.83	0.09512	1.58	2.378	2.47	0.1813	1.90	0.768	1544	29.8	1075	24.9
32	No	11.80	1214	2045	491	4.31	0.09467	1.60	3.055	2.39	0.2335	1.77	0.743	1535	30.1	1354	30.0

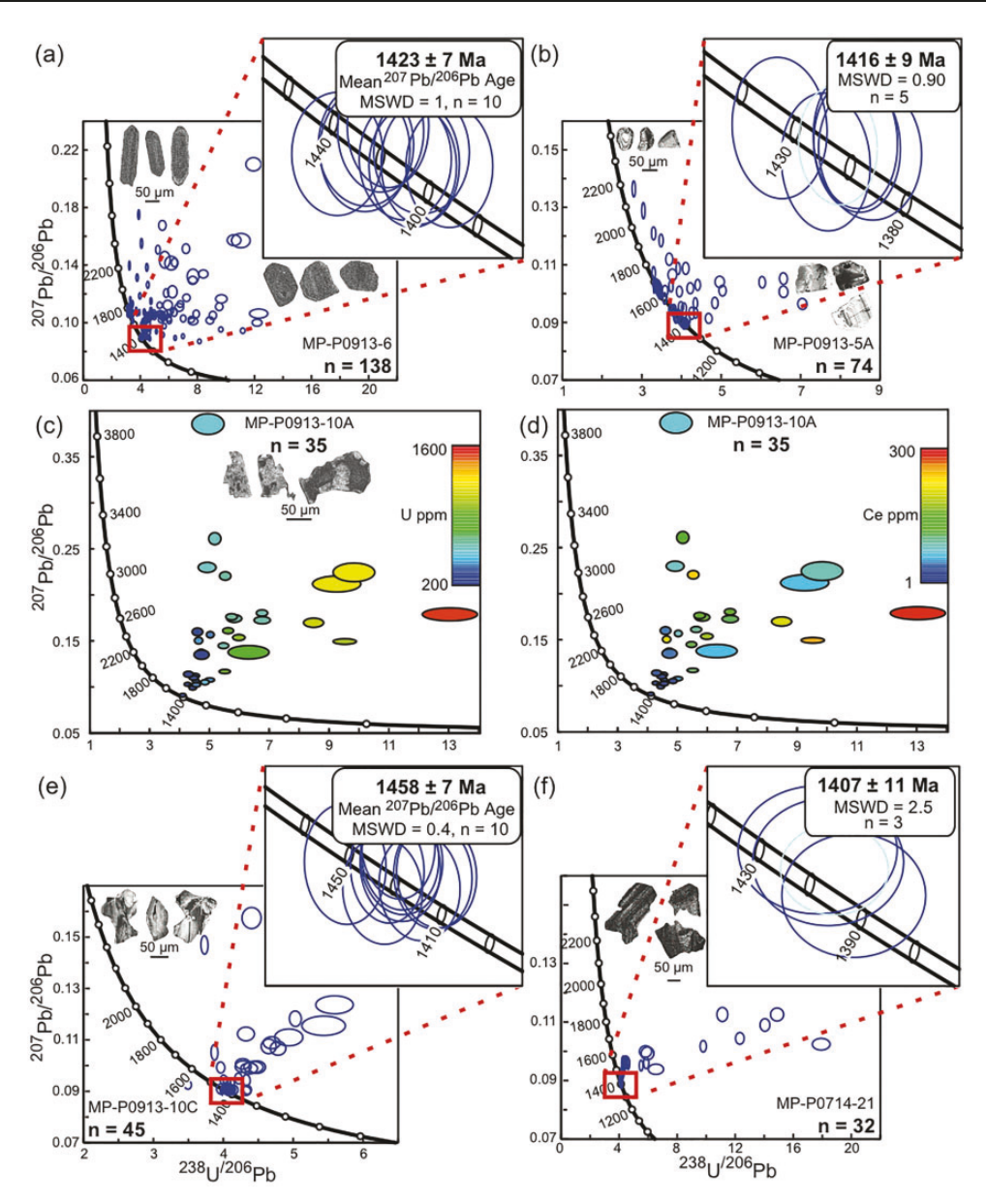


Fig. 10. Representative Tera–Wasserburg concordia plots for U–Pb analyses of zircon in MPIS ultrapotassic rocks. CL images of representative grains are shown in each plot except (d); it should be noted that scale is different for each plot. (a) Sample MP-P0913-6. (b) Sample MP-P0913-5A. (c) Sample with only discordant analyses, colored by U content (MP-P0913-10A). Greater discordance in high-U grains should be noted. (d) Sample with only discordant analyses, colored by Ce content (MP-P0913-10A). Greater discordance in high-Ce grains should be noted. (e) Sample MP-P0913-10C. (f) Sample MP-P0714-21.

samples (Fig. 13a; see description of alteration textures in syenite, above). Euhedral grains were found only in two samples that show abundant evidence for alteration (MP-P0913-2 and MP-P0913-7; Supplementary Data Electronic Appendices 1 and 3). In contrast, monazite is a common accessory mineral in carbonatite, occurring as euhedral to anhedral grains that vary from  $\sim\!\!25$  to 200  $\mu m$  in size in carbonatite sample MP-L0613-BDAY2 (Fig. 13b), and as anhedral, porous, crumbly grains from  $\sim\!\!50\,\mu m$  to  $\sim\!\!1\,mm$  in carbonatite sample MP-P0913-SQ1 (Supplementary Data Electronic Appendix 3).

Representative monazite geochronology data are presented in Table 7 and the complete monazite LASS-ICP-MS dataset (including trace element data) is given

in Supplementary Data Electronic Appendix 10. Monazite from the ultrapotassic rocks and carbonatites typically contains 3-50 ppm U and has low (typically < 5 ppm) radiogenic <sup>206</sup>Pb; thus, U-Pb analyses have large uncertainties and do not yield meaningful dates. However, monazite contains significant Th (typically 2000-20000 ppm) and has low common <sup>208</sup>Pb (i.e. >85% is radiogenic); it is therefore possible to calculate <sup>208</sup>Pb/<sup>232</sup>Th dates. Weighted mean, common-Pb corrected <sup>208</sup>Pb/<sup>232</sup>Th dates for monazite in ultrapotassic samples MP-P0913-2 and MP-P0913-7 are 1376  $\pm$  36 Ma MSWD = 4.5) (n = 13.and  $1401 \pm 32 \,\text{Ma}$  (n=8, MSWD = 1.9), respectively (Fig. 13c). The weighted mean <sup>208</sup>Pb/<sup>232</sup>Th date from carbonatite sample MP-

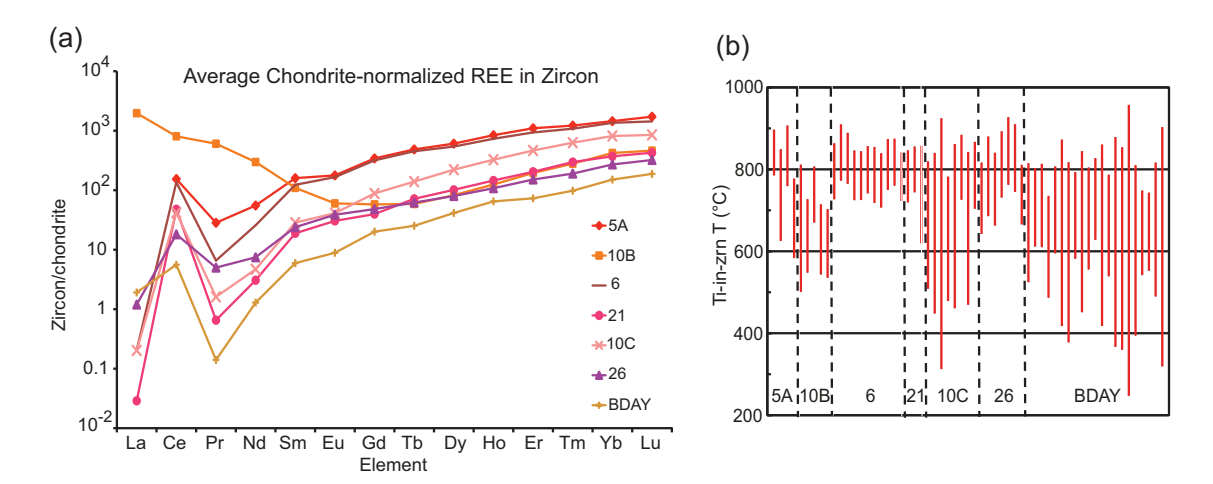


Fig. 11. Selected trace element plots for concordant zircon from MPIS ultrapotassic rocks. (a) Average chondrite-normalized REE patterns for all concordant zircons. (b) Ti-in-zircon apparent temperatures for all concordant zircons. High uncertainties are a product of poor precision as a result of low Ti content in zircon (<10 ppm).

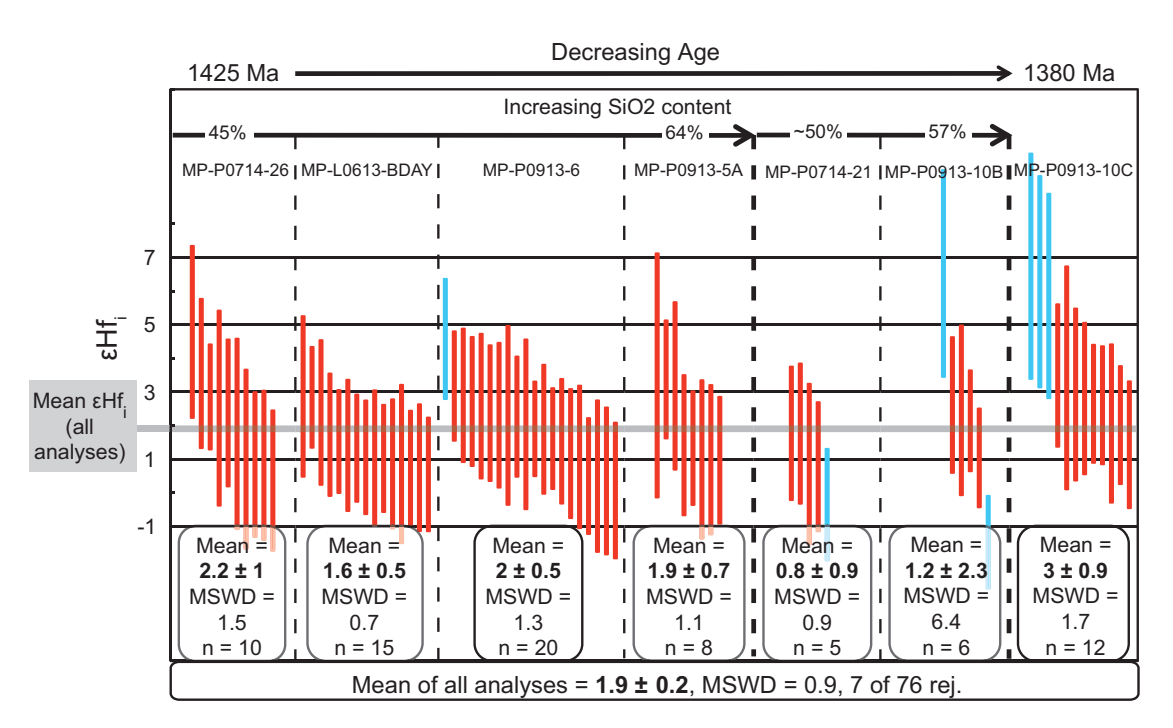


Fig. 12. Weighted mean plot of  $\epsilon$ Hf $_i$  for all measured MPIS zircons. Each set of analyses is from one sample. Analyses are only from zircon that yielded concordant U–Pb analyses. Samples are arranged by age, with age decreasing from left to right. Within each age group, samples increase in whole-rock silica content from left to right. Blue bars represent analyses that were rejected in the weighted mean calculation for all analyses. The mean of all analyses is shown by the gray bar.

L0613-BDAY2 is  $1396 \pm 16 \,\text{Ma}$  (n = 23, MSWD = 4·2), whereas carbonatite sample MP-P0913-SQ1 defines a more narrow range, giving a weighted mean of  $1371 \pm 10 \,\text{Ma}$  (n = 46, MSWD = 1·6) (Fig. 13c). Multiple analyses of single crystals indicate that some monazite grains are zoned with respect to Th, but Th content does not correlate with the common-lead corrected  $^{208}\text{Pb}/^{232}\text{Th}$  dates.

Chondrite-normalized REE patterns in monazite from the ultrapotassic rocks and carbonatites show enrichment in LREE, with steep negative LREE to HREE slopes, and minor negative Eu anomalies (Fig. 13d). Monazite from carbonatite sample MP-P0913-SQ1 shows greater depletion in HREE. Nd isotopic analysis of monazite from carbonatite sample MP-P0913-SQ1 yielded consistent  $\epsilon Nd_i$  values, with a weighted mean of  $-2.8\pm0.2$  (MSWD = 0.8; Fig. 13e). Monazite Nd isotopic data are reported in Table 4.

U–Pb monazite dates from one host-rock sample, a garnet–biotite–sillimanite gneiss (MP-P0913-4), yield a mean  $^{207}$ Pb/ $^{206}$ Pb date of  $1693\pm8\,\text{Ma}$  (MSWD= $2\cdot2$ ; Supplementary Data Electronic Appendix 8).

Downloaded from http://petrology.oxfordjournals.org/ by guest on September 23, 2016

topic data
LA-MC-ICP-MS Hf iso
epresentative zircon
Table 6: R

Spot	Hf beam (V)	βНf	дХв	176Hf/ 177Hf	±2σ	<sup>176</sup> Lu/ <sup>177</sup> Hf	±2σ	<sup>176</sup> Yb/ <sup>177</sup> Hf	Analysis age (Ma)	<sup>176</sup> Hf <sub>i</sub> 177Hf <sub>i</sub>	<sub>i</sub> Hf <sub>i</sub>	$\pm 2\sigma$	Propagated 2σ	Т <sub>БМ</sub>	T <sub>DM</sub> <sup>C</sup> 2-stage
MP-P05	MP-P0913-5A zircon	~													
_	7.3	-1.46	-1.98	0.281927	0.000049	0.000562	0.000007	0.029	1420	0.281912	1.0	1.7	9:1	1835	2088
2	5.2	-1.46	-1.96	0.282021	0.000067	0.001744	0.000072	060.0	1420	0.281974	ဗ	2.4	2.5	1751	1953
က	9.6	-1.49	-1.99	0.281958	0.000059	0.001699	0.000086	0.067	1420	0.281912	<u>-</u>	2.1	2.2	1834	2087
4	8·9	-1.46	-1.98	0.281939	0.000043	0.000631	0.000012	0.034	1420	0.281922	1.4	1.5	1.7	1821	2066
2	8.1	-1.46	-2.01	0.282020	0.000100	0.001380	0.000120	0.061	1420	0.281983	3.6	3.5	3.6	1739	1934
9	6.7	-1.46	-1.99	0.281956	0.000055	0.001173	0.000021	0.057	1420	0.281924	ان خ	2.0	2.1	1818	2060
7	8.9	-1.46	-1.98	0.282003	0.000045	0.000872	0.000023	0.043	1420	0.281980	3.5	1.6	1.7	1743	1941
<sub>∞</sub>	6.5	-1.44	-1.94	0.281928	0.000063	0.000572	0.000028	0.030	1420	0.281913	<u>-</u>	2.2	2.3	1834	2086
MP-P07	MP-P0714-21 zircon														
_	6.1	-1.45	-1.98	0.281888	0.000042	0.000250	0.000011	0.012	1405	0.281881	<del>-</del> 0.4	1.5	1.7	1876	2163
2	5.4	-1.46	-1.95	0.281928	0.000064	0.000477	0.000004	0.023	1405	0.281915	0 8	2.3	2.4	1830	2089
က	5.3	-1.45	-1.98	0.281973	0.000055	0.001211	0.000024	0.059	1405	0.281941	1.7	2.0	2.1	1796	2034
4	6.1	-1.45	-2.02	0.281951	0.000052	0.000375	0.000005	0.019	1405	0.281941	1.7	<del>0</del> .	2.0	1795	2034
2	5.5	-1.45	-1.98	0.281933	0.000050	0.000749	0.000027	0.038	1405	0.281913	0.7	<del>,</del>	1.9	1833	2094
MP-L06	MP-L0613-BDAY zircon	con													
_	4.7	-1.45	-2.03	0.281914	0.000063	0.000143	0.000016	0.007	1425	0.281910	<u>-</u>	2.2	2.3	1837	2088
2	5.9	-1.45	-1.76	0.281904	0.000043	0.000097	0.00000	0.005	1425	0.281901	8. O	1.5	1.7	1849	2107
က	6.1	-1.46	-1.96	0.281930	0.000051	0.000159	0.000002	0.008	1425	0.281926	1.7	<del>,</del>	0; 6:	1816	2055
4	7.2	-1.44	-1.62	0.281969	0.000064	0.000087	0.000002	0.004	1425	0.281967	3.1	2.3	2.4	1761	1966
ഉ	7.2	-1.45	-2.07	0.281970	0.000037	0.000151	0.000005	0.008	1425	0.281966	э <del>.</del>	1.3	1. 5	1762	1967
9	6.1	-1.45	-1.96	0.281917	0.000040	0.000082	0.000002	0.004	1425	0.281915	<u>က</u>	1.4	1.6	1831	2078
7	0.9	-1.45	-1.84	0.281917	0.000053	0.000075	0.00000.0	0.004	1425	0.281915	<u>რ</u>	1.9	2.0	1831	2078
∞	6.2	-1.45	-1.88	0.281927	0.000040	0.000135	0.000002	0.007	1425	0.281923	1.6	1.4	1.6	1819	2060
6	2.7	-1.44	-2.05	0.281910	0.000049	0.000110	0.000002	0.005	1425	0.281907	1.0	1.7	0; 0;	1841	2095
10	2.7	-1.45	-1.93	0.281938	0.000047	0.000125	0.000001	900.0	1425	0.281935	2.0	1.7	1.8	1804	2035
11	8·9	-1.44	-1.96	0.281933	0.000038	0.000150	0.00000	0.008	1425	0.281929	<del>,</del>	1.3	1. 5	1812	2048
12	6.7	-1.45	-1.90	0.281957	0.000057	0.000139	0.00001	0.007	1425	0.281953	5.6	2.0	2.1	1779	1995
13	7.1	-1.45	-1.88	0.281909	0.000043	0.00000	0.00001	0.003	1425	0.281907	1.0	ا ئ	1.7	1841	2095
14	5.5	-1.45	-2.15	0.281914	0.000000	0.000139	0.000002	0.007	1425	0.281910	<del>-</del>	<del>,</del>	0; 0;	1837	2088
15	7.1	-1.45	-1.98	0.281918	0.000043	0.000085	0.000002	0.004	1425	0.281916	1.3	ان ت	1.7	1830	2076

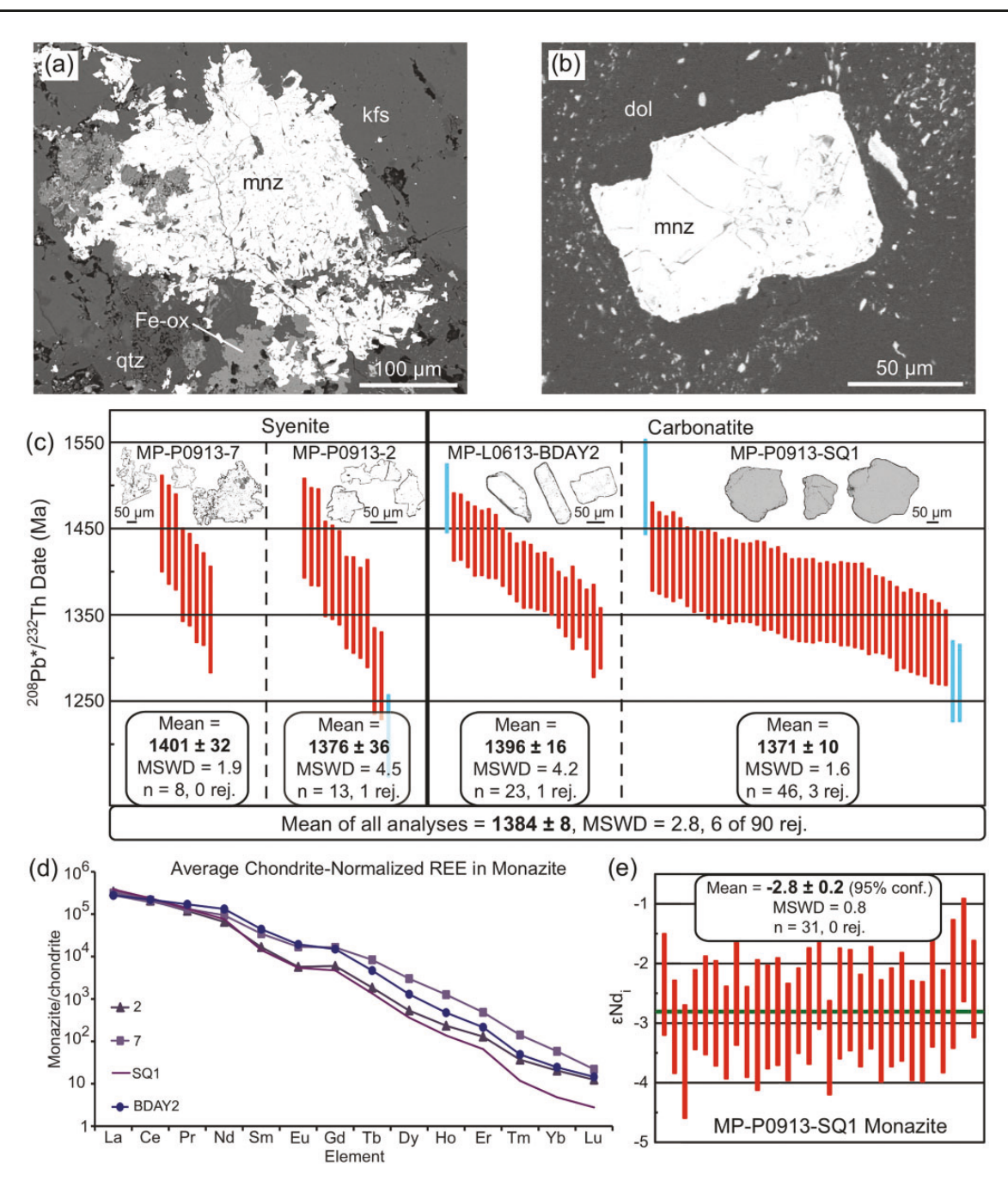


Fig. 13. Examples of monazite grains and monazite data from MPIS rocks. (a) BSE image of anhedral monazite in altered syenite (MP-P0913-7). (b) BSE image of euhedral monazite in carbonatite (MP-L0613-BDAY2). (c) Weighted mean plot of all common-Pb corrected Th-Pb dates from monazite in MPIS rocks. Blue bars represent analyses rejected from the weighted mean calculation. BSE images of representative grains are shown for each sample. It should be noted that scale is different for each sample. (d) Average chondrite-normalized REE patterns for monazite from MPIS ultrapotassic rocks and carbonatite. (e) Weighted mean plot of εNd; for monazite in carbonatite (MP-P0913-SQ1). dol, dolomite; Fe-ox, Fe-oxide; kfs, K-feldspar; mnz, monazite; qtz, quartz.

Chondrite-normalized REE profiles are flat among the LREE, have pronounced negative Eu anomalies, and show a range of HREE contents (10–100 times chondritic values; Supplementary Data Electronic Appendix 8).

## Bastnäsite textures, U-Pb and Nd isotopes

Bastnäsite, the primary REE ore-bearing mineral at Mountain Pass, was observed only in carbonatite

samples. It occurs as tabular or elongate to acicular, subhedral to euhedral, honey-yellow to light brown crystals up to  $\sim\!\!1\,\text{mm}$  in sample MP-P0913-SQ1 (Fig. 14a), and as anhedral intergrowths with barite in samples MP-P0913-1B and MP-L0613-BDAY2 (Fig. 14b). It is occasionally intergrown with synchysite or parisite (Fig. 14c). The grains are compositionally heterogeneous and contain abundant inclusions of calcite, dolomite, and barite.

Downloaded from http://petrology.oxfordjournals.org/ by guest on September 23, 2016

data
logy
ouo.
ochr
Sge
Ρ-Ν
S-IC
LAS
nazite
ทอก
tive
enta
pres
Be
e 7
_
<u>Tap</u>

Spot	⊃	L	Pb	Th/U	% <sup>208</sup> Pb			Measu	red isoto	Measured isotopic ratios					Appare	nt isoto	Apparent isotopic ages (Ma)	(Ma)		
	(mdd)	(mdd)	(mdd)		common	<sup>208</sup> Pb/ <sup>204</sup> Pb	2SE %	<sup>207</sup> Pb/ <sup>206</sup> Pb	2SE %	<sup>206</sup> Pb/ <sup>238</sup> U	2SE %	Rho	<sup>208</sup> Pb/ <sup>232</sup> Th	2SE %	<sup>208</sup> Pb/ <sup>232</sup> Th age	2SE abs.	<sup>208</sup> Pb*/ <sup>232</sup> Th	2SE %	<sup>208</sup> Pb*/ <sup>232</sup> Th age	2SE abs.
NAP PC	NAP_POQ13_CO	-	tons) etizenom	cizo – o	todo mi	from		tarios todo	08-14	acor oner	I m N — Vorage reset 08 —	1000/								Ì
1	5 5 8 8 8	-	262.9	402	12.47	17.71	ا 4 ر	0.8188	1.92	0.54	172	1.000	0.07895	3.10	1536	48	0.06910	3.26	1350	44
- 2	, , ,	2962	282.9	787	10.59	19.5	5.64	0.7726	1.95	0.33	239	1.000	0.07628	3.13	1486	46	0.06820	3.27	1333	44
က	4.1	2678	264.4	299	12.23	18.73	3.68	0.8085	1.88	1.4	85.7	1.000	0.07882	3.11	1533	48	0.06918	3.27	1352	44
4	7.1	4920	460	654	2.51	25.3	11.5	0.599	2.54	0.64	61.0	0.999	0.07458	3.13	1454	45	0.07271	3.28	1419	47
2	დ ფ	4287	414.7	503	8.43	19.98	4.55	0.727	3.04	<del>ا</del> ن	6.97	0.999	0.07722	3.22	1503	48	0.07071	3.38	1381	47
9	11.1	5210	484	465	5.69	21.7	4.61	0.6705	1.94	1.32	23.5	0.997	0.07408	3.13	1444	45	0.06987	3.28	1365	45
7	8.4	3820	383.5	472	8.91	19.18	3.96	0.7392	1.76	0.72	72.2	1.000	0.08007	3.15	1557	49	0.07294	3.31	1423	47
œ	လ ထ	3462	342.5	952	68.6	19.85	4.13	0.7511	2.03	<del>-</del>	155	1.000	0.07892	3.08	1535	47	0.07111	3.24	1389	45
6	7.4	2913	280.8	442	7.46	22	5.45	0.6667	1.98	0.55	81.8	1.000	0.07684	3.13	1496	47	0.07111	3.28	1388	46
10	3.4	2395	242.8	822	10.16	17.84	5.33	0.7772	1.97	0.16	475	1.000	0.08083	3.10	1571	49	0.07262	3.25	1417	46
1	4.1	4624	443.2	1087	8.46	21.85	2.88	0.6812	1.73	2.1	71.4	1.000	0.07640	3.11	1488	46	0.06993	3.27	1366	45
12	3.5	3155	309.9	606	12.10	17.86	3.53	0.8062	1.96	_	100	1.000	0.07833	3.10	1524	47	0.06885	3.26	1346	44
13	6.4	2726	254.4	446	9.70	26.5	5.28	0.5913	2.29	5.9	65.5	0.999	0.07435	3.13	1450	45	0.06714	3.28	1314	43
14	7	2556	267.2	417	13.40	19.58	4.03	0.7444	1.86	2.4	83.3	1.000	0.08324	3.07	1616	20	0.07209	3.23	1407	45
15	3.4	3468	329	1031	4.98	21.4	6.07	0.6843	2.07	1.2	150	1.000	0.07556	3.11	1472	46	0.07180	3.26	1401	46
16	3,0	4280	411	1370	6.67	18.17	4.57	0.7697	1.85	-0.25	252	1.000	0.07642	3.12	1488	46	0.07132	3.27	1392	46
17	4.7	3020	299.7	641	9.27	20	4.20	0.683	2.46	0.2	200	1.000	0.07895	3.52	1536	24	0.07164	3.66	1398	21
18	2.3	2565	255.8	1176	11.32	16.8	4.40	0.8047	1.85	-0.46	185	1.000	0.07931	3.37	1543	25	0.07033	3.52	1374	48
19	7.5	2964	289.3	410	9.85	19.42	3.60	0.7396	1.92	0.65	86.2	1.000	0.07763	3.39	1511	21	0.07001	3.53	1368	48
20	16	2805	285.4	182	9.44	22.41	3.93	0.6615	2.00	0.785	12.6	0.988	0.08096	3.43	1574	24	0.07332	3.57	1430	51
21	4.6	2378	245.3	288	12.91	19.38	3.51	0.7612	1.90	0.5	460	1.000	0.08204	3.54	1594	26	0.07144	3.68	1395	51
22	1	2789	268.3	262	7.30	24.5	5.31	0.6041	2.01	0.71	64.8	1.000	0.07648	3.52	1490	23	0.07090	3.68	1384	21
23	<u>ن</u>	2761	262.7	476	6.03	18:3	7.10	0.713	2.19	90.0-	1217	1.000	0.07566	3.34	1474	49	0.07110	3.48	1388	48
24	တ္ (	3330	318.5	431	8.14	22	5.45	0.636	2.33	0.31	181	1.000	0.07590	3.40	1479	20	0.06972	3.54	1362	8 9
25	0 00 10	2472	233.9	269	7.16	20.8	6.73	0.6725	1.96	0.61	90.2	1.000	0.07506	3.48	1463	2	0.06968	3.62	1362	49
70	· 0	1/07	200.9	324	0.0	9 C	4.73 5.73	0.7408	2.00	20.00	7.4.	000.	0.07298	رن 4 د د د د د د د د د د د د د د د د د د د	1480	- c	0.00831	ς. 10.00	1330	δ δ
78	0.0	2300	261.0	270	0.03	10.68	0.0	0.7128	7 . 7	0.00	52.1	000	0.07670	5.45 5.45 5.45	1423	4 С	0.000.0	) () () ()	1380	9 G
26	10.3	3003	268	319	8.01	19.3	5.70	0.7442	1.94	0.08	1188	1.000	0.07066	3.33	1380	46	0.06500	3.48	1273	8 4 4 4
30	5.1	3530	328.9	752	5.31	22.3	6.28	0.694	2.33	0.27	226	1.000	0.07385	3.23	1440	47	0.06993	3.38	1366	46
31	15.6	3850	365	274	6.75	24.6	4.47	0.62	2.24	0.97	20.7	0.994	0.07510	3.34	1464	49	0.07003	3.49	1368	48
32	<u>∞</u>	3214	301.9	397	6.78	19.9	5.53	0.716	2.19	0.19	321	1.000	0.07439	3.49	1450	21	0.06935	3.63	1355	49
33	4 i	3523	335.1	833	6.92	19:5	5.64	0.7666	1.94	0.33	28	1.000	0.07532	3.23	1468	47	0.07011	8 8 8 8	1370	46
გე ი	τ 4 τ	3098	294.7	629	10.29	- x x x	4.75	0.77	7 .7	۰ ر د د	25.	000-	0.0/524	λ 24 24 24 34 34 34 34 34 34 34 34 34 34 34 34 34	1400	2 2	0.06/50	30.5	1320	δ.
ი ი		2002	2004	1515	) v	2 - Z	4.00 0.00	0.7104	S R	- c	4.00	1 000	0.07500	5.45 000	1450	4 У С	0.0000	00.00	1220	4 4
37.	4.4	3560	333.4	719	5.95	19.73	4.97	0.744	2.06	2 6	250	1.000	0.07420	2 2 2	1447	84	0.06979	3.48	1364	47
88	. 60	3477	327.7	208	9.63	18.77	4.79	0.782	2.05	1.12	72.3	1.000	0.07457	3.42	1454	20	0.06739	3.56	1318	47
39	25.5	5670	574	198	2.84	35.9	8.36	0.434	2.78	0.423	11.19	0.970	0.07923	3.50	1541	54	0.07698	3.64	1499	22
40	8.1	3356	322	372	6.73	20.6	4.85	0.721	2.18	0.5	220	1.000	0.07511	3.34	1464	49	0.07005	3.48	1369	48
41	က	3414	339.3	1053	8.43	19.53	3.84	0.7509	1.97	<del>-</del>	136	1.000	0.07778	3.24	1514	49	0.07122	3.39	1391	47
42	2.7	4053	402.5	1299	10.10	19.74	3.50	0.7739	1.79	2.5	59.1	1.000	0.07767	3.38	1512	51	0.06982	3.53	1364	48
43	က	3461	356.9	1190	10.93	17.77	4.22	0.8131	1.85	۳.0-	833	1.000	0.08069	3.29	1568	52	0.07187	3.44	1403	4 8
4 4 4 r	ω <u>-</u>	2955	270.4	312	9.06	23.1	5.63	0.6728	86 5	<del>ر</del> ن	100	1.000	0.07158	3.51	1397	4 1 1	0.06510	 	1275	7 4 7
<del>.</del> გ	- 4	3534	245.0	937	10.4	25.4	4.03 0.03	0.0800	00 C	- 272	7	1,000	0.08115	0.4.50 0.00	1/87	22	0.0710	50.5 50.5 50.5	1201	- 0
5		2005	0	200	5	t.07	0.0	2020	200.7	74.0	2	000.	0000	0.0	1404	8	0.0.0	† 0	- 00	5
																			(continued)	(panı

Table 7: Continued

Downloaded from http://petrology.oxfordjournals.org/ by guest on September 23, 2016

Spot	Spot U Th	T L	Pb	Th/U	% <sup>208</sup> Pb			Measur	ed isotol	Measured isotopic ratios					Apparer	nt isotc	Apparent isotopic ages (Ma)	Ma)		
	(mdd)	(mdd) (mdd)	(mdd)		common	<sup>208</sup> Pb/ <sup>204</sup> Pb	2SE %	<sup>207</sup> Pb/ <sup>206</sup> Pb	2SE %	<sup>206</sup> Pb/ <sup>238</sup> U	2SE %	Rho	<sup>208</sup> Pb/ <sup>232</sup> Th	2SE %	<sup>208</sup> Pb/ <sup>232</sup> Th age	2SE abs.	<sup>208</sup> Pb*/ <sup>232</sup> Th	2SE %	<sup>208</sup> Pb*/ <sup>232</sup> Th age	2SE abs.
MP-T	0613-BD,	MP-L0613-BDAY2 monazite (spot size	nazite (sp	oot size=	= 9 µm, sh	9 $\mu$ m, shot frequency=	S	Hz, shot count=		80, laser energy = 4 mJ at $100\%$	ergy= 4 m	J at 100	1%)							
_	2.7	7570	758	3030	0.57	13		0.457		-0.14	143	1.000	0.07129		1392	29	0.07089	2.34	1384	32
2	3.2		069	2174	1.19	11.3	17.7	0.586	2.54	0.14	78.6		0.07205		1406	30	0.07119	2.34	1390	32
က	10.1		803	781	1.13	18	2.99	0.604	_	80.0	238		0.07352		1434	31	0.07269	2.35	1418	33
4	6.5		1670	2364	0.54	18.5	28.6	0.3733		0.51	106		0.07215		1408	31	0.07176	2.40	1401	34
വ	7.7	17210	1717	2128	0.85	13.3	12.8	0.533	2.55	0.37	40.6	0.998	0.07023	2.29	1372	31	0.06964	2.50	1361	34
9	12:3		2448	1880	0.51	27	37	0.392		0.36	38.9		0.07154		1397	31	0.07118	2.44	1390	34
7	<del>ر</del> 9		1263	6536	0.31	14.8	18.2	0.444		0.05	520		0.07029		1373	30	0.07008	2.37	1369	32
œ	7.5		1516	2198	0.57	14.5	8.97	0.616	2.21	0.54	61.1		0.06994		1366	30	0.06954	2.44	1359	33
6	5.2		227	420	2.70	14.7	15	0.64		0.35	9.88		0.07661		1492	36	0.07453	2.60	1453	38
10	4.9		370	719	1.52	16.3	17.2	0.598		0.14	393		0.07749		1508	37	0.07631	5.66	1486	40
11	3.1		939	3333	0.20	9.5	65.3	0.361	4.42	0.04	275		0.07383		1440	38	0.07368	2.79	1437	40
12	5.7		1830	3448	0.39	22.4	38.4	0.467		0.24	313		0.06844		1338	25	0.06817	4.01	1333	24
13	5.6		1305	2252	0.45	19.7	15.2	0.515		0.34	221		0.07441		1451	32	0.07407	2.61	1444	38
14	4:3		1136	2500	0.39	18.8	17.6	0.4625		-0.14	429		0.07382		1440	37	0.07353	2.78	1434	40
15	26.2		888	322	1.54	11.95	5.69	0.694		0.19	8.48		0.07342		1432	33	0.07229	2.49	1411	32
16	00		815	1087	1.02	13.4	18.7	0.582		0.26	20		0.07409		1445	34	0.07334	2.57	1431	37
17	23.6		1012	448	1.05	14.5	15.9	989.0		0.203	13.3		0.07033		1374	46	0.06959	3.51	1360	48
18	37.2		1538	441	69.0	15.2	11.2	0.587		0.135	13.4		0.06820		1333	33	0.06773	5.64	1325	32
19	10		2006	1949	0.22	22	72.7	0.381		0.29	29.7		0.07176		1401	36	0.07160	2.74	1398	38
20	52.6		1526	309	1.29	13.22	4.99	0.678		0.158	8.29		0.06978		1363	32	0.06888	2.56	1346	32
21	12.7		466	373	1.32	23.6	6.36	0.3244		0.393	13.8		0.07455		1453	32	0.07357	2.61	1435	37
22	27.9		573.4	195	0.35	20	240	0.3513		0.1176	8.06		0.07177		1401	34	0.07152	2.61	1396	36
23	105		288	31	5.05	17.04	3.93	0.5643		0.1233	5.29		0.05588		1099	34	0.05306	3.27	1045	34
24	234		191.1	11	8.09	16.43	3.65	0.602		0.089	16.9		0.05048		962	99	0.04640	6.72	917	62
22	215		320	20	1.99	25.1	14.7	0.4443		0.0329	8.14		0.05433		1069	40	0.05325	3.90	1049	41
56	11		398.9	327	1.15	32	37.5	0.4651		0.57	6.73		0.07541		1470	37	0.07455	2.69	1453	39

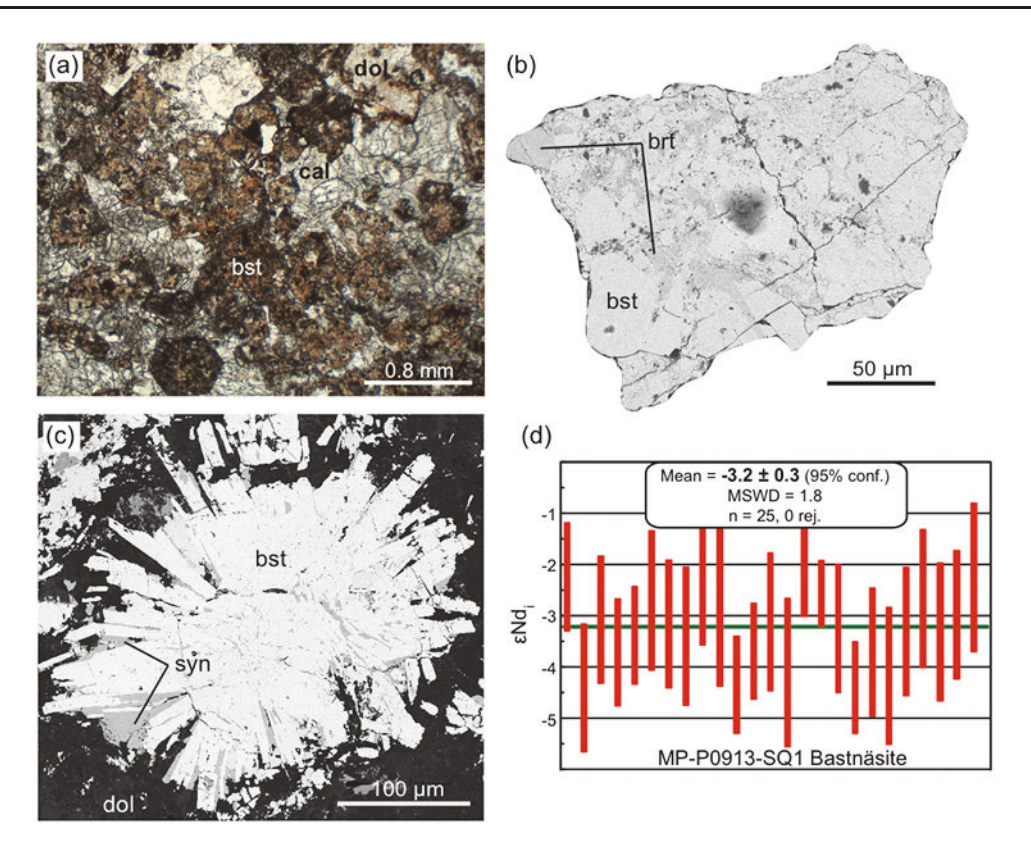


Fig. 14. Examples of bastnäsite in MPIS carbonatite. (a) Plane-polarized light photomicrograph of bastnäsite in a matrix of calcite and minor dolomite in carbonatite thin section (MP-P0913-SQ1). (b) BSE image of bastnäsite–barite intergrowth in grain mount (carbonatite sample MP-P0913-1B). (c) BSE image of intergrowth between bastnäsite and synchysite–parisite in carbonatite thin section. (d) Weighted mean plot of εNd<sub>i</sub> for bastnäsite in carbonatite (MP-P0913-SQ1). brt, barite; bst, bastnäsite; cal, calcite; dol, dolomite; syn, synchysite/parisite.

Bastnäsite from two carbonatite samples was analyzed for U-Pb and Nd isotopes. Both samples are very low in U (<10 ppm), and have high and variable common Pb contents. The low U combined with the large scatter in Pb and U/Pb isotopic ratios suggest that bastnäsite has behaved as an open system with respect to Pb; thus reliable dates could not be calculated and bastnäsite U-Pb data are not considered further. The opensystem behavior described here for bastnäsite was also reported by DeWitt et al. (1987, 2000). In contrast, Nd isotopic analysis of bastnäsite from sample MP-P0913-SQ1 yielded relatively consistent ENd; values with a weighted mean  $\varepsilon Nd_i$  of  $-3.2 \pm 0.3$  (MSWD = 1.8), consistent with ENd; from monazite in the same sample (Figs 13e and 14d). A date of 1380 Ma was used for bastnäsite εNd; age correction, based on the sample's mean monazite Th-Pb date of  $1371 \pm 10 \, \text{Ma}$  (see above). Bastnäsite Nd isotopic data are reported in Supplementary Data Electronic Appendix 6.

#### **DISCUSSION**

# Trace element sinks in an ultrapotassic silicatecarbonatite suite

Trends observed between whole-rock major element oxides in Mountain Pass shonkinite and syenite may be

attributed to differences in the modal abundance of major and accessory phases. The trends observed between major elements and silica in MPIS rocks, such as increasing Al<sub>2</sub>O<sub>3</sub> with increasing silica and lack of trend between K<sub>2</sub>O and silica, are common in other ultrapotassic suites (Foley et al., 1987; Castor, 2008). Decreasing Mg and Ca contents with increasing silica content are controlled by the greater modal abundance of clinopyroxene (Mg, Ca) and apatite (Ca) in low-silica samples. Decreasing Fe content with increasing silica is probably a product of decreased abundance of clinopyroxene and biotite. Lower P2O5 is probably due to decreased abundance of apatite in more felsic samples. TiO<sub>2</sub> also decreases with increasing silica, probably owing to the high abundance of Ti-bearing biotite in mafic samples, which has been reported in previous studies (Haxel, 2005; Castor, 2008). Higher Ti in mafic samples may also be due in part to the presence of clinopyroxene (Haxel, 2007). Increased levels of Al and Na in high-silica samples are probably due to greater abundances of K-feldspar and plagioclase, the latter of which is mostly absent in mafic samples. Potassium does not show a marked trend, presumably because of the high abundance of biotite in mafic samples and Kfeldspar in felsic samples.

The higher abundance of compatible trace elements (i.e. Cr, V) in mafic samples is characteristic of most

igneous suites, and is probably controlled primarily by clinopyroxene and biotite. The high abundance of incompatible trace elements in mafic MPIS samples (i.e. Ba, Sr, and LREE) is atypical of most igneous suites, but is common in ultrapotassic suites (Foley et al., 1987; Castor, 2008) and reflects high modal percentages of incompatible element-rich phases in the mafic samples. Apatite analyzed in this study typically has Sr contents in the tens of thousands of ppm range (Supplementary Data Electronic Appendix 11), and is probably the predominant sink for Sr in the less evolved rocks, as it is most abundant in these samples. High Ba content is probably due to high-Ba biotite, which was noted by Haxel (2005) and Castor (2008). The absence of plagioclase in mafic MPIS rocks indicates that it is unlikely to account for high Sr and Ba in mafic samples, and is therefore not an important host to these elements.

Chondrite-normalized REE patterns of the whole-rock samples analyzed in this study are typical of ultra-potassic rocks, most notably the high LREE to HREE slope and lack of an Eu anomaly (e.g. Foley *et al.*, 1987; Castor, 2008), the latter indicating that plagioclase fractionation was not a significant factor in the magmatic history of the MPIS—consistent with the paucity of plagioclase in these rocks.

The higher abundance of LREE in low-silica samples is most probably due to the abundance of apatite. Apatite has been noted as an important REE host in alkaline rocks (e.g. Zhou & Wang, 1989; Krenn et al., 2012), and forms up to  $\sim$ 3% of the mafic MPIS samples in this study. Previous studies have reported up to 5% apatite in mafic MPIS samples (Woyski, 1980; Haxel, 2005). For MPIS samples in which apatite was analyzed, its modal abundance accounts for  $\sim$ 30-40% and  $\sim$ 40-70% of the whole-rock Ce content for felsic and mafic samples, respectively (Supplementary Data Electronic Appendix 12). Titanite is also an important REE host—it is known to incorporate up to ~4 wt % REE in alkaline igneous rocks (e.g. Vuorinen & Hålenius, 2005), and is commonly considered an important REE sink in silicate magmas (e.g. Gromet & Silver, 1983; Sawka et al., 1984). Although the modal abundance of titanite is poorly constrained in most samples, for samples in which its approximate modal abundance is known, the modal abundance of titanite accounts for ~5-20% of whole-rock Ce (Supplementary Data Electronic Appendix 12). Titanite in apatite-poor samples contains higher LREE—for example, titanite accounts for up to ~90% of whole-rock Ce in one apatite-poor leucosyenite sample (MP-P0714-17). However, titanite modal abundance is similar in both mafic and felsic samples, and therefore the observed trends in REE cannot be explained by differences in its relative abundance between rock types. Monazite is present in some felsic MPIS samples, and must account for some of the whole-rock LREE in these samples. Sodic amphibole may also contain a significant amount of the whole-rock LREE (e.g. Bea, 1996); however, amphibole composition was not determined.

The HREE, Th, and U contents of the samples do not show a trend with major element composition. Metamict, high-Th, high-U, and HREE-rich zircon (e.g. Fig. 9a and b, Supplementary Data Electronic Appendix 7) is ubiquitous in MPIS rocks of all compositions. Zircon has been shown to be a significant host to HREE in granitoids (Bea, 1996) and actinides in alkaline rocks (e.g. Žáček et al., 2009), suggesting that zircon may be an important host to HREE, Th, and U in the MPIS. Concordant zircon grains utilized for geochronology data are less abundant and contain much lower Th, U, and HREE than metamict grains (e.g. Table 5), and are thus not considered. An approximate modal abundance of  $\sim$ 0·125–0·25% metamict zircon accounts for  $\sim$ 30– 70% of whole-rock Yb content in felsic samples (Supplementary Data Electronic Appendix 12). In mafic samples, however, zircon only contains  $\sim$ 5–15% of the whole-rock Yb. Apatite and titanite each account for  $\sim$ 8–20% of the whole-rock Yb in all samples, regardless of composition. Sodic amphibole may account for the bulk of the remaining HREE—it is common in mafic to intermediate MPIS rocks, and is known to contain appreciable HREE (e.g. Bea, 1996). Approximately 5-30% of whole-rock Th can be attributed to zircon, whereas apatite accounts for  $\sim$ 4–10% (but as much as 20%) and titanite for <1-3% (Supplementary Data Electronic Appendix 12). Thorite was also observed in some samples, and probably contains the bulk of whole-rock Th less than 0.02% modal thorite would be required to account for the whole-rock Th in most samples. For two samples with the highest whole-rock Th content (MP-P0913-5A and MP-P0714-17),  $\sim$ 0.03% and 0.05% modal thorite would be required, respectively. Where present, monazite also accounts for some of the whole-rock Th, but occurs primarily in felsic samples and is not present in significant abundance. Most of the whole-rock U (65-90% or more) can be attributed to zircon, whereas apaand titanite each tite account for (Supplementary Data Electronic Appendix 12).

Together, these data indicate that apatite is probably the most important host of LREE in these rocks, followed by titanite. Apatite, titanite, and zircon are probably important HREE hosts, but amphibole may also host significant amounts of HREE in mafic samples. Thorite and zircon are the most important hosts to Th and U, respectively. Monazite contains abundant REE and Th, but is not present in significant amounts in most samples and appears to occur only as a secondary phase. The presence of monazite in veins may indicate that monazite grew from a late-stage fluid, as suggested by Stoeser (2013)—in this case, monazite may be an additional primary REE host in some samples. Alternatively, the presence of monazite and rutile in rocks with titanite that appears to be breaking down (Fig. 5c), and the lack of titanite in rocks that contain significant monazite and rutile (e.g. MP-P0913-2), may indicate that the latter two phases grew at the expense of titanite, and thus host REE, Th, and HFSE that were formerly hosted by titanite.

Based on these data, apatite, titanite, zircon, thorite, and sodic amphibole are likely to have played the most important roles in controlling the REE, HFSE, and actinide budget of the ultrapotassic magmas as they crystallized.

## **Geochronology of the MPIS**

## Ultrapotassic silicate rocks

With the exception of two samples that have undergone minor disturbance of the U–Pb system and therefore record two discrete age populations (samples MP-P0714-16 and MP-P0714-26), titanite in the ultrapotassic rocks of the MPIS consistently yields single-population U–Pb dates that range from  $1429 \pm 10$  to  $1385 \pm 18$  Ma (Fig. 6). In contrast, zircon yields complex and chiefly discordant U–Pb data (Fig. 10), providing minimal age information for most samples. Based on textural observations, monazite in the ultrapotassic rocks appears to be secondary, and yields scattered and imprecise Th–Pb and U–Pb dates (Fig. 13).

Several lines of evidence indicate that titanite is most probably a primary phase and that the titanite dates are best interpreted as the igneous crystallization ages of the ultrapotassic rock samples: (1) detailed petrographic observation indicates that titanite is generally euhedral to subhedral and shows interlocking textures with primary igneous mineral assemblages (Fig. 5a and b), suggesting that it crystallized directly from a melt; (2) where present, titanite alteration textures suggest that it is primary and has partially reacted to form secondary minerals (Fig. 5c), rather than grown in response to alteration; (3) chondrite-normalized REE patterns in Mountain Pass titanite are similar to chondritenormalized REE patterns from Mountain Pass ultrapotassic rocks in terms of LREE enrichment and lack of an Eu anomaly (Figs 4 and 7a), suggesting that both crystallized from the same melt; (4) Zr-in-titanite thermometry predominantly yields temperatures of 700°C and higher, consistent with an igneous origin (Fig. 7b); (5) dates obtained from oscillatory-zoned, concordant zircon overlap the titanite dates within uncertainty in four of five samples. Taken together, and as stated above, these data suggest that titanite is most probably a primary igneous phase in the Mountain Pass ultrapotassic rocks, and has recorded the same igneous crystallization event that is sparsely recorded by zircon. We attribute titanite U-Pb age sub-populations in MP-P0714-16 and MP-P0714-26 to subtle loss of radiogenic Pb, and the ages of the samples are interpreted to be represented by their older age components (Fig. 6). The variability in apparent Zr-in-titanite temperatures in all but the youngest samples (MP-P0913-10C and MP-P0714-17) suggests that some titanite grains may have recorded lower apparent Zr-in-titanite temperatures in response to thermal disturbance during emplacement of later phases of magma, which may provide an explanation for the subtle loss of radiogenic Pb in MP-P0714-16 and MP-P0714-26.

Despite their scarcity, concordant zircon dates are present in six samples, ranging from 1458  $\pm\,7$  to

1407 ± 11 Ma, and, based on crystal morphology and oscillatory zonation, are regarded as reflecting igneous crystallization ages in five of these samples. Concordant dates from ~1635 to 1800 Ma are derived from multiple, discrete grains in MP-P0913-5A and MP-P0913-6; these are interpreted as xenocrystic zircon inherited from the host-rocks based on their similarity to zircon from the host-rock in terms of age, morphology, and Th/U < 1 (see description of zircon above). MP-P0913-5A also yielded zircon dates from 1600 to 1430 Ma from three large, rounded grains that do not overlap with either host-rock zircon dates, or zircon dates from other MPIS rocks (Fig. 10b, Supplementary Data Electronic Appendix 8). These are interpreted as 'mixed' dates resulting from sampling of both Mesoproterozoic overgrowths and inherited, Paleoproterozoic cores of grains. Additionally, these zircon grains have Th/U ratios < 1 (Supplementary Data Electronic Appendix 8), the same as for zircon older than 1640 Ma in the sample and zircon from the hostrocks. In contrast, all zircon grains younger than 1430 Ma in this sample (as well as most zircon grains from all other MPIS samples except MP-P0913-10B) Th/U > 1 (Supplementary Data Electronic Appendix 8); therefore, zircon grains with Th/U < 1 are excluded from the age interpretation of MP-P0913-5A.

MP-P0913-10C is the only sample in which zircon yields only Mesoproterozoic dates, but titanite and zircon dates do not coincide (Figs 6 and 10e). This rock crosscuts another rock (MP-P0913-10B) that yields younger overlapping dates from titanite and oscillatoryzoned zircon (e.g. Figs 2c and 6, Supplementary Data Electronic Appendix 8). We therefore infer that the U-Pb zircon age does not reflect the crystallization age of this rock; instead, we prefer the interpretation that these zircon grains are inherited, and a result of recycling of older zircon within the MPIS.

### Carbonatite

The Th–Pb monazite crystallization ages of carbonatite samples MP-L0613-BDAY2 and MP-P0913-SQ1 are inferred to be  $\sim\!1405\!-\!1395\,\text{Ma}$  and  $\sim\!1380\!-\!1370\,\text{Ma}$ , respectively. We attribute the excess scatter (MSWD =  $4\cdot2$  and  $1\cdot6$ , respectively) observed in the samples to be a result of variable but minor radiogenic Pb loss, which probably skews their mean dates toward younger ages. Regardless, monazite Th–Pb dates from carbonatite overlap titanite and zircon U–Pb dates < 1415 Ma from the ultrapotassic rocks within uncertainty—indicating that carbonatite magmatism and the latter stages of ultrapotassic magmatism at Mountain Pass were broadly coeval.

# Timescales of ultrapotassic silicate-carbonatite magmatism at Mountain Pass

U-Pb zircon dates from ultrapotassic rocks in the Birthday and Corral stocks (Fig. 1b) constrain ultrapotassic magmatism in these locations to  $\sim\!1430\text{--}1420\,\text{Ma}$ 

(Fig. 15). Although less precise, titanite dates corroborate these ages. Zircon and titanite dates from ultrapotassic rocks in the Tors, Mexican Well, and Wheaton stocks indicate a second stage of magmatism c. 1410-1400 Ma (Figs 1b and 15). The mean Th-Pb date of 1396 ± 16 Ma from monazite in carbonatite dike sample MP-L0613-BDAY2 suggests that this stage was accompanied by emplacement of carbonatite dikes (Figs 2d and 15). We interpret titanite dates of 1385  $\pm$  18 Ma and 1358 ± 71 Ma from shonkinite and svenite dikes (MP-P0913-10C and MP-P0714-17), respectively, to record the latest stage of ultrapotassic magmatism at c. 1380-1370 Ma, on the following basis: (1) the dikes cross-cut 1410-1400 Ma syenite; (2) the dikes are continuous and do not appear to be deformed, suggesting that they were not comagmatic with the rock they cross-cut (Fig. 2c); (3) previous work suggests that a shonkinite vein cross-cuts carbonatite (Olson & Pray, 1954), indicating relatively late emplacement of shonkinite dikes and veins. The mean monazite Th-Pb date of carbonatite sample MP-P0913-SQ1 indicates that this stage was accompanied by emplacement of the Sulphide Queen stock (Figs 1b and 15).

The geochronology results reveal that ultrapotassic silicate–carbonatite magmatism at Mountain Pass occurred episodically over  $\sim$ 45–50 Myr, a relatively long period of time considering the small volume of

these rocks that is now exposed. However, alkaline and carbonatite magmatism in other locations around the world is commonly long-lived within a restricted area (Jones et al., 2013). For example, alkaline igneous rocks in the Southern Granulite Terrain of India (Santosh et al., 2014), the Paraná-Etendeka large igneous province in Paraguay (Gibson et al., 2006), and the Monteregian Hills of Quebec, Canada (Eby, 1984) were all shown to have been emplaced in two distinct episodes ~20 Myr apart. Additionally, alkaline igneous rocks in the Chilwa Alkaline Province of Malawi were emplaced in three phases ~10 Myr apart (Eby et al., 1995). The ~45 Myr age range of MPIS rocks is longer than these other occurrences, but regardless, the temporal range of ultrapotassic and carbonatitic magmatism at Mountain Pass is consistent with temporal relationships observed in other alkaline rock occurrences, and indicates repeated partial melting of the source(s) of the MPIS during the Mesoproterozoic.

# Petrogenetic processes recorded by mineralscale Nd and Hf isotopes

Titanite  $\varepsilon Nd_i$  values from the ultrapotassic rocks at Mountain Pass predominantly range between -3.5 and -6, with the highest values in all but one sample overlapping the  $\varepsilon Nd_i$  (-2.5 to -3.5) values obtained from

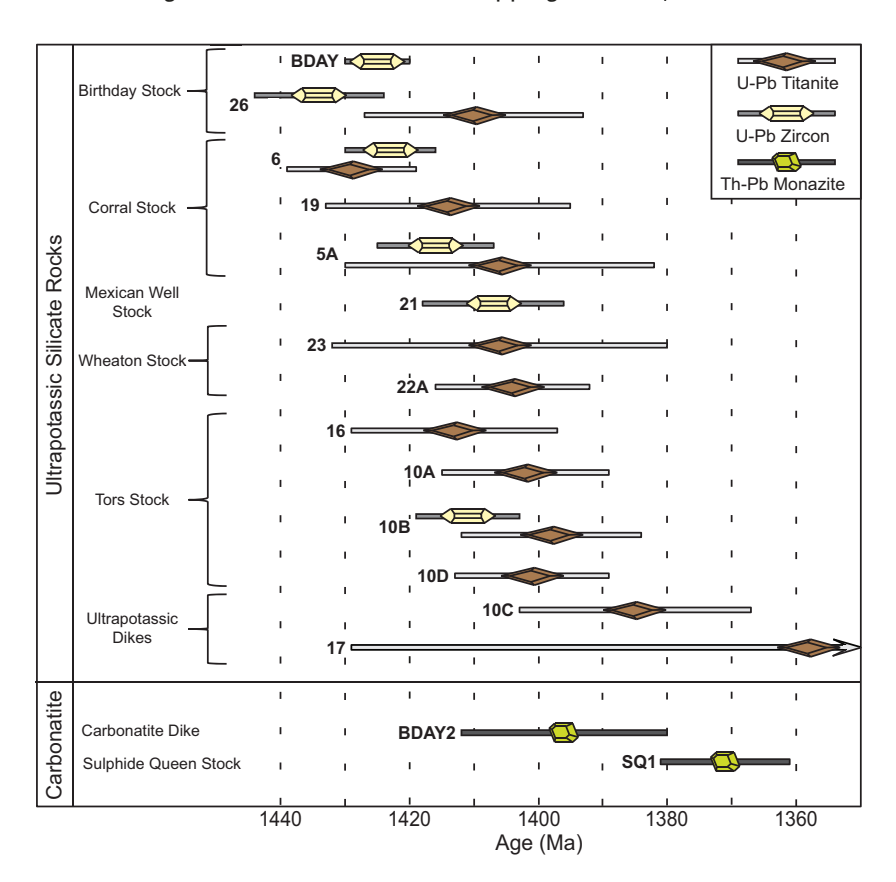


Fig. 15. Summary of titanite, zircon, and monazite dates from all samples analyzed in this study. Each date and associated uncertainty is from all analyses of a specific mineral interpreted as an age. It should be noted that the uncertainty of one sample extends to the right beyond the width of the plot ('17' = MP-P0714-17, titanite date =  $1358 \pm 71 \,\text{Ma}$ ). Locations of samples in the field area are indicated.

monazite and bastnäsite in MPIS carbonatite (Fig. 8). The overlap of  $\varepsilon Nd_i$  of the carbonatite and the most primitive  $\varepsilon Nd_i$  of the ultrapotassic rocks supports the idea that they are related and probably derived from a common source.

In contrast to titanite Nd isotopic data, zircon  $\epsilon Hf_i$  from Mesoproterozoic zircon in the same rocks does not systematically differ within or between samples, with all data from all samples giving a weighted mean of  $1.9\pm0.2$  (MSWD=0.9, Fig. 12). These data support the hypothesis that MPIS ultrapotassic rocks are all derived from the same source and, more regionally, coincide with previously reported zircon  $\epsilon Hf_i$  for  $\sim1.4$  Ga granitoids throughout the Mojave Desert (Wooden et al., 2012, Fig. 1a).

Variable titanite  $\epsilon Nd_i$  and consistent zircon  $\epsilon Hf_i$  indicate that the Nd isotopic signature of some titanite has been influenced by a process that did not have a noticeable effect on zircon  $\epsilon Hf_i$ . Possible explanations include (1) magma mixing, (2) contamination of the magma by wall-rock, and/or (3) post-crystallization disturbance of the Nd isotopic system in titanite.

Pankhurst *et al.* (2011) attributed variable titanite εNd<sub>i</sub> values in an A-type granite to mixing of parental magmas. DeWitt *et al.* (2000) interpreted Pb and Nd isotope data to record mixing of melts derived from mantle and lower crustal sources of variable age to produce the MPIS carbonatite magma. Thus, some variability in titanite εNd<sub>i</sub> from MPIS ultrapotassic rocks may be attributable to mixing between magmas from different source regions with different Nd isotopic signatures. However, the same variability is not observed in carbonatite or the youngest ultrapotassic rocks, suggesting

that this may be the case only for the earliest MPIS rocks (Fig. 8).

The low εNd; in titanite from ultrapotassic rock samples may be explained by assimilation of crustal material, either the host-rocks exposed at Mountain Pass or unexposed basement rocks of the Mojave Crustal Province. This hypothesis is supported by the general decrease in ENd; with increasing SiO2 content in the oldest ( $\sim$ 1430–1420 Ma) and youngest ( $\sim$ 1380–1370 Ma) MPIS samples (Fig. 8) — assimilation of felsic country rock and accompanying fractional crystallization would have increased the SiO2 content of the magmas. A binary mixing model demonstrates that the variability in Nd isotopic signatures of MPIS titanite can be explained by assimilation (Fig. 16). In this model, mean titanite εNd<sub>i</sub> values are used to approximate whole-rock εNd<sub>i</sub> for each sample, parameters for the primary magma are estimated based on the most primitive MPIS samples ( $\sim$ 45 wt % SiO<sub>2</sub>,  $\sim$ 325 ppm Nd,  $\epsilon$ Nd  $\sim$  –3), and parameters for the contaminant are estimated using 70 wt % SiO<sub>2</sub> to approximate a granitic (sensu lato) composition. Using these parameters, ~70% contaminant and ~30% primary magma would be required to produce the MPIS sample with the highest silica content (MP-P0913-5A,  $\sim$ 65 wt % SiO<sub>2</sub>) through binary mixing. Assuming that MP-P0913-5A is 70% contaminant, a curve fit to the MPIS samples in εNd vs 1/Nd space defines a contaminant end-member with  $\epsilon Nd \sim -15$  and a Nd concentration of  $\sim$ 150 ppm (Fig. 16). Nd abundance and isotopic data have not been reported for Mountain Pass host-rocks, making the definition of this endmember difficult. Additionally, a binary mixing model is oversimplification, perhaps fractional as

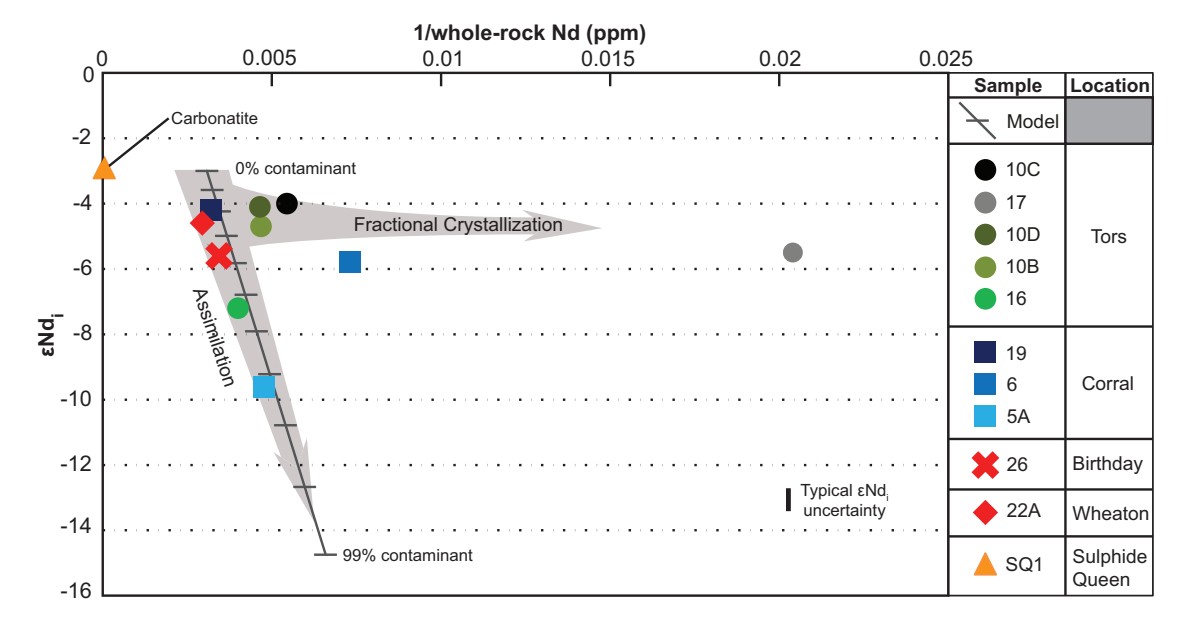


Fig. 16. Nd isotope binary mixing model for MPIS rocks. Each data point is a mean titanite  $\epsilon Nd_i$  value from all analyses in one sample, used here to approximate whole-rock  $\epsilon Nd_i$ . Typical uncertainty on the mean  $\epsilon Nd_i$  is shown by the vertical bar at the lower right ( $\pm 0.7$   $\epsilon$ -units). Each bar on the mixing model line represents 10% increments (i.e. addition of 10% contaminant to the original magma).

crystallization must have accompanied assimilation and would also have increased the SiO2 content of the evolving magma. However, an assimilation-fractional crystallization model (DePaolo, 1981) with a ratio of assimilation rate to fractional crystallization rate (r) = 1and relatively high bulk partition coefficient (D) = 0.8-1.2 for Nd (estimated based on the high proportion of apatite and titanite in the most primitive samples) yields a very similar result. In summary, a binary mixture of  $\sim$ 30% primary magma with 325 ppm Nd,  $\epsilon$ Nd = -3, and 45 wt % SiO<sub>2</sub> and  $\sim$ 70% contaminant with  $\sim$ 150 ppm Nd,  $\varepsilon$ Nd = -15, and  $\sim$ 70% SiO<sub>2</sub> would be required to produce MP-P0913-5A (mean  $\epsilon Nd_i \sim -9.6$  and  $\sim 65$  wt % SiO<sub>2</sub>, Figs 8 and 16). MP-P0913-5A contains abundant inherited zircon grains (Fig. 10b) and xenoliths of host gneiss and granite, providing direct evidence of crustal assimilation. Samples MP-P0913-6 and MP-P0714-17 fall off of the mixing curve and can be explained by a combination of fractional crystallization and assimilation ( $\leq$ 40% assimilation; Fig. 16).

The uniformity of the zircon EHfi in MPIS rocks indicates that the Hf isotope compositions of the magmas were unaffected by contamination. This could be explained by a contaminant with a very low Hf concentration relative to the primary magmas. Primitive MPIS samples contain ~12 ppm Hf (Table 2), requiring the Hf content of the contaminant to be  $< \sim 2 \text{ ppm}$  based on the mixing parameters above. It is more likely that zircon was the dominant Hf reservoir in the contaminant and was not dissolved when incorporated into the ultrapotassic magma, resulting in contamination of the magma without a noticeable effect on the Hf isotopic composition of the melt. This is feasible, given the high distribution coefficient ( $K_d$ ) for Hf between zircon and common silicate melts (e.g. Mahood & Hildreth, 1983; Fujimaki, 1986), and because of the abundance of euhedral (apparently undissolved), inherited zircon in some MPIS samples. An alternative explanation is that the MPIS and its host-rocks have a similar Hf isotopic composition. However, this would suggest that the hostrocks plot far above the εHf<sub>i</sub>-εNd<sub>i</sub> terrestrial array of Vervoort et al. (1999); that is, they have  $\varepsilon Hf_i$  between  $\sim 2$ and 0, and  $\epsilon Nd_i \approx -15$  (from the model presented above); this is therefore an unlikely explanation.

Post-crystallization disturbance of the Nd isotopic system in titanite could also explain the source of Nd isotopic variation in at least two samples (MP-P0714-16 and MP-P0714-26). These samples yielded two subpopulations of U-Pb data (Fig. 6), and also have some of the lowest and most variable  $\epsilon$ Nd<sub>i</sub> values (as low as – 10·7; Fig. 8). Titanite from these samples may record the  $\epsilon$ Nd<sub>i</sub> of an altering fluid that post-dated crystallization (e.g. Shawe, 1952), in addition to potential mixing of magma from different sources and/or magma contamination by wall-rock. The variable  $\epsilon$ Nd<sub>i</sub> and relatively low silica content in these two samples alone suggests that magma contamination may be a less likely scenario to account for their Nd isotopic composition. Furthermore, post-crystallization disturbance of titanite

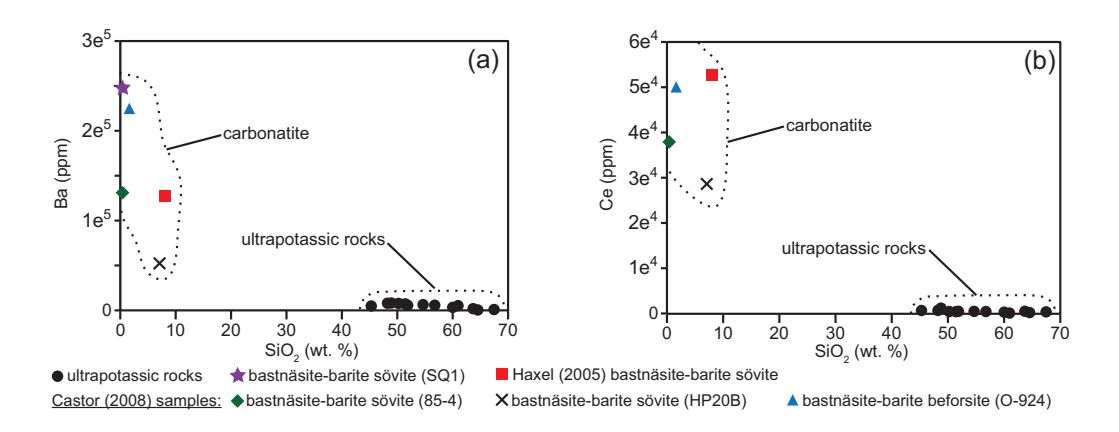
provides a potential explanation for the subtle loss of radiogenic Pb observed in these two samples. We favor this interpretation over disturbance to the U–Pb system in these samples by later intrusion of magma, because the latter scenario does not explain the variability in  $\epsilon Nd_i$  in these samples.

In summary, mineral-scale Nd and Hf isotopic data reported here are interpreted to indicate derivation of Mountain Pass ultrapotassic rocks and carbonatite from the same source, potential mixing of magma from two or more sources to produce these magmas, and crustal contamination of some of the ultrapotassic magmas. Post-crystallization disturbance of the Nd isotopic signature in titanite by a secondary fluid can convincingly be demonstrated in only two of the analyzed samples.

# Petrogenetic model for the Mountain Pass Intrusive Suite

Despite the temporal overlap between ultrapotassic and carbonatite magmatism at Mountain Pass, available data suggest that the two are unlikely to have differentiated from a common parental melt. Derivation of the carbonatite from a silicate melt by fractional crystallization implies either that the carbonatite is a cumulate that crystallized from a silicate melt (e.g. Gittins & Harmer, 2003; Downes et al., 2005) or that it is the most evolved member of the suite and represents a latestage, residual liquid. It seems unlikely that the carbonatite is a cumulate because it does not fall along an evolutionary trend with the ultrapotassic rocks (Fig. 17a and b). Furthermore, a cumulate should be composed primarily of crystals and is therefore unlikely to intrude subsequently as cross-cutting dikes or to differentiate into different types of carbonatite (i.e. sövite and beforsite); additionally, it should contain trapped intercumulus material that represents the silicate melt from which it crystallized, which is not observed.

Alternatively, if the carbonatite represents a latestage, residual liquid, incompatible elements that are abundant in the carbonatite (i.e. Ba, Sr, LREE) should be least abundant in primitive (i.e. low-silica) members of the MPIS ultrapotassic suite and most abundant in evolved (i.e. high-silica) members. However, the most primitive members of the MPIS ultrapotassic suite have the highest Ba, Sr, and LREE, whereas the most evolved members have the lowest contents of these elements (Fig. 3). Furthermore, the carbonatite and ultrapotassic rocks do not occur in a concentrically zoned, plug-like intrusion with a relatively small core of carbonatite surrounded by alkaline silicate rocks, as has been documented in other locations and cited as evidence for carbonatite representing a volumetrically small, latestage residual liquid (e.g. Juquiá complex in Brazil, Beccaluva et al., 1992; Salmagorskii complex in Russia, Korobeinikov et al., 1998). On the contrary, field evidence shows that the carbonatite and ultrapotassic magmas were emplaced separately (e.g. Fig. 2d),



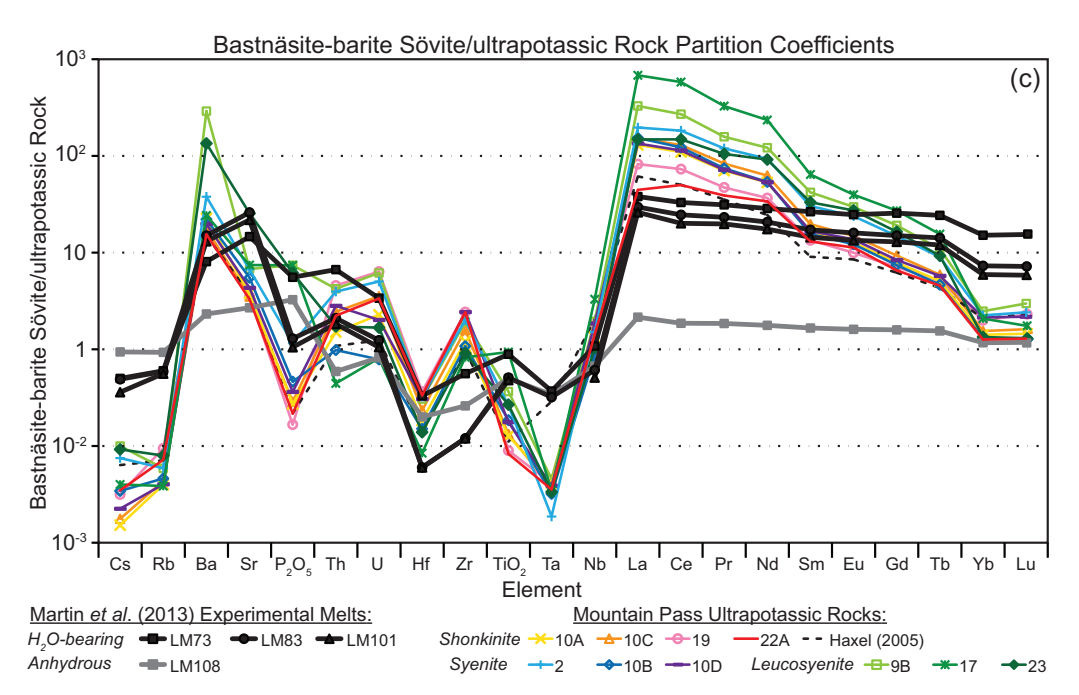


Fig. 17. Whole-rock variation diagrams and carbonatite/ultrapotassic rock trace element ratio plot for MPIS rocks. (a) Ba vs silica plot for MPIS carbonatite and ultrapotassic rocks. (b) Ce vs silica plot for MPIS carbonatite and ultrapotassic rocks. Sample SQ1 is not shown, but contains ∼138 000 ppm Ce and <1 wt % SiO₂ and thus plots above the carbonatite samples shown. (c) Bastnäsite–barite sövite/ultrapotassic rock trace element patterns for MPIS rocks. Experimental data shown for comparison are from Martin et al. (2013). Bastnäsite–barite sövite data are from Haxel (2005); the plotted elements are all of those that are available from this dataset. Samples MP-P0913-5A, MP-P0913-6, MP-P0714-16, and MP-P0714-26 are interpreted as being contaminated based on Nd isotopes, and are not shown, but plot similarly to samples shown here.

requiring that a parental magma would have had to undergo protracted fractional crystallization prior to mobilization and emplacement of its products. Taken together, these data indicate that if the carbonatite and ultrapotassic rocks were derived from a common parental melt, liquid immiscibility and physical separation of carbonatite and ultrapotassic melts would have to have occurred at some point along its evolutionary path.

Partition coefficients between immiscible carbonatite and silicate liquids have been determined for a number of elements by experimental studies (e.g. Veksler *et al.*, 1998, 2012; Martin *et al.*, 2012, 2013), providing a quantitative method for evaluating whether or not carbonatite and alkaline silicate rocks at a given locality are potentially related by liquid immiscibility. We compared the experimental data of Martin *et al.* (2013) from H<sub>2</sub>O-

bearing, potassic systems with MPIS data from Haxel (2005), Castor (2008), and this study to test the liquid immiscibility hypothesis for MPIS ultrapotassic rocks and carbonatite. Although the experiments of Martin *et al.* (2013) were performed at higher pressures (1–3 GPa) than that of the MPIS emplacement (~0·1 GPa), the experiments of Veksler *et al.* (1998) were carried out at lower pressures (<1 GPa) and yielded similar results for melts of comparable composition.

The ratios of trace elements between MPIS carbonatites [bastnäsite-barite sövite from Haxel (2005)] and ultrapotassic rocks (from this study) are significantly different from the experimentally derived carbonatite-silicate partition coefficients of Martin *et al.* (2013). The MPIS carbonatite/ultrapotassic rock ratios are lower for  $P_2O_5$ ,  $TiO_2$ , Cs, Rb, and HREE, and higher for Zr than the

experimental melts (Fig. 17). Additionally, ratios are lower for Ta in all but one sample, and higher for LREE in all but one sample. Carbonatite/ultrapotassic rock trace element ratios for bastnäsite-barite sövite analyzed in this study show similar differences from the experimental data, and are also lower for K<sub>2</sub>O, Na<sub>2</sub>O, Al<sub>2</sub>O<sub>3</sub>, and Zr, and higher for Pb and LREE (see Supplementary Data Electronic Appendix 13 for partition coefficient plots). Carbonatite/ultrapotassic rock trace element ratios calculated with MPIS carbonatite samples from Castor (2008) (sövite, dolomitic sövite, and beforsite) show similar discrepancies.

A key difference between the MPIS carbonatite and experiments is that experimental immiscible carbonatite liquids are invariably alkali-rich (e.g. Veksler et al., 1998, 2012; Martin et al., 2012, 2013), whereas MPIS carbonatite is distinctly alkali-poor (Na<sub>2</sub>O +  $K_2O$  < 2). However, this may be due in part to late-stage alkali loss, which some researchers have argued is common in carbonatites (Bell et al., 1999; Martin et al., 2013), and may also have resulted in depletion of large ion lithophile elements (LILE) such as Cs and Rb. Regardless of alkali content, carbonatite/ultrapotassic rock ratios for a multitude of elements differ from those of experimental immiscible carbonatite-potassic silicate melts, and suggest that the MPIS rocks are unlikely to be related by liquid immiscibility. This suggests, then, that MPIS carbonatite was generated as a primary carbonatitic melt.

A number of studies have contended that some, if not most, carbonatites are primary, mantle-derived melts (e.g. Harmer & Gittins, 1998; Harmer, 1999; Gittins & Harmer, 2003; Ying et al., 2004). In cases where primary carbonatites are associated with alkaline silicate rocks, the two may still be closely related despite being generated from separate melts. A number of studies have shown that carbonatite melts may metasomatize mantle rocks (e.g. Green & Wallace, 1988; Yaxley et al., 1991; Hauri et al., 1993; Rudnick et al., 1993), and Harmer (1999) presented a model in which these rocks may later partially melt and produce alkaline silicate melts. In this model, the alkaline silicate melts ascend with the assistance of volatiles, and subsequent carbonatite melt ascends by exploiting the conduit formed by earlier silicate melts and without significant interaction with countryrock. This model is consistent with the age and isotopic relationships of the MPIS in that (1) the earliest and most voluminous stages of magmatism resulted in the emplacement of alkaline silicate rocks, (2) alkaline silicate magmatism progressively decreased in volume and carbonatite magmatism progressively increased in volume, and (3) the carbonatite and silicate rocks have similar isotopic characteristics owing to their derivation from the same source, although the silicate rocks have more variable isotopic signatures as a result of crustal contamination. Although the composition of the ultrapotassic rocks and carbonatite are somewhat different from those in the model of Harmer (1999), this model provides an appropriate analog for the petrogenesis of the MPIS.

#### **Tectonic setting of the MPIS**

The spatial relationship and temporal overlap between the MPIS and ~1.4 Ga granitoids of similar age throughout the southwestern USA suggests that both were emplaced in response to the same thermal event (Haxel, 2005) and in a similar tectonic regime (Gleason et al., 1994). Although some studies have postulated an anorogenic origin for the ~1.4 Ga granitoids (e.g. Anderson & Bender, 1989; Hoffman, 1989), more recent studies have concluded that they were associated with a contractional orogenic event (e.g. Nyman et al., 1994; Daniel & Pyle, 2006; Whitmeyer & Karlstrom, 2007; Daniel et al., 2013). Alkaline and carbonatitic magmatism has been documented in contractional settings in other locations (e.g. Tilton et al., 1998; Wang et al., 2001; Ying et al., 2004), and commonly occurs peripherally to orogens (e.g. Veizer et al., 1992; Jones et al., 2013) or larger subalkaline igneous provinces (e.g. Gibson et al., 2006; Ernst & Bell, 2010). The occurrence of a belt of ultrapotassic rocks (including the MPIS) along the westernmost edge of a large, ~1.4 Ga granitoid suite (Castor, 2008) that may have been emplaced in an orogenic environment is consistent with this scenario. The ultrapotassic and carbonatite magmas and granitoid magmas were probably derived from distinct sources (Gleason et al., 1994; Haxel, 2005), which may have been juxtaposed to the east of the ultrapotassic belt, and both partially melted during a widespread and long-lived thermal event.

### Implications for carbonatite-alkaline magmatism

The MPIS does not have a direct analog because of its unique features (Haxel, 2005; Castor, 2008), including the wide range of silica contents in the ultrapotassic rocks, the association between ultrapotassic (rather than potassic) rocks and significant amounts of carbonatite, and the geochemistry of the shonkinite and carbonatite, preventing direct comparison with other carbonatite-alkaline rock occurrences worldwide. However, the MPIS is most akin to the group of carbonatite-alkaline rock occurrences in which the two rock types are spatially and temporally associated but were generated as separate melts-for example, the Spitskof, Shawa, Dorowa, Kerimasi, and Napak complexes in Africa (Harmer & Gittins, 1998; Harmer, 1999), and the Jacupiranga complex in southern Brazil (Huang et al., 1995).

# **CONCLUSIONS**

Whole-rock and mineral geochemistry data from the MPIS indicate that titanite, zircon, apatite, thorite, and sodic amphibole are the most important hosts of REE and actinides in the ultrapotassic rocks. Titanite and zircon from ultrapotassic rocks yield U–Pb ages of  $\sim$ 1425–1385 Ma and  $\sim$ 1425–1407 Ma, respectively, and record three discrete phases of magmatism ( $\sim$ 1425,  $\sim$ 1405, and  $\sim$ 1380 Ma; Fig. 15). Trace element and textural data

indicate that titanite grew as an igneous phase in Mountain Pass rocks. Titanite yields identical dates to demonstrably igneous zircon, and is therefore interpreted to accurately record the igneous crystallization ages of the MPIS. Monazite Th-Pb ages from carbonatite are 1400-1380 Ma (Fig. 15) and overlap titanite and zircon dates from ultrapotassic rocks within uncertainty. Hf isotopic data from zircon in the ultrapotassic rocks are uniform, yielding a mean  $\varepsilon Hf_i$  of  $1.9 \pm 0.2$  across all samples (Fig. 12), indicating derivation from a common source. The most primitive Nd isotopic values measured in titanite overlap εNd; from monazite and bastnäsite in the carbonatite (Fig. 8), further supporting a genetic relationship between the carbonatite and ultrapotassic rocks of the MPIS. Whole-rock major and trace element data suggest that the carbonatite and ultrapotassic rocks are unlikely to have differentiated from a common parental magma. Combined, data from this study effectively demonstrate and resolve—contrary to previous studies—that carbonatite and ultrapotassic rocks younger than  $\sim$ 1410 Ma were contemporaneous, but were derived from separate melts from the same source region. In this way, the MPIS is most similar to carbonatite-alkaline rock suites in which the two rock types were generated as separate melts. We speculate that REE deposits of similar grade to the Mountain Pass may be more likely to occur in primary carbonatites than in carbonatites that separated from parental silicate melts.

### **APPENDIX: ANALYTICAL METHODS**

# **Accessory minerals**

Sample preparation

Accessory minerals were analyzed either in epoxy grain mounts or in thin section. Sample thin sections were prepared by Spectrum Petrographics of Vancouver, Washington. To prepare mineral separates,  $\sim$ 2–3 kg of each sample was crushed in a jaw crusher and disc mill, sieved, separated by density using a gold pan or Rodgers Table and then in methylene iodide ( $\rho = 3.32 \,\mathrm{g}$ cm<sup>-3</sup>), and separated by magnetic susceptibility using a Frantz isodynamic separator. Thirty to 50 grains of each mineral were picked from samples by hand under a binocular microscope, mounted in epoxy pucks, and polished to a 0·25 μm (titanite, monazite, apatite, bastnäsite) or 1 µm (zircon, rutile) finish. Backscattered-electron (BSE) and cathodoluminescence (CL) images of the samples were collected using scanning electron microscopy (SEM) to provide textural context for LASS-ICP-MS spot analysis placement. Representative example SEM images of sample grains with spot analyses shown are provided in Supplementary Data Electronic Appendix 3.

## U-Th-Pb

Mineral analyses were carried out using LASS-ICP-MS at the University of California, Santa Barbara (UCSB). The LASS-ICP-MS system combines a Photon Machines 193 nm ArF Excimer laser and Hel-Ex ablation cell with a Nu Instruments HR Plasma high-resolution MC-ICP-

MS system for collecting U-Th/Pb data and an Agilent 7700S quadrupole (Q)-ICP-MS system for collecting major and trace element data. Methods used in this study follow those outlined by Cottle et al. (2012, 2013) and Kylander-Clark et al. (2013), except that trace elements were measured via Q-ICP-MS (method outlined below). Different laser run conditions were used for each mineral depending on expected U, Th, and Pb content, varying in the range of 9-40 µm spot size, 3-7 mJ laser power at 75-100%, laser pulse frequency 3-4 Hz, and 80-120 shots per analysis (see Supplementary Data Electronic Appendices 5, 7, 10 and 11). Bastnäsite was ablated using line scans 25 μm wide and 100 μm long with a travel rate of 4 µm s<sup>-1</sup>. Before each ablation period, the laser was fired twice to remove contamination from the surface of the analyte, followed by an 8s delay to permit sample washout. Masses <sup>204</sup>Pb + Hg, <sup>206</sup>Pb, <sup>207</sup>Pb, and <sup>208</sup>Pb were measured on ion counters, and <sup>232</sup>Th and <sup>238</sup>U were measured on Faraday detectors. Typically, 20-40 analyses were performed per sample, according to the abundance of the mineral of interest per sample. Every set of eight sample analyses was bracketed by analyses of a primary and a secondary natural reference material of the same mineral type as the sample. Information about the primary and secondary reference materials used is provided in Supplementary Data Electronic Appendix 14. Bastnäsite is the only exception, owing to the lack of а widely distributed and/or well-characterized bastnäsite reference material; therefore, zircon and monazite were used as reference materials for bastnäsite and all three minerals were ablated using line scans to avoid addition of systematic uncertainty owing to differences in downhole fractionation of U and Pb. Zircon data were acquired during seven separate analytical sessions, monazite data over four, rutile data over one, and titanite, bastnäsite, and apatite over two sessions each.

Raw U-Th-Pb and trace element data were reduced using lolite v2.5 (Paton et al., 2011) to correct for instrument drift, laser-ablation-induced down-hole elemental fractionation, plasma-induced elemental fractionation, and instrumental mass bias. Secondary reference materials were used to monitor accuracy and internal reproducibility from run to run, and between analytical sessions. External uncertainty was added to sample isotopic ratios in quadrature, and was assigned based on the additional uncertainty needed to produce an MSWD  $\sim$ 1 in a population (n>9) of secondary reference material analyses from the same analytical session.  $^{206}\text{Pb}/^{238}\text{U}$  typically required the addition of  $\sim\!1\text{--}1.5\%$ external uncertainty. 207Pb/206Pb measurements usually required addition of <1% uncertainty. However, longterm <sup>207</sup>Pb/<sup>206</sup>Pb reproducibility for this laboratory and setup is reported to be 1.5-2% (e.g. Kylander-Clark et al., 2013; Spencer et al., 2013); thus, 1.5% external uncertainty has been added to all <sup>207</sup>Pb/<sup>206</sup>Pb ratios to account for long-term accuracy. U-Th/Pb data collected

from the secondary reference materials are shown in Supplementary Data Electronic Appendix 15.

Isoplot 4.1 (Ludwig, 2012) was used to plot U–Pb data on Tera–Wasserburg diagrams, to calculate lower-intercept and concordia dates, and to calculate weighted means. Reported titanite ages are U–Pb isochron dates derived from Tera–Wasserburg plots. Zircon ages are U–Pb concordia dates derived from Tera–Wasserburg plots for samples that yield MSWD  $< 1 + 2(2/f)^{1/2}$ , where f = n - 2 (Wendt & Carl, 1991). For samples that do not yield a concordia age that meets this criterion, reported ages are weighted means of  $^{207}$ Pb/ $^{206}$ Pb dates calculated from measured  $^{207}$ Pb/ $^{206}$ Pb ratios. Zircon dates were calculated using data that are < 3% discordant; per cent discordance was calculated as the per cent difference between the  $^{207}$ Pb/ $^{206}$ Pb and  $^{206}$ Pb/ $^{238}$ U dates from the corresponding isotopic ratios measured in the sample.

All reported monazite ages are common-Pb corrected <sup>208</sup>Pb/<sup>232</sup>Th dates. Correction was applied according to the following steps. (1) Raw <sup>232</sup>Th, <sup>208</sup>Pb, and <sup>204</sup>Pb + Hg signals were corrected for instrumental drift and mass bias in Iolite v2.5 (Paton et al., 2011). (2) Per cent common <sup>208</sup>Pb in the <sup>208</sup>Pb signal was calculated based on the mass-204 signal and the 208Pb/204Pb at a reference age of 1400 Ma from the Stacey & Kramers (1975) model of Pb evolution. Changes in the reference age of <100 Myr did not significantly change the final <sup>208</sup>Pb/<sup>232</sup>Th date (<1 Myr). The mass-204 signal was not corrected for isobaric interference of <sup>204</sup>Hg on <sup>204</sup>Pb; however, the possible presence of Hg in the Ar gas supply should be accounted for in the background mass-204 signal, and we therefore consider the effect of neglecting this correction insignificant. (3) Radiogenic <sup>208</sup>Pb (<sup>208</sup>Pb\*) was calculated by subtracting the common <sup>208</sup>Pb from the total measured <sup>208</sup>Pb. (4) Corrected <sup>208</sup>Pb\*/<sup>232</sup>Th ratios were used to calculate <sup>208</sup>Pb/<sup>232</sup>Th dates. Uncertainties were calculated by the same method as was used to calculate uncertainty for 206Pb/238U and 207Pb/206Pb ratios as described above, with an additional 1% added in quadrature for uncertainty on the 208Pb/204Pb ratio from the Stacey & Kramers (1975) model. Measured <sup>208</sup>Pb/<sup>232</sup>Th ratios of the reference materials typically required addition of  $\sim$ 3% uncertainty.

#### Trace elements

Trace elements of interest were measured in titanite, zircon, monazite, and apatite by LASS-ICP-MS simultaneously with U-Th-Pb isotopes using an Agilent 7700 S Q-ICP-MS system; laser settings, ablation periods, and washout times used for trace element measurement were therefore identical to those described above. Zircon grains that appear to be metamict (see below) were also measured using LA-Q-ICP-MS for U-Th-Pb isotopes and trace elements of interest; analytical methods were otherwise identical to those used for titanite, zircon, monazite, and apatite. The Q-ICP-MS system is equipped with a second Edwards E2M 18 rotary interface pump, increasing sensitivity by about two-fold for

elements heavier than Mg. The Q-ICP-MS system was tuned such that ThO<sup>+</sup> and CeO<sup>+</sup> were less than  $\sim$ 0.5%, and doubly charged ions less than 2%. Dwell time for elements of stoichiometric abundance (e.g. Ca, Ti, and Si for titanite; Zr and Si for zircon) was 5 ms. A dwell time of 10 ms was used for trace elements with expected abundances of 10 000-1000 ppm (e.g. REE in titanite; Hf in zircon). For trace elements with expected abundances of ~1000 ppm or less, or those that were used for geothermometry (e.g. Zr in titanite. Ti in zircon), dwell time was set to 20 ms. Sweep time was ~0.8 s. Analog detection mode was used for elements of stoichiometric abundance; pulse-counting mode was used for most elements and allowed to switch to analog mode automatically. Masses monitored during analysis are listed in Supplementary Data Electronic Appendix

'GJ1' zircon was used as the primary reference material for most trace elements in zircon samples [see Liu et al. (2010) for trace element reference values]. '91500' zircon was used as the primary reference material for Si, P, and Ta, because of the lack of 'accepted' values for these elements in 'GJ1' zircon. Trace element reference values used for '91500' are from the GeoReM database, application version 18 (October 2009; http:// georem.mpch-mainz.gwdg.de/) (Jochum et al., 2005). 'Stern' monazite was used as the primary reference material for monazite trace elements (reference values based on data compiled from UCSB LASS-ICP-MS and electron probe micro-analyzer laboratories). NIST SRM610 reference glass (Jochum et al., 2011) was measured in conjunction with titanite, apatite, and metamict zircon and used as the primary trace element reference material for these phases. Secondary trace element reference materials used are the same as the primary U-Pb reference materials (Supplemetary Data Electronic Appendix 14). Trace element data were reduced using the 'trace elements' data reduction scheme in Iolite v2.5 (Paton et al., 2011). Zircon and monazite trace element data were reduced using the 'semi-quantitative' standardization method of lolite. Ca was used as an internal standard for titanite and apatite, and Si was used as an internal standard for metamict zircon; Ca and Si values were assumed stoichiometric. These standardization schemes reproduced values in the secondary reference materials to within 10% or less for most trace elements. REE plots are normalized to the chondrite concentrations of McDonough & Sun (1995).

Zr-in-titanite apparent temperatures were calculated using the calibration of Hayden *et al.* (2008). Pressure was assumed to be  $0.1\pm0.1$  GPa based on the presence of K-feldspar pseudomorphs after primary leucite in some samples (Castor, 2008), which has been experimentally shown to be unstable above  $\sim\!0.1$  GPa (Barton & Hamilton, 1978). Ti-in-zircon apparent temperatures were calculated using the calibration of Ferry & Watson (2007). For both geothermometers, TiO<sub>2</sub> activity was assumed to be  $0.8\pm0.2$ , based on the apparent lack of

primary rutile, and  $SiO_2$  activity to be unity, based on the presence of minor quartz. For samples where quartz was not observed in thin section,  $SiO_2$  activity was assumed to be  $0.9 \pm 0.1$ . Uncertainty in elemental concentration (2SE),  $TiO_2$  activity, and  $SiO_2$  activity are propagated into the reported temperature uncertainties. Additionally, uncertainty in pressure is propagated in the reported Zr-in-titanite apparent temperatures. Temperatures quoted here are weighted means calculated by Isoplot 4.1 (Ludwig, 2012), or are a range of values from non-single population groups of analyses.

## Nd isotopes

Nd isotopes in titanite, monazite, and bastnäsite were measured in situ by LA-MC-ICP-MS at UCSB. The methods presented by Fisher et al. (2011b) were followed for this study, and are summarized here. For titanite and monazite, only grains that were analyzed for U-Pb geochronology were analyzed for Nd isotopes, with the exception of one sample (MP-P0913-10B). All minerals were ablated with 5 mJ laser energy at 100% and pulse rate of 6 Hz for each analysis. Laser spot sizes were  $65\,\mu m$  for titanite,  $20\,\mu m$  for monazite, and  $15\,\mu m$  for bastnäsite. Reference glasses were ablated with a spot size of 40 um to obtain an optimal signal during monazite and bastnäsite analysis, and 65 µm during titanite analysis. Samples were ablated for 50s, with a 30s delay between analyses to allow washout. Masses 141-150 were measured on 10 Faraday cups with 1 a.m.u. spacing. Data were reduced using lolite v2.5 (Paton et al., 2011). The data were carefully screened to detect the presence of inclusions; portions of analyses that appeared to record measurement of inclusions were rejected during data processing.

During in situ measurement of Nd isotopes, the isobaric interference on <sup>144</sup>Nd by <sup>144</sup>Sm has been noted to constitute between 1.5 and 4.6% of the mass-144 signal in LREE-rich minerals (Fisher et al., 2011b); thus, correcting this interference is vital to obtaining an accurate <sup>143</sup>Nd/<sup>144</sup>Nd ratio. In addition, determination of <sup>147</sup>Sm/<sup>144</sup>Nd in the sample is necessary to accurately calculate the initial <sup>143</sup>Nd/<sup>144</sup>Nd of the sample. To make these corrections, instrumental mass bias factors for Sm and Nd must first be determined. 'JNdi-1' glass was employed to evaluate Nd isotopic measurements withinterference complication by isobaric  $(^{143}Nd/^{144}Nd = 0.512115 \pm 7; Tanaka et al., 2000). 'JNdi-$ 1' doped with Ce, Pr, Sm, Eu, and Gd ('LREE' glass; Fisher et al., 2011b) was employed to provide a homogeneous 147Sm/144Nd reference material, and to evaluate Nd isotope measurements where Sm is included. <sup>147</sup>Sm/<sup>149</sup>Sm was used to calculate a Sm mass bias factor, using a natural 147Sm/149Sm ratio of 0.22332 (Isnard et al., 2005). 144Sm interference was then calculated using the measured <sup>149</sup>Sm and a natural <sup>144</sup>Sm/<sup>149</sup>Sm ratio of 1.08680 (Dubois et al., 1992). For Nd mass bias determination, a natural <sup>146</sup>Nd/<sup>144</sup>Nd ratio of 0.7219 was used. A canonical 145Nd/144Nd value of 0.348415

(Wasserburg *et al.*, 1981) was used to monitor the accuracy of the Nd mass bias correction.  $^{147} \rm Sm/^{144} \rm Nd$  was calculated using the mass bias corrected  $^{147} \rm Sm$  and the interference corrected  $^{144} \rm Nd$ . Natural reference materials 'Trebilcock' monazite ( $^{143} \rm Nd/^{144} \rm Nd = 0.512616 \pm 11$ ; Fisher *et al.*, 2011*b*) and 'Hondo Canyon' titanite ( $^{143} \rm Nd/^{144} \rm Nd = 0.512211 \pm 9$ ; Fisher *et al.*, 2011*b*) were analyzed between every 10–20 unknowns and used to monitor the accuracy of the corrected  $^{143} \rm Nd/^{144} \rm Nd$  and  $^{147} \rm Sm/^{144} \rm Nd$  ratios. The weighted mean corrected  $^{143} \rm Nd/^{144} \rm Nd$  values ( $\pm 2 \rm SD$ ) obtained for the reference materials are as follows:  $0.512612 \pm 18$  ( $n\!=\!34$ ) for Trebilcock monazite;  $0.512218 \pm 59$  ( $n\!=\!24$ ) for Hondo Canyon titanite.

The  $\epsilon Nd_i$  values were calculated relative to the chondritic uniform reservoir (CHUR) parameters of Jacobsen & Wasserburg (1980) (present-day  $^{143}Nd/^{144}Nd=0.512638$  and  $^{147}Sm/^{144}Nd=0.1967$ ) with  $^{143}Nd/^{144}Nd$  re-normalized to  $^{146}Nd/^{144}Nd=0.7219$  (Hamilton *et al.*, 1983; Bouvier *et al.*, 2008). Age corrections on the measured  $^{143}Nd/^{144}Nd$  were applied using the sample age interpreted from titanite and/or zircon dates; changes of  $\sim\!20$  Myr in the correction age did not have a drastic effect on the epsilon values ( $\sim\!0.2$  epsilon units). Uncertainties on the measured  $^{143}Nd/^{144}Nd$  and  $^{147}Sm/^{144}Nd$  ratios were propagated into the  $\epsilon Nd_i$  values.

## Hf isotopes

Hf isotopes in zircon were measured *in situ* by LA-MC-ICP-MS at UCSB. Methods used in this study are similar to those used by Hagen-Peter *et al.* (2015), and are summarized here. Only zircon grains that were analyzed for U–Pb geochronology and yielded concordant dates younger than  $\sim\!1460\,\text{Ma}$  were analyzed for Hf isotopes. Ablation spots were placed over the original U–Pb analysis spots to obtain Hf compositions that correspond to the measured U–Pb date of the zircon. A laser spot size of 50  $\mu\text{m}$ , 4 mJ laser energy at 100%, and a pulse rate of 8 Hz were used to ablate samples for 50 s, with a 30 s delay between analyses to allow washout. Masses 171–180 were measured on 10 Faraday cups with 1 a.m.u. spacing.

Data were reduced using lolite v2.31 (Paton *et al.*, 2011). Natural ratios of <sup>176</sup>Yb/<sup>173</sup>Yb = 0.786847 (Thirlwall & Anczkiewicz, 2004) and <sup>176</sup>Lu/<sup>175</sup>Lu = 0.02656 (Chu *et al.*, 2002) were used to subtract isobaric interferences of <sup>176</sup>Yb and <sup>176</sup>Lu on <sup>176</sup>Hf. The Yb mass bias factor was calculated using a natural <sup>173</sup>Yb/<sup>171</sup>Yb ratio of 1.123575 (Thirlwall & Anczkiewicz, 2004) and was used to correct for both Yb and Lu mass bias. A natural <sup>179</sup>Hf/<sup>177</sup>Hf ratio of 0.7325 (Patchett & Tatsumoto, 1980, 1981) was used to calculate the Hf mass bias factor.

To assess accuracy and precision, synthetic reference material zircons 'MUNZirc1' and 'MUNZirc3' ( $^{176}$ Hf/ $^{177}$ Hf =  $0.282135 \pm 7$ ; Fisher *et al.*, 2011a), as well as natural reference material zircons '91500' ( $^{176}$ Hf/ $^{177}$ Hf =  $0.282308 \pm 6$ ; Blichert-Toft, 2008), 'GJ-1' ( $^{176}$ Hf/ $^{177}$ Hf =  $0.282000 \pm 5$ ; Morel *et al.*, 2008), 'Plešovice' ( $^{176}$ Hf/ $^{177}$ Hf =  $0.282482 \pm 13$ ; Sláma *et al.*,

2008), and 'Mud Tank' ( $^{176}$ Hf/ $^{177}$ Hf =  $0.282507 \pm 6$ ; Woodhead & Hergt, 2005) were analyzed between every 5–10 sample analyses. The weighted mean corrected  $^{176}$ Hf/ $^{177}$ Hf values ( $\pm 2$ SD) obtained for the secondary reference materials were  $0.282142 \pm 38$  ( $n\!=\!8$ ) for MUNZirc1 and MUNZirc3,  $0.282305 \pm 42$  ( $n\!=\!5$ ) for 91500,  $0.282000 \pm 56$  ( $n\!=\!4$ ) for GJ-1,  $0.282517 \pm 24$  ( $n\!=\!5$ ) for Plešovice, and  $0.282527 \pm 42$  ( $n\!=\!5$ ) for Mud Tank.

The  $\epsilon Hf_i$  values were calculated relative to CHUR (present-day  $^{176}$ Hf/ $^{177}$ Hf = 0.282785;  $^{176}$ Lu/ $^{177}$ Hf = 0.0336; Bouvier et al., 2008) at the U-Pb age of each sample (concordia age if MSWD < 2 and mean <sup>207</sup>Pb/<sup>206</sup>Pb age if MSWD > 2) using  $\lambda^{-176}Lu = 1.867 \times 10^{-11} \text{ a}^{-1}$  (Scherer et al., 2001, 2003; Söderlund et al., 2004). Age corrections on the measured <sup>176</sup>Hf/<sup>177</sup>Hf were applied using the sample age interpreted from titanite and/or zircon dates; changing the correction age by ~20 Myr did not have a drastic effect on the epsilon values ( $\sim 0.5$  epsilon units). Uncertainties on the corrected 176Hf/177Hf ratios were propagated into the EHfi values; uncertainties on the <sup>176</sup>Lu/<sup>177</sup>Hf have negligible effect. Depleted-mantle model ages (T<sub>DM</sub>) were calculated relative to a depletedmodel mantle reservoir with present-day <sup>176</sup>Hf/<sup>177</sup>Hf = 0.28325 (Nowell et al., 1998; Griffin et al., 2000, 2002) and  $^{176}$ Lu/ $^{177}$ Hf = 0.0384 (Griffin *et al.*, 2000). Two-stage depleted-mantle model ages (T<sub>DM</sub><sup>C</sup>) were calculated using the same depleted mantle parameters and a crustal average <sup>176</sup>Lu/<sup>177</sup>Hf of 0.015 for the evolution of the crustal magma source after it separated from the depleted mantle (Griffin et al., 2002).

#### Whole-rock geochemistry

Samples representative of the range of rock types in the MPIS were selected for whole-rock geochemical analysis, with emphasis on those that contained accessory minerals that produced useful U-Pb age data. Between 0.5 and 0.75 kg of the least weathered or altered portions of each sample was first gently hammered into 1-2 cm fragments and powdered in a tungsten carbide (WC) ring mill and thoroughly mixed. More material was powdered for coarse-grained samples to ensure accurate representation of sample mineralogical composition. Sample powder (3.5  $\pm$  0.0001 g) was combined with  $7 \pm 0.0001$  g of di-lithium tetraborate flux for a lowdilution sample to flux ratio of 2:1, and thoroughly mixed by vortexer. The mixtures were then transferred to graphite crucibles and heated at 1000°C in a furnace for 30-40 min to ensure complete fusion. The resulting glass beads were then re-powdered in a WC ring mill to achieve optimal homogenization, and re-fused at 1000°C for an additional 30–40 min. The final glass bead was polished to an  $\sim$ 15  $\mu$ m finish, and 2–3 mm chips were then cut from the beads for trace element analysis. The chips were mounted in an epoxy puck and polished to a 1 µm finish. Whole-rock major elements were measured by XRF at Pomona College in Claremont, California using a PanAlytical Axios wavelengthdispersive system equipped with a standard set of crystals, a duplex detector, and calibrations constructed using 61 certified reference standards. Interference corrections are adapted from Johnson *et al.* (1999) and detection limits were described by Lackey *et al.* (2012).

Whole-rock trace elements were measured by LA-Q-ICP-MS at UCSB. The analytical setup was the same as that used for accessory phase trace elements, except that laser energy was set to 5 mJ and 30 s of washout was allowed between each analysis. Samples were ablated using line scans 50 µm wide and 250 µm long at a travel rate of  $2 \, \mu m \, s^{-1}$  for  $\sim 2 \, min$  of data each. Prior to each ablation period, surface contamination was removed from the sample surface by performing a line scan 50 µm wide by 250 µm long at a travel rate of  $70 \,\mu \text{m s}^{-1}$ . Three line scans were performed on each sample. Whole-rock reference materials BCR-2, BHVO-2, AGV-2, Atho-G, ML3B-G, StHs6/80-G, GOR132-G, and T1-G were measured at the beginning and end of the analytical session, with Atho-G and AGV-2 measured between every nine unknowns. Reference values used for these reference materials are from the GeoReM database, application version 18 (January 2015; http:// georem.mpch-mainz.gwdg.de/) (Jochum et al., 2005). Atho-G was used as the primary reference material and AGV-2 as the secondary reference material to assess accuracy of the measurements of each element individually. Three analyses were performed on each sample to assist in the recognition of outliers; the reported values are the arithmetic mean of the three values. LA-Q-ICP-MS data were reduced using the 'Trace Elements IS' data reduction scheme in lolite v2.5 (Paton et al., 2011). Ca content was measured by XRF, and was used as the internal elemental standard. Elements reported here were reproduced within less than 10% of the accepted values for AGV-2, except for Cs, Tb, Pb, and U (13.5%, 10.5%, 14.4%, and 10.9% difference from accepted values, respectively).

## **ACKNOWLEDGEMENTS**

We thank Andrew Kylander-Clark for assistance with LASS-ICP-MS data collection. Additionally, we thank Graham Lederer for reconnaissance work on the project, for providing samples, and for assistance in Nd isotope data collection. We are indebted to Callum Hetherington and an anonymous reviewer, whose insightful and constructive reviews led to substantial improvements to the paper.

## **FUNDING**

This work was supported by funding from the University of California, Santa Barbara.

#### **SUPPLEMENTARY DATA**

Supplementary data for this paper are available at *Journal of Petrology* online.

#### **REFERENCES**

- Anderson, J. L. & Bender, E. E. (1989). Nature and origin of Proterozoic A-type granitic magmatism in the southwestern United States of America. *Lithos* 23, 19–52.
- Barth, A. P., Wooden, J. L., Coleman, D. S. & Fanning, C. M. (2000). Geochronology of the Proterozoic basement of southwesternmost North America, and the origin and evolution of the Mojave crustal province. *Tectonics* 19, 616–629.
- Barth, A. P., Wooden, J. L., Coleman, D. S. & Vogel, M. B. (2009). Assembling and disassembling California: A zircon and monazite geochronologic framework for Proterozoic crustal evolution in southern California. *Journal of Geology* 117, 221–239.
- Barton, M. & Hamilton, D. L. (1978). Water-saturated melting relations to 5 kilobars of three Leucite Hills lavas. *Contributions to Mineralogy and Petrology* **66**, 41–49.
- Bea, F. (1996). Residence of REE, Y, Th and U in granites and crustal protoliths; Implications for the chemistry of crustal melts. *Journal of Petrology* **37**, 521–552.
- Beccaluva, L., Barbieri, M., Born, H., Brotzu, P., Coltorti, M., Conte, A., Garbarino, C. B., Gomes, G., Acciotta, M., Morbidelli, L., Ruberti, E., Siena, F. & Traversa, G. (1992). Fractional crystallization and liquid immiscibility processes in the alkaline–carbonatite complex of Juquiá (São Paulo, Brazil). *Journal of Petrology* 33, 1371–1404.
- Bell, K., Kjarsgaard, B. A. & Simonetti, A. (1999). Carbonatites into the twenty-first century. *Journal of Petrology* 39, 1839–1845.
- Belousova, E. A., Griffin, W. L., O'Reilly, S. Y. & Fisher, N. I. (2002). Igneous zircon: Trace element composition as an indicator of source rock type. Contributions to Mineralogy and Petrology 143, 602–622.
- Blichert-Toft, J. (2008). The Hf isotopic composition of zircon reference material 91500. *Chemical Geology* **253**, 252–257.
- Bouvier, A., Vervoort, J. D. & Patchett, P. J. (2008). The Lu-Hf and Sm-Nd isotopic composition of CHUR: Constraints from unequilibrated chondrites and implications for the bulk composition of terrestrial planets. *Earth and Planetary Science Letters* 273, 48–57.
- Burchfiel, B. C. & Davis, G. A. (1971). Clark Mountain thrust complex in the Cordillera of southeastern California: Geologic summary and field trip guide. In: Elders, W. A. (ed.) Geological Excursions in Southern California: Campus Museum Contributions Number 1. University of California, Riverside, pp. 1–28.
- Castor, S. B. (2008). The Mountain Pass rare-earth carbonatite and associated ultrapotassic rocks, California. *Canadian Mineralogist* 46, 779–806.
- Chu, N.-C., Taylor, R. N., Chavagnac, V., Nesbitt, R. W., Boella, R. M., Milton, J. A., German, C. R., Bayon, G. & Burton, K. (2002). Hf isotope ratio analysis using multi-collector inductively coupled plasma mass spectrometry: An evaluation of isobaric interference corrections. *Journal of Analytical Atomic Spectrometry* 17, 1567–1574.
- Cottle, J. M., Kylander-Clark, A. R. & Vrijmoed, J. C. (2012). U– Th/Pb geochronology of detrital zircon and monazite by single shot laser ablation inductively coupled plasma mass spectrometry (SS-LA-ICPMS). *Chemical Geology* 332–333, 136–147.
- Cottle, J. M., Burrows, A. J., Kylander-Clark, A., Freedman, P. A. & Cohen, R. S. (2013). Enhanced sensitivity in laser ablation multi-collector inductively coupled plasma mass spectrometry. *Journal of Analytical Atomic Spectrometry* 28, 1700–1706.
- Crow, H. C., III (1984). Geochemistry of shonkinites, syenites, and granites associated with the Sulphide Queen

- carbonatite body, Mountain Pass, California. MS thesis, University of Nevada, Las Vegas, 56 pp.
- Daniel, C. G. & Pyle, J. M. (2006). Monazite–xenotime thermochronometry and Al<sub>2</sub>SiO<sub>5</sub> reaction textures in the Picuris Range, northern New Mexico, USA: New evidence for a 1450–1400 Ma orogenic event. *Journal of Petrology* **47**, 97–118.
- Daniel, C. G., Pfeifer, L. S., Jones, J. V., III & McFarlane, C. M. (2013). Detrital zircon evidence for a non-Laurentian provenance, Mesoproterozoic (ca. 1490–1450 Ma) deposition and orogenesis in a reconstructed orogenic belt, northern New Mexico, USA: Defining the Picuris orogeny. Geological Society of America Bulletin 125, 1423–1441.
- DePaolo, D. J. (1981). Trace element and isotopic effects of combined wallrock assimilation and fractional crystallization. *Earth and Planetary Science Letters* **53**, 189–202.
- DeWitt, E., Kwak, L. M. & Zartman, R. E. (1987). U–Th–Pb and <sup>40</sup>Ar/<sup>39</sup>Ar dating of the Mountain Pass carbonatite and alkalic igneous rocks, southeastern California. *Geological Society of America, Abstracts with Programs* **19**, 642.
- DeWitt, E., Zartman, R. E. & Futa, K. (2000). Age and origin of the Mountain Pass carbonatite, southeastern California. *Geological Society of America, Abstracts with Programs* 32, 397.
- Downes, H., Balaganskaya, E., Beard, A., Liferovich, R. & Demaiffe, D. (2005). Petrogenetic processes in the ultramafic, alkaline and carbonatitic magmatism in the Kola Alkaline Province: A review. *Lithos* **85**, 48–75.
- Dubois, J. C., Retali, G. & Cesario, J. (1992). Isotopic analysis of rare earth elements by total vaporization of samples in thermal ionization mass spectrometry. *International Journal of Mass Spectrometry and Ion Processes* 120, 163–177.
- Eby, G. N. (1984). Geochronology of the Monteregian Hills alkaline igneous province, Quebec. *Geology* **12**, 468–470.
- Eby, G. N., Roden-Tice, M., Krueger, H. L., Ewing, W., Faxon, E. H. & Woolley, A. R. (1995). Geochronology and cooling history of the northern part of the Chilwa Alkaline Province, Malawi. *Journal of African Earth Sciences* 20, 275–288.
- Ernst, R. E. & Bell, K. (2010). Large igneous provinces (LIPs) and carbonatites. *Mineralogy and Petrology* **98**, 55–76.
- Evans, J. R. (1971). Geology and mineral deposits of the Mescal Range quadrangle, San Bernardino County, California. California Division of Mines and Geology Map Sheet 17, scale 1:62 500.
- Evans, J. R. (1974). Relationship of mineralization to major structural features in the Mountain Pass area, San Bernardino County, California. *California Geology* 27, 147–155.
- Ferry, J. M. & Watson, E. B. (2007). New thermodynamic models and revised calibrations for the Ti-in-zircon and Zr-in-rutile thermometers. Contributions to Mineralogy and Petrology 154, 429–437.
- Fisher, C. M., Hanchar, J. M., Samson, S. D., Dhuime, B., Blichert-Toft, J., Vervoort, J. D. & Lam, R. (2011a). Synthetic zircon doped with hafnium and rare earth elements: A reference material for in situ hafnium isotope analysis. Chemical Geology 286, 32–47.
- Fisher, C. M., McFarlane, C. R. M., Hanchar, J. M., Schmitz, M. D., Sylvester, P. J., Lam, R. & Longerich, H. P. (2011b). Sm-Nd isotope systematics by laser ablation-multicollector-inductively coupled plasma mass spectrometry: Methods and potential natural and synthetic reference materials. Chemical Geology 284, 1–20.
- Foley, S. F., Venturelli, G., Green, D. H. & Toscani, L. (1987). The ultrapotassic rocks: Characteristics, classification, and constraints for petrogenetic models. *Earth-Science Reviews* 24, 81–134.
- Fujimaki, H. (1986). Partition coefficients of Hf, Zr, and REE between zircon, apatite, and liquid. *Contributions to Mineralogy and Petrology* **94**, 42–45.

- Gibson, S. A., Thompson, R. N. & Day, J. A. (2006). Timescales and mechanisms of plume-lithosphere interactions: <sup>40</sup>Ar/<sup>39</sup>Ar geochronology and geochemistry of alkaline igneous rocks from the Paraná–Etendeka large igneous province. *Earth and Planetary Science Letters* **251**, 1–17.
- Gittins, J. & Harmer, R. E. (2003). Myth and reality in the carbonatite-silicate rock 'association'. Periodico di Mineralogia 72, 19–26.
- Gleason, J. D., Miller, C. F., Wooden, J. L. & Bennett, V. C. (1994). Petrogenesis of the highly potassic 1-42 Ga Barrel Spring pluton, southeastern California, with implications for mid-Proterozoic magma genesis in the southwestern USA. Contributions to Mineralogy and Petrology 118, 182–197.
- Green, D. H. & Wallace, M. E. (1988). Mantle metasomatism by ephemeral carbonatite melts. *Nature* **336**, 459–462.
- Griffin, W. L., Pearson, N. J., Belousova, E., Jackson, S. E., Van Achterbergh, E., O'Reilly, S. Y. & Shee, S. R. (2000). The Hf isotope composition of cratonic mantle: LAM-MC-ICPMS analysis of zircon megacrysts in kimberlites. *Geochimica et Cosmochimica Acta* 64, 133–147.
- Griffin, W. L., Wang, X., Jackson, S. E., Pearson, N. J., O'Reilly, S. Y., Xu, X. & Zhou, X. (2002). Zircon chemistry and magma mixing, SE China: *In-situ* analysis of Hf isotopes, Tonglu and Pingtan igneous complexes. *Lithos* 61, 237–269.
- Gromet, L. P. & Silver, L. T. (1983). Rare earth element distributions among minerals in a granodiorite and their petrogenetic implications. *Geochimica et Cosmochimica Acta* 47, 925–939.
- Hagen-Peter, G., Cottle, J. M., Tulloch, A. J. & Cox, S. C. (2015). Mixing between enriched lithospheric mantle and crustal components in a short-lived subduction-related magma system, Dry Valleys area, Antarctica: Insights from U-Pb geochronology, Hf isotopes, and whole-rock geochemistry. *Lithosphere* 7, 174–188.
- Hamilton, P. J., O'Nions, R. K., Bridgwater, D. & Nutman, A. (1983). Sm-Nd studies of Archaean metasediments and metavolcanics from West Greenland and their implications for the Earth's early history. Earth and Planetary Science Letters 62, 263–272.
- Harmer, R. E. (1999). The petrogenetic association of carbonatite and alkaline magmatism: Constraints from the Spitskop Complex, South Africa. *Journal of Petrology* 40, 525–548.
- Harmer, R. E. & Gittins, J. (1998). The case for primary, mantlederived carbonatite magma. *Journal of Petrology* 39, 1895–1903.
- Hauri, E. H., Shimizu, N., Dieu, J. J. & Hart, S. R. (1993). Evidence for hotspot-related carbonatite metasomatism in the oceanic upper mantle. *Nature* 365, 221–227.
- Haxel, G. B. (2005). Ultrapotassic mafic dikes and rare-earth element- and barium-rich carbonatite at Mountain Pass, Mojave Desert, Southern California: Summary and field trip localities. US Geological Survey, Open-File Report 2005– 1219, 53 pp.
- Haxel, G. B. (2007). Ultrapotassic rocks, carbonatite, and rare-earth element deposit, Mountain Pass, Southern California.
   In: Theodore, T. G. (ed.) Geology and Mineral Resources of the East Mojave National Scenic Area, San Bernardino County, California. US Geological Survey Bulletin 2160, 17–56.
- Hayden, L. A., Watson, E. B. & Wark, D. A. (2008). A thermobarometer for sphene (titanite). Contributions to Mineralogy and Petrology 155, 529–540.
- Hoffman, P. (1989). Speculations on Laurentia's first gigayear (2.0 to 1.0 Ga). *Geology* **17**, 135–138.
- Huang, Y.-M., Hawkesworth, C. J., van Calsteren, P. & McDermott, F. (1995). Geochemical characteristics and origin of the Jacupiranga carbonatites, Brazil. *Chemical Geology* 119, 79–99.

- Isnard, H., Brennetot, R., Caussignac, C., Caussignac, N. & Chartier, F. (2005). Investigations for determination of Gd and Sm isotopic compositions in spent nuclear fuels samples by MC ICPMS. *International Journal of Mass Spectrometry* 246, 66–73.
- Jacobsen, S. B. & Wasserburg, G. J. (1980). Sm-Nd isotopic evolution of chondrites. Earth and Planetary Science Letters 50, 139–155.
- Jaffe, H. W. (1955). Precambrian monazite and zircon from the Mountain Pass Rare-Earth district, San Bernardino County, California. Geological Society of America Bulletin 66, 1247–1256.
- Jochum, K. P., Nohl, U., Herwig, K., Lammel, E., Stoll, B. & Hofmann, A. W. (2005). GeoReM: a new geochemical database for reference materials and isotopic standards. *Geostandards and Geoanalytical Research* 29, 333–338.
- Jochum, K. P., Weis, U., Stoll, B., Kuzmin, D., Yang, Q., Raczek, I., Jacob, D. E., Stracke, A., Birbaum, K., Frick, D. A., Günther, D. & Enzweiler, J. (2011). Determination of reference values for NIST SRM 610–617 glasses following ISO guidelines. Geostandards and Geoanalytical Research 35, 397–429.
- Johnson, D. M., Hooper, P. R. & Conrey, R. M. (1999). XRF analysis of rocks and minerals for major and trace elements on a single low dilution Li-tetraborate fused bead. Advances in X-Ray Analysis 41, 843–867.
- Jones, A. P., Genge, M. & Carmody, L. (2013). Carbonate melts and carbonatites. In: Hazen, R. M., Jones, A. P. & Baross, J. A. (eds) Carbon in Earth. Mineralogical Society of America and Geochemical Society, Reviews in Mineralogy and Geochemistry 75, 289–322.
- Korobeinikov, A. N., Mitrofanov, F. P., Gehör, S., Laajoki, K., Pavlov, V. P. & Mamontov, V. P. (1998). Geology and copper sulphide mineralization of the Salmagorskii ring igneous complex, Kola Peninsula, NW Russia. *Journal of Petrology* 39, 2033–2041.
- Krenn, E., Harlov, D. E., Finger, F. & Wunder, B. (2012). LREE-redistribution among fluorapatite, monazite, and allanite at high pressures and temperatures. *American Mineralogist* 97, 1881–1890.
- Kylander-Clark, A. R. C., Hacker, B. R. & Cottle, J. M. (2013). Laser-ablation split-stream ICP petrochronology. *Chemical Geology* 345, 99–112.
- Lackey, J. S., Cecil, M., Windham, C. J., Frazer, R. E., Bindeman, I. N. & Gehrels, G. E. (2012). The Fine Gold Intrusive Suite: The roles of basement terranes and magma source development in the Early Cretaceous Sierra Nevada batholith. *Geosphere* 8, 292–313.
- Lanphere, M. A. (1964). Geochronologic studies in the Eastern Mojave Desert, California. *Journal of Geology* 72, 381–399.
- Lee, W.-J. & Wyllie, P. J. (1998). Processes of crustal carbonatite formation by liquid immiscibility and differentiation, elucidated by model systems. *Journal of Petrology* 39, 2005–2013.
- Liu, Y. S., Hu, Z. C., Zong, K. Q., Gao, C. G., Gao, S., Xu, J. & Chen, H. H. (2010). Reappraisement and refinement of zircon U-Pb isotope and trace element analyses by LA-ICP-MS. Chinese Science Bulletin 55, 1535–1546.
- Long, K. R., Van Gosen, B. S., Foley, N. K. & Cordier, D. (2010). The principal rare earth elements deposits of the United States—A summary of domestic deposits and a global perspective. US Geological Survey, Scientific Investigations Report 2010–5220, 96 pp.
- Ludwig, K. R. (2012). User's manual for Isoplot 3.75: A geochronological tool kit for Microsoft Excel. Berkeley Geochronological Centre Special Publication 5, 75 pp.

- Mahood, G. & Hildreth, W. (1983). Large partition coefficients for trace elements in high-silica rhyolites. *Geochimica et Cosmochimica Acta* 47, 11–30.
- Martin, L. H. J., Schmidt, M. W., Mattsson, H. B., Ulmer, P., Hametner, K. & Guenther, D. (2012). Element partitioning between immiscible carbonatite–kamafugite melts with application to the Italian ultrapotassic suite. *Chemical Geology* 320–321, 96–112.
- Martin, L. H. J., Schmidt, M. W., Mattsson, H. B. & Guenther, D. (2013). Element partitioning between immiscible carbonatite and silicate melts for dry and H<sub>2</sub>O-bearing systems at 1–3 GPa. *Journal of Petrology* **54**, 2301–2338.
- McDonough, W. F. & Sun, S.-S. (1995). The composition of the Earth. *Chemical Geology* **120**, 223–253.
- McKinney, S. T., Cottle, J. M. & Lederer, G. W. (2015). Evaluating rare earth element (REE) mineralization mechanisms in Proterozoic gneiss, Music Valley, California. *Geological Society of America Bulletin* **127**, 1135–1152.
- Morel, M. L. A, Nebel, O., Nebel-Jacobsen, Y. J., Miller, J. S. & Vroon, P. Z. (2008). Hafnium isotope characterization of the GJ-1 zircon reference material by solution and laser-ablation MC-ICPMS. Chemical Geology 255, 231–235.
- Nowell, G. M., Kempton, P. D., Noble, S. R., Saunders, A. D., Mahoney, J. J. & Taylor, R. N. (1998). High-precision Hf isotopic measurements of MORB and OIB by thermal ionization mass-spectrometry: Insights into the depleted mantle. Chemical Geology 149, 211–233.
- Nyman, M. W., Karlstrom, K. E., Kirby, E. & Graubard, C.M. (1994). Mesoproterozoic contractional orogeny in western North America: Evidence from *ca.* 1-4 Ga plutons. *Geology* 22, 901–904.
- Olson, J. E. & Pray, L. C. (1954). The Mountain Pass rare-earth deposits. In: Jahns, R. H. (ed.) Geology of Southern California. California Division of Mines Bulletin 170, Chapter 8, 23–39.
- Olson, J. C., Shawe, D. R., Pray, L. C. & Sharp, W. N. (1954). Rare-earth Mineral Deposits of the Mountain Pass District, San Bernardino County, California. US Geological Survey, Professional Papers 261, 91 pp.
- Panina, L. I. & Motorina, I. V. (2008). Liquid immiscibility in deep-seated magmas and the generation of carbonatite melts. *Geochemistry International* 45, 448–464.
- Pankhurst, M. J., Vernon, R. H., Turner, S. P., Schaefer, B. F. & Foden, J. D. (2011). Contrasting Sr and Nd isotopic behaviour during magma mingling; new insights from the Mannum A-type granite. *Lithos* 126, 135–146.
- Patchett, P. J. & Tatsumoto, M. (1980). Hafnium isotope variations in oceanic basalts. *Geophysical Research Letters* **7**, 1077–1080.
- Patchett, P. J. & Tatsumoto, M. (1981). A routine highprecision method for Lu–Hf isotope geochemistry and chronology. Contributions to Mineralogy and Petrology 75, 263–267.
- Paton, C., Hellstrom, J., Paul, B., Woodhead, J. & Hergt, J. (2011). Iolite: Freeware for the visualisation and processing of mass spectrometric data. *Journal of Analytical Atomic Spectrometry* 26, 2508–2518.
- Premo, W. R., DeWitt, E. H., Moscati, R. J., Cosca, M. A., Stoeser, D. & Premo, V. L. (2013). Ages and Pb–Sr–Nd isotopes of silicate rocks at Mountain Pass, Southern California. Geological Society of America, Abstracts with Programs 45, 113.
- Rudnick, R. L., McDonough, W. F. & Chappell, B. W. (1993). Carbonatite metasomatism in the northern Tanzanian mantle: petrographic and geochemical characteristics. *Earth and Planetary Science Letters* 117, 463–475.

- Santosh, M., Yang, Q.-Y., Ram Mohan, M., Tsunogae, T., Shaji, E. & Satyanarayanan, M. (2014). Cryogenian alkaline magmatism in the Southern Granulite Terrane, India: Petrology, geochemistry, zircon U-Pb ages and Lu-Hf isotopes. *Lithos* 208–209, 430–445.
- Sawka, W. N., Chappell, B. W. & Norrish, K. (1984). Light-rareearth-element zoning in sphene and allanite during granitoid fractionation. *Geology* 12, 131–134.
- Scherer, E., Münker, C. & Mezger, K. (2001). Calibration of the lutetium–hafnium clock. *Science* **293**, 683–687.
- Scherer, E. E., Mezger, K. & Münker, C. (2003). The <sup>176</sup>Lu decay constant discrepancy: Terrestrial samples vs. meteorites. *Meteoritics and Planetary Science* **38**, A136.
- Schmitt, A. K., Wetzel, F., Cooper, K. M., Zou, H. & Wörner, G. (2010). Magmatic longevity of Laacher See volcano (Eifel, Germany) indicated by U-Th dating of intrusive carbonatites. *Journal of Petrology* 51, 1053–1085.
- Shawe, D. R. (1952). Thorium resources of the Mountain Pass District, San Bernardino County, California. US Geological Survey Trace Element Investigation Report 251, 58 pp.
- Sláma, J., Košler, J., Condon, D. J., Crowley, J. L., Gerdes, A., Hanchar, J. M., Horstwood, M. S. A., Morris, G. A., Nasdala, L., Norberg, N., Schaltegger, U., Schoene, B., Tubrett, M. N. & Whitehouse, M. J. (2008). Plešovice zircon—A new natural reference material for U-Pb and Hf isotopic microanalysis. Chemical Geology 249, 1–35.
- Söderlund, U., Patchett, P. J., Vervoort, J. D. & Isachsen, C. E. (2004). The <sup>176</sup>Lu decay constant determined by Lu–Hf and U–Pb isotope systematics of Precambrian mafic intrusions. *Earth and Planetary Science Letters* **219**, 311–324.
- Spencer, K. J., Hacker, B. R., Kylander-Clark, A. R. C., Andersen,
  T. B., Cottle, J. M., Stearns, M. A., Poletti, J. E. & Seward, G.
  G. E. (2013). Campaign-style titanite U-Pb dating by laser-ablation ICP: Implications for crustal flow, phase transformations and titanite closure. *Chemical Geology* 341, 84–101.
- Stacey, J. S. & Kramers, J. D. (1975). Approximation of terrestrial lead isotope evolution by a 2-stage model. *Earth and Planetary Science Letters* **26**, 207–221.
- Stoeser, D. B. (2013). Mineralogy and late stage alteration of the Mountain Pass, California, ultrapotassic silicate intrusive rocks—Preliminary report. Geological Society of America, Abstracts with Programs 45, 500.
- Strickland, B. A., Wooden, J. L., Mattinson, C. G., Ushikubo, T., Miller, D. M. & Valley, J. W. (2013). Proterozoic evolution of the Mojave crustal province as preserved in the Ivanpah Mountains, southeastern California. *Precambrian Research* 224, 222–241.
- Tanaka, T., Togashi, S., Kamioka, H., Amakawa, H., Kagami, H., Hamamoto, T., Yuhara, M., Orihashi, Y., Yoneda, S., Shimizu, H., Kunimaru, T., Takahashi, K., Yanagi, T., Nakano, T., Fujimaki, H., Shinjo, R., Asahara, Y., Tanimizu, M. & Dragusanu, C. (2000). JNdi-1: A neodymium isotopic reference in consistency with LaJolla neodymium. *Chemical Geology* 168, 279–281.
- Thirlwall, M. F. & Anczkiewicz, R. (2004). Multidynamic isotope ratio analysis using MC-ICP-MS and the causes of secular drift in Hf, Nd and Pb isotope ratios. *International Journal of Mass Spectrometry* **235**, 59–81.
- Tilton, G. R., Bryce, J. G. & Mateen, A. (1998). Pb–Sr–Nd isotope data from 30 and 300 Ma collision zone carbonatites in northwest Pakistan. *Journal of Petrology* **39**, 1865–1874.
- Veizer, J., Bell, K. & Jansen, S. L. (1992). Temporal distribution of carbonatites. *Geology* 20, 1147–1149.
- Veksler, I. V., Petibon, C., Jenner, G. A., Dorfman, A. M. & Dingwell, D. B. (1998). Trace element partitioning in immiscible silicate-carbonate liquid systems: An initial

- experimental study using a centrifuge autoclave. *Journal of Petrology* **39**, 2095–2104.
- Veksler, I. V., Dorfman, A. M., Dulski, P., Kamenetsky, V. S., Danyushevsky, L. V., Jeffries, T. Dingwell, D. B. (2012). Partitioning of elements between silicate melt and immiscible fluoride, chloride, carbonate, phosphate and sulfate melts, with implications to the origin of natrocarbonatite. Geochimica et Cosmochimica Acta 79, 20–40.
- Verplanck, P. L. & Van Gosen, B. S. (2011). Carbonatite and alkaline intrusion-related rare earth element deposits—A deposit model. US Geological Survey, Open-File Report 2011-1256, 6 pp.
- Vervoort, J. D., Patchett, P. J., Blichert-Toft, J. & Albarède, F. (1999). Relationships between Lu-Hf and Sm-Nd isotopic systems in the global sedimentary system. *Earth and Planetary Science Letters* 168, 79–99.
- Vuorinen, J. H. & Hålenius, U. (2005). Nb-, Zr-, and LREE-rich titanite from the Alno alkaline complex: Crystal chemistry and its importance as a petrogenetic indicator. *Lithos* 83, 128–142.
- Wang, D., Yang, J., Yan, S., Xu, J., Chen, Y., Pu, G. & Luo, Y. (2001). A special orogenic-type rare earth element deposit in Maoniuping, Sichuan, China: Geology and geochemistry. Resource Geology 51, 177–188.
- Wasserburg, G. J., Jacobsen, S. B., DePaolo, D. J., McCulloch, M. T. & Wen, T. (1981). Precise determination of ratios, Sm and Nd isotopic abundances in standard solutions. *Geochimica et Cosmochimica Acta* 45, 2311–2323.
- Wendt, I. & Carl, C. (1991). The statistical distribution of the mean squared weighted deviation. *Chemical Geology* 86, 275–285
- Whitmeyer, S. J. & Karlstrom, K. E. (2007). Tectonic model for the Proterozoic growth of North America. *Geosphere* 3, 220–259.
- Williams, R. W., Gill, J. B. & Bruland, K. W. (1986). Ra–Th disequilibria systematics: Timescale of carbonatite magma formation at Oldoinyo Lengai volcano, Tanzania. *Geochimica et Cosmochimica Acta* 50, 1249–1259.

- Wooden, J. L. & Miller, D. M. (1990). Chronologic and isotopic framework for Early Proterozoic crustal evolution in the eastern Mojave Desert region, SE California. *Journal of Geophysical Research* 95, 20133–20146.
- Wooden, J. L., Barth, A. P. & Mueller, P. A. (2012). Crustal growth and tectonic evolution of the Mojave crustal province: Insights from hafnium isotope systematics in zircons. *Lithosphere* **5**, 17–28.
- Woodhead, J. D. & Hergt, J. M. (2005). A preliminary appraisal of seven natural zircon reference materials for *in situ* Hf isotope determination. *Geostandards and Geoanalytical Research* **29**, 183–195.
- Woolley, A. R. (2003). Igneous silicate rocks associated with carbonatites: Their diversity, relative abundances and implications for carbonatite genesis. *Periodico di Mineralogia* **72**, 9–17.
- Woyski, M. (1980). Petrology of the Mountain Pass Carbonatite Complex—a review. In: Fife, D. L. & Brown, A. R. (eds) Geology and Mineral Wealth of the California Desert. South Coast Geological Society, pp. 367–378.
- Yaxley, G. M., Crawford, A. J. & Green, D. H. (1991). Evidence for carbonatite metasomatism in spinel peridotite xenoliths from western Victoria, Australia. Earth and Planetary Science Letters 107, 305–317.
- Ying, J., Zhou, X. & Zhang, H. (2004). Geochemical and isotopic investigation of the Laiwu–Zibo carbonatites from western Shandong Province, China, and implications for their petrogenesis and enriched mantle source. *Lithos* 75, 413–426.
- Žácek, V., Škod, R. & Sulovský, P. (2009). U-Th-rich zircon, thorite and allanite-(Ce) as main carriers of radioactivity in the highly radioactive ultrapotassic melasyenite porphyry from the Šumava Mts., Moldanubian Zone, Czech Republic. *Journal of Geosciences* 54, 355–371.
- Zhou, L. & Wang, Y. (1989). REE geochemical characteristics of apatite, sphene and zircon from alkaline rocks. *Chinese Journal of Geochemistry* 8, 245–253.